

NATURAL ORIGIN SILICA REINFORCED DUAL FIBER MATRICES FOR
BONE TISSUE ENGINEERING

A THESIS SUBMITTED TO
THE GRADUATE SCHOOL OF NATURAL AND APPLIED SCIENCES
OF
MIDDLE EAST TECHNICAL UNIVERSITY

BY

ALİ DENİZ DALGIÇ

IN PARTIAL FULFILLMENT OF THE REQUIREMENTS
FOR
THE DEGREE OF DOCTOR OF PHILOSOPHY
IN
ENGINEERING SCIENCES

OCTOBER 2020

Approval of the thesis:

**NATURAL ORIGIN SILICA REINFORCED DUAL FIBER MATRICES
FOR BONE TISSUE ENGINEERING**

submitted by **ALİ DENİZ DALGIÇ** in partial fulfillment of the requirements for
the degree of **Doctor of Philosophy in Engineering Sciences, Middle East
Technical University** by,

Prof. Dr. Halil Kalıpçılar
Dean, Graduate School of **Natural and Applied Sciences** _____

Prof. Dr. Murat Dicleli
Head of the Department, **Engineering Sciences** _____

Prof. Dr. Dilek Keskin
Supervisor, **Engineering Sciences, METU** _____

Prof. Dr. Ayten Yazgan Karataş
Co-Supervisor, **Mol. Biol. and Gene., ITU** _____

Examining Committee Members:

Prof. Dr. Ayşen Tezcaner
Engineering Sciences, METU _____

Prof. Dr. Dilek Keskin
Engineering Sciences, METU _____

Assoc. Prof. Dr. Eda Ayşe Aksoy
Basic Pharmaceutical Sciences, Hacettepe Uni. _____

Prof. Dr. Şükrü Talaş
Metallurgical and Materials Eng., Afyon Kocatepe Uni. _____

Prof. Dr. Zafer Evis
Engineering Sciences, METU _____

Date: 02.10.2020

I hereby declare that all information in this document has been obtained and presented in accordance with academic rules and ethical conduct. I also declare that, as required by these rules and conduct, I have fully cited and referenced all material and results that are not original to this work.

Name, Last name : Dalgıç, Ali Deniz

Signature :

ABSTRACT

NATURAL ORIGIN SILICA REINFORCED DUAL FIBER MATRICES FOR BONE TISSUE ENGINEERING

Dalgıç, Ali Deniz
Doctor of Philosophy, Engineering Sciences
Supervisor: Prof. Dr. Dilek Keskin
Co-Supervisor: Prof. Dr. Ayten Yazgan Karataş

October 2020, 140 pages

Graft therapy is used to treat bone tissue loss, which has drawbacks; donor scarcity, risk of disease transmission and immune reaction. Tissue engineering scaffolds can overcome these drawbacks. In this study, a 3D scaffold that will support tissue regeneration at defect site was developed using mainly natural materials. Scaffold was produced by co-electrospinning and had two distinct fiber phases; first fiber phase was produced from a bacterial origin polymer, Poly(3-hydroxybutyrate-co-3-hydroxyvalerate) (PHBV), and small amount of Polycaprolactone (PCL) to support fiber structure, second fiber phase was formed by pullulan (PUL) polymer and diatom silica shells (DS) from single cell algae origin. Also, in the study, PHBV production by *Cupriavidus necator* bacterial strain was optimized and used to produce scaffold groups. PHBV/PCL/CA:PUL/DS scaffold group was produced as dual fiber matrix and a new crosslinking method for PUL was developed for crosslinking through electrospinning. Cefuroxime Axetil (CA) antibiotic was loaded into hydrophobic PHBV fibers to sustain antibiotic release from scaffold. Characterization studies revealed that, in aqueous environment scaffold degrade slowly, take less water and has stable structure, support controlled release of antibiotic and improved compressive strength due to incorporated DS and double

fiber structure. In vitro studies revealed that DS bearing groups improved Saos-2 cell viability and co-electrospun groups that have hydrophilic PUL fibers supported L929 cell viability. Scanning electron microscopy and confocal laser scanning microscopy analyses showed that cells distributed through co-electrospun scaffold with healthy morphology. In the study, a novel, 3D, dual fiber scaffold was produced with natural origin base materials and has potential to be used for bone tissue engineering applications.

Keywords: Bone Tissue Engineering, Diatom, Co-Electrospinning, Pullulan, Poly(3-hydroxybutyrate-co-3-hydroxyvalerate)

ÖZ

KEMİK DOKU MÜHENDİSLİĞİ İÇİN DOĞAL KÖKENLİ SİLİKA TAKVİYELİ ÇİFT FİBERLİ MATRİSLER

Dalgıç, Ali Deniz
Doktora, Mühendislik Bilimleri
Tez Yöneticisi: Prof. Dr. Dilek Keskin
Ortak Tez Yöneticisi: Prof. Dr. Ayten Yazgan Karataş

Ekim 2020, 140 sayfa

Kemik doku kayıplarının tedavisinde kullanılan greft terapilerde, donör kısıtlılığı, hastalık bulaşma riski ve immün reaksiyon dezavantajları bulunmaktadır. Doku mühendisliği taşıyıcıları bu dezavantajların önüne geçmektedir. Bu çalışmada, hasar bölgesindeki doku rejenerasyonunu destekleyecek, 3 boyutlu hücre taşıyıcı, temelde doğal malzemeler kullanılarak geliştirilmiştir. Hücre taşıyıcı, birlikte elektroğirme yöntemiyle üretilmiştir ve iki farklı fiber fazı bulunmaktadır; birinci fiber fazı bakteri kökenli polimer Poli(3-hidroksibütrat-ko-3-hidroksivalerat) (PHBV) ve yapıyı desteklemek için az miktarda Polikaprolakton (PCL) polimerlerinden üretilmiştir, ikinci fiber yapısı pullulan (PUL) polimeri ve tek-hücreli bir alg kökenli diatom silika kabuklarından (DS) oluşturulmuştur. Çalışmada ayrıca, *Cupriavidus necator* bakteri suşu'ndan PHBV üretimi optimize edilmiştir ve hücre taşıyıcı grupları üretiminde kullanılmıştır. PHBV/PCL/SA:PUL/DS hücre taşıyıcı grubu ikili fiber matrisi olarak üretilmiş ve PUL'ın elektroğirme sırasında çapraz bağlanması için yeni bir çaprazbağlama yöntemi geliştirilmiştir. Hücre taşıyıcıdan antibiyotik salımını sağlamak için hidrofobik PHBV fiberlerine Sefuroksim aksetil (SA) antibiyotiği yüklenmiştir. Karakterizasyon çalışmaları, hücre taşıyıcının su içeren

ortamda yavaş hızda bozunduğunu, az su emdiği ve sabit yapısının olduğunu, kontrollü antibiyotik salımını desteklediğini ve içerdiği DS ve çift fiber yapısı sayesinde gelişmiş basma dayanımına sahip olduğunu ortaya çıkarmıştır. In vitro çalışmalar, DS içeren grupların Saos-2 hücre canlılığını arttırdığını ve hidrofilik PUL fiberleri içeren birlikte elektroğirilmiş grupların L929 hücre canlılığını desteklediğini ortaya çıkarmıştır. Taramalı elektron mikroskobu ve konfokal lazer taramalı mikroskobu analizleri, hücrelerin birlikte elektroğirilmiş taşıyıcı içerisinde sağlıklı morfolojiyle yayıldığını göstermiştir. Çalışmada, yeni, 3 boyutlu, ikili fiberli hücre taşıyıcı, temelinde doğal kökenli malzemeler ile üretilmiştir ve kemik doku mühendisliği uygulamalarında kullanılma potansiyeli bulunmaktadır.

Anahtar Kelimeler: Kemik Doku Mühendisliği, Diatom, Birlikte Elektroğirme, Pullulan, Poli(3-hidroksibütirat-co-3-hidroksivalerat)

This thesis is dedicated to my family and my beloved one.

ACKNOWLEDGMENTS

The study of PhD is a long way with many unique challenges to overcome and I want to express my deepest gratitude to my advisor Prof. Dr. Dilek Keskin who always supported and believed in me with her endless understanding, who guided me to overcome challenges and turn them into successes. I want to thank Prof. Dr. Ayşen Tezcaner for her support and guidance through my PhD study. One of the many things that she taught me was to be result oriented that pushed me forward. I also want to thank Prof. Dr. Zafer Evis for supporting me to improve myself on new academic studies and guiding me to create new academic collaborations. His support and academic life advices was very valuable for me. I want to thank Prof. Dr. Ayten Yazgan Karataş for her academic support. I want to thank to my lab mate, my best friend Deniz Atila who was there, surviving long study nights with me at MM building, for endless support, chats on the meaning of life and reminding the joy of living. I want to thank Gizem Demir for always being there for me. I want to thank to my family, who always supported me through my PhD study.

The production studies of PHBV from bacterial strains were conducted by study group of Prof. Dr. Ayten Yazgan Karataş at Istanbul Technical University.

This thesis was financially supported with TUBITAK 1001 (215M893) and METU BAP DKT-310-2018-3638 projects.

TABLE OF CONTENTS

ABSTRACT.....	v
ÖZ.....	vii
ACKNOWLEDGMENTS	x
TABLE OF CONTENTS.....	xi
LIST OF TABLES	xvi
LIST OF FIGURES	xvii
LIST OF ABBREVIATIONS.....	xxiii
CHAPTERS	
1 INTRODUCTION	1
1.1 Functions of Bone	1
1.2 Structure of Bone	1
1.3 Bone Development by Growth, Modelling and Remodeling.....	3
1.4 Bone Tissue Engineering	5
1.5 Silicone in Bone Tissue Engineering	10
1.6 Diatom Silica Shells as Silicone Source	11
1.6.1 Diatom Silica Shells in Biotechnology	12
1.6.2 The Use of Diatom Silica Shell in Bone Tissue Engineering.....	13
1.7 Electrospinning.....	15
1.8 Natural Origin Polymers for Tissue Engineering Applications	17
1.8.1 Polyhydroxyalkanoates	18
1.8.2 Poly(ϵ -caprolactone).....	20
1.8.3 Pullulan	21

1.9	Local Treatments of Bone via Drug Delivery from Bone Implants/Scaffolds	22
1.10	Aim of the study	24
2	MATERIALS AND METHODS	27
2.1	Materials	27
2.2	Production, Purification and Characterization of Synthesized PHBV	28
2.2.1	PHBV Production by <i>Cupriavidus necator</i>	28
2.2.2	Optimization of PHBV Production by <i>Cupriavidus necator</i>	28
2.2.3	Isolation and Purification of Synthesized PHBV	29
2.2.4	Characterization of Produced Synthesized PHBV	30
2.3	Purification and characterization of DS.....	32
2.3.1	Purification and Pulverization of DS.....	32
2.3.2	Morphology and Size Analysis of DS.....	33
2.3.3	Chemical Characterization of DS.....	33
2.4	In Vitro Cytotoxicity Analysis of DS	33
2.4.1	MTT Cell Viability Assay	34
2.4.2	Indirect Cell Viability Assay of DS.....	34
2.4.3	Direct Cell Viability Assay of DS.....	35
2.5	Production of 3-D Fibrous Bone Tissue Engineering Scaffold Groups ...	36
2.5.1	Electrospinning of Control Group Scaffolds	36
2.5.2	Co-electrospinning of PHBV/PCL/CA:PUL/DS Scaffold	36
2.5.3	Production of B-PHBV/PCL/CA:PUL/DS Scaffold Using B-PHBV	38
2.6	Characterization of Scaffolds.....	38
2.6.1	Scanning Electron Microscopy Analysis.....	38

2.6.2	Pore Size Distribution and Porosity Analysis	38
2.6.3	Weight Loss, Enzymatic Degradation and Water Retention Analysis 39	
2.6.4	Water Contact Angle Analysis.....	40
2.6.5	Calcium Adsorption on Scaffolds	40
2.6.6	Cefuroxime Axetil Loading and Release Studies	41
2.6.7	Tensile and Compressive Strength Tests	42
2.6.8	SEM Observation of Fiber Break Points Under Tensile stress	42
2.7	In Vitro Cell Culture Studies.....	42
2.7.1	Alamar Blue Cell Viability Assay	43
2.7.2	Determination of Alkaline Phosphatase Activity and Intracellular Calcium Amount.....	44
2.7.3	Analysis of Cell Attachment and Morphology on Scaffolds	45
2.7.4	Confocal Laser Scanning Microscopy Analysis	45
2.7.5	Statistical Analysis.....	46
3	RESULTS AND DISCUSSION	47
3.1	Results of Production, Purification and Characterization of PHBV produced by Bacteria	47
3.1.1	Valerate Mole Percentage of Synthesized PHBV	52
3.1.2	Molecular Weight of PHBV Determined by Static Light Scattering Spectrometry	52
3.1.3	Results of Fourier Transform Infrared Spectroscopy Analysis of PHBV	56
3.1.4	Results of Differential Scanning Calorimetry Analysis of PHBV....	57
3.2	Results of Purification and Chemical Analysis of Diatom Silica Shells..	58

3.3	Results of Purification and Chemical Analysis of Diatom Silica Shells ..	61
3.4	Evaluation of Effects of DS on Cell Viability	63
3.4.1	Results of Cell Viability After Direct Contact with DS	63
3.4.2	Results of Cell Viability After Direct Contact with DS	65
3.4.3	Results of Cell Viability on Scaffolds with Different Polymer/DS Concentrations	68
3.5	Production and Morphological Characterization of Scaffold Groups	68
3.5.1	Optimization of Production of the PHBV/PCL Fiber Phase	69
3.5.2	Optimization of Production of the PUL/DS Fiber Phase	75
3.5.3	Properties of Co-electrospun Scaffold.....	82
3.6	Comparison of Pore Size Distribution and Porosity of Scaffold Groups .	84
3.7	Weight Loss, Water Retention and Enzymatic degradation Results of Scaffold Groups.....	85
3.8	Calcium Deposition on Scaffold Groups	89
3.9	Fiber Morphology of Scaffold Groups	91
3.10	Efficiency of Cefuroxime Axetil Loading and Release Profiles of the Scaffolds	93
3.11	Mechanical Test Results of the Scaffolds.....	95
3.11.1	Results of Tension Test	96
3.11.2	Results of Compression Test.....	98
3.12	Results of In Vitro Cell Culture Experiments.....	100
3.12.1	Saos-2 and L929 Cell Viability on Scaffold Groups.....	100
3.12.2	Cell Morphology and Attachment Analysis by Scanning Electron Microscopy	103

3.12.3	Alkaline Phosphatase Activity and Calcium Deposition on Scaffold Groups	105
3.12.4	Cell Morphology and Distribution Analysis by Laser Scanning Confocal Microscopy	107
4	CONCLUSION	109
	REFERENCES	111
	APPENDICES	
A.	Appendix A	137
	CURRICULUM VITAE	139

LIST OF TABLES

TABLES

Table 1.1 Components and methods used in some recent bone tissue engineering studies.	9
Table 3.1 Elemental compositions of DS determined by X-ray photoelectron spectroscopy	60
Table 3.2 Optimization trials for crosslinking PUL. RT: Drying at RT, L: Lyophilization, 60 °C: High temperature was applied to polymer solution with GTA for 1 h, GTA: GTA crosslinking. PBS: Degradation experiment. Table was first divided into two parts according to in situ cross-linking method; GTA (groups 1-9) or STMP (groups 10-15) and additional operations are marked in the order. The success of crosslinking was presented as stability in PBS.	78
Table 3.3 Tensile strength test results of scaffold groups. α : Statistical significant difference of PHBV/PCL/CA:PUL/DS and B-PHBV/PCL/CA:PUL/DS groups Young modulus results from other groups. β : Statistical significant difference of PHBV/PCL group ultimate tensile strength from PHBV/PCL/DS and B-PHBV/PCL/CA:PUL/DS groups.....	97
Table 3.4 Compressive strength test results of scaffold groups. α : Statistical significant difference of B-PHBV/PCL/CA:PUL/DS groups' Young modulus result from PHBV/PCL and PHBV/PCL/DS groups. β : Statistical significant difference of B-PHBV/PCL/CA:PUL/DS groups' compressive strength result from PHBV/PCL and PHBV/PCL/DS groups results.....	99

LIST OF FIGURES

FIGURES

Figure 1.1. Nano to micro size structural organization of bone tissue (Y. Liu et al., 2016).	2
Figure 1.2 Schematic illustration of remodeling cycle of bone (Truesdell & Saunders, 2019).	5
Figure 1.3 Morphology of silica frustules of different diatom species (Frazer, 2016).	11
Figure 1.4 Schematic illustration of wet electrospinning.	16
Figure 1.5 Chemical formula of PHB, PHV and PHBV polymers (Ross et al., 2017).	19
Figure 1.6 Chemical synthesis routes of PCL (Guarino et al., 2002).	20
Figure 1.7 Chemical formula of Pullulan (Ferreira et al., 2015).	21
Figure 1.8 Schematic illustration of electrospinning systems of scaffold groups; PHBV/PCL (a), PUL/DS (b), PHBV/PCL/DS (c), PHBV/PCL/CA:PUL/DS (d). Schematic illustration of co-electrospun PHBV/PCL/CA:PUL/DS scaffold (e). SEM image of co-electrospun PHBV/PCL/CA:PUL/DS scaffold (f).	25
Figure 2.1. Schematic illustration of separation and purification steps of PHBV polymer which produced by bacteria.	30
Figure 2.2. Schematic illustration of wet electrospinning system for production of electrospun PHBV/PCL (Left) and DS bearing PHBV/PCL/DS fibrous scaffolds.	36
Figure 2.3. Schematic illustration of wet co-electrospinning system for production of PHBV/PCL/CA:PUL/DS scaffold.	37
Figure 3.1. The production of polymer granules in <i>Bacillus polymyxa</i> bacteria cells was observed after Sudan Black B staining.	47
Figure 3.2. H-NMR peaks of purified polymer produced by <i>Bacillus polymyxa</i> . ..	48
Figure 3.3. H-NMR peaks of purified polymer produced by <i>Cupriavidus necator</i> , first (a) and second (b) trials.	49
Figure 3.4. The production of polymer granules in <i>Cupriavidus necator</i> bacteria cells was observed after Sudan Black B staining. (400 X magnifications).	50

Figure 3.5. The H-NMR peaks of PHBV produced by <i>Cupriavidus necator</i> strain (a). The H-NMR peaks of commercially obtained PHBV (b).	51
Figure 3.6. Zimm plot of static light scattering spectrometry data of commercially obtained PHBV (a) and produced PHBV (b) at different concentrations and angles.	54
Figure 3.7. Fourier transform infrared spectroscopy curve of PHBV produced by <i>Cupriavidus necator</i> bacterial strain.	56
Figure 3.8. Differential Scanning Calorimetry heat curves of commercially obtained PHBV (a) and PHBV produced by <i>Cupriavidus necator</i> bacterial strain.	58
Figure 3.9. Light microscopy images of DS before (a) and after (b) purification. SEM images of micro-nano structure of DS (c). Elemental composition results obtained by EDX analysis of DS (d).	60
Figure 3.10. Scanning electron microscopy images of DS particles after basic lysis at 10 000X (a) and 100 000X magnifications. Scale bars show 10 μm (a) and 1 μm (b).	61
Figure 3.11. Scanning electron microscopy of DS particles as a whole (a) and after grinding for 1 min (b). Images were taken at 10 000X magnification and scale bars show 10 μm length. Light microscopy images of DS after 1 (c), 5 (d), 10 (e) and 15 (f) min of grinding. Images were taken at 10X magnification and scale bars show 30 μm length. Particle size distribution graphs of DS particles after 1 min (g) and 15 min (h) of grinding.	63
Figure 3.12. MTT assay results of direct cell interaction of different concentrations of ground and not ground DS groups after 1 day (a) and 2 days (b) of incubation. The percent cell viabilities were calculated with respect to control group involving cells without DS direct contact. α , β , γ : The statistically significant differences between ground and not ground groups ($p < 0.01$).	65
Figure 3.13. MTT assay results of indirect cell interaction of different concentrations of ground and not ground DS groups after 1 (a), 3 (b) and 7 (c) days of incubation. The percent cell viabilities were calculated with respect to control group; cells without DS interaction. α : The statistically significant differences between not	

ground and ground DS groups ($p < 0.05$). β : The statistically significant differences between not ground and ground DS groups ($p < 0.01$).....	67
Figure 3.14. Alamar Blue assay results of cell viability study of scaffolds with different polymer/DS ratios. α : The statistically significant difference between 20/1 ratio group and all other groups at day 1. β : The statistically significant difference of 20/1 ratio group from other groups after 2 days of incubation ($p < 0.05$).	68
Figure 3.15. SEM images of PHBV fibers produced by dry (a) and wet (b) electrospinning methods using chloroform as the solvent. SEM images of PHBV fibers produced by dry electrospinning using chloroform/acetic acid (1/1) (c) and chloroform/HFIP (1/1) (d) as the polymer solvents. Images were taken at 500X magnification and scale bars show 200 μm length.	71
Figure 3.16. SEM images of PHBV fibers produced by wet electrospinning using HFIP as the polymer solvent. Red circles indicate fractures on fiber structure. Image was taken at 5000X magnification and scale bars show 20 μm length.	72
Figure 3.17. SEM images of fiber morphology of electrospun PHBV/PVA and PHBV/PCL scaffolds prepared by different blend ratios; The PHBV:PVA ratio is 9:1 (a), 8:2 (b) and 7:3 (c). The PHBV:PCL ratio is 9:1 (d), 8:2 (e) and 7:3 (f). Red circles indicate breakages on fiber structures. Image was taken at 5000X magnification and scale bars show 20 μm length.	74
Figure 3.18. SEM images of electrospun PUL/DS scaffolds prepared by PUL/DS blend at 20/1 (a), 10/1 (b), 5/1 (c) and 4/1 (d) wt/wt ratios. Images were taken at 1000X magnification while scale bars show 100 μm length.	76
Figure 3.19. SEM images of intact groups (2-9 and 14) with PUL cross-linking, after PBS incubation. The image to the right of each numbered image is the version of the same experimental group produced using DMF as solvent. (All scale bars: 100 μm).	80
Figure 3.20. Cyclic hemiacetal formation by GTA in acidic pH (a) α,β -unsaturated glutaraldehyde polymer formation by GTA in basic pH (b). Crosslinking of PUL by acetal bridge formation with GTA hemiacetal ring (c). Shema was modified from studies of Hermanson and Li et al., (Hermanson, 2013; Y. Li et al., 2018).	81

Figure 3.21. SEM images of co-electropun PHBV/PCL/CA:PUL/DS scaffold at different magnification. Images were taken at 500X (Left) and 2500X (Right) magnifications while scale bars show 200 (Left) and 40 μm (Right) lengths..... 83

Figure 3.22. Pore size distributions of the scaffold groups; PHBV/PCL (a), PHBV/PCL/DS (b), PHBV/PCL/CA:PUL/DS (c) and B-PHBV/PCL/CA:PUL/DS (d). Red arrow indicates the decrease in amount of smaller pore size in B-PHBV/PCL/CA:PUL/DS scaffold compared to other groups..... 85

Figure 3.23. Cumulative weight loss (a) and water retention (b) results of scaffold groups incubated for 21 days..... 87

Figure 3.24. Cumulative weight loss of scaffold groups under lysozyme (1 mg/mL) degradation through 14 days of incubation (a). SEM images of B-PHBV/PCL/CA:PUL/DS scaffold after 1 (b) and 2 (c) weeks of degradation. Arrows show DS morphology in between fibers. Scale bars show 20 μm length. 89

Figure 3.25. The amount of calcium deposited onto scaffold groups after 7 and 14 days of incubation in SBF. α : Indicates the statistically significant difference of PHBV/PCL group from other groups after 7 and 14 days of incubation. β : Indicates the statistically significant difference of the co-electrospun group from PHBV/PCL/DS and PHBV/PCL/CA groups after 7 days of incubation. ($p < 0.05$). 91

Figure 3.26. SEM images of PHBV/PCL (a) B-PHBV/PCL (b) PHBV/PCL/CA:PUL/DS (c) and B-PHBV/PCL/CA:PUL/DS (d) scaffold groups. Images were taken at 1000X (a and b) and 2000X (c and d) magnifications while scale bars show 100 μm (a and b), 40 μm (c) and 50 μm (d) lengths. 93

Figure 3.27. Percent cumulative CA release from scaffold groups through 21 days of incubation period. Release was studied in PBS at 37 $^{\circ}\text{C}$ ($n = 4$). 95

Figure 3.28. Representative stress strain curve for PHBV/PCL scaffold under tensile load. 97

Figure 3.29. SEM images of fibers breaking point when tensile force is applied. Arrow shows DS in between fibers. Scale bars show 20 μm length. 98

Figure 3.30. Representative stress strain curve for PHBV/PCL scaffold under compressive load. 100

Figure 3.31. The Alamar Blue reduction of Saos-2 (a) and L929 (b) cells grown on scaffold groups through 1, 4 and 7 days of incubation periods. α : Statistically significant difference of PHBV/PCL/CA:PUL/DS and B-PHBV/PCL/CA:PUL/DS from PHBV/PCL and PHBV/PCL/CA groups after 4 day of incubation ($p < 0.05$). β : Statistically significant difference of PHBV/PCL/CA:PUL/DS and B-PHBV/PCL/CA:PUL/DS from PHBV/PCL/CA group after 7 day of incubation ($p < 0.05$). Θ : Statistically significant difference of PHBV/PCL/CA:PUL/DS and B-PHBV/PCL/CA:PUL/DS groups from other groups after 7 and 14 days of incubation ($p < 0.05$)..... 102

Figure 3.32. SEM images of Saos-2 cells after 7 days of incubation on scaffold groups (a) PHBV/PCL, (b) PHBV/PCL/DS, (c) PHBV/PCL/CA and (d) PHBV/PCL/CA:PUL/DS. Images were taken at 2500X magnifications while scale bars show 40 μm length. Red circles show cells on fibers. 103

Figure 3.33. SEM images of Saos-2 cells proliferating for 7 days on B-PHBV/PCL (a and b) and B-PHBV/PCL/CA:PUL/DS (c and d) scaffold groups. (Arrows: Cells on fibers). The scale bars on the images show 20 μm length. 104

Figure 3.34. Saos-2 cell ALP activity after 7 and 14 days of incubation on PHBV/PCL scaffolds containing different concentrations of DS. Saos-2 cells grown as PHBV/PCL scaffold without DS was the control group (a). ALP activities of Saos-2 cells grown on scaffold groups after 7 and 14 days of incubation (b). As a result of the ALP activity assay, intracellular calcium levels of Saos-2 cells proliferated on scaffold groups (c). 106

Figure 3.35. Laser-scanning confocal microscopy images of Saos-2 cells grown for 7 days on PHBV/PCL (a), PHBV/PCL/DS (b), PHBV/PCL/CA (c), PHBV/PCL/CA:PUL/DS (d), B-PHBV/PCL (e) and B-PHBV/PCL/CA:PUL/DS (f) scaffold groups. The cell cytoplasm was labeled with FTIC (Green) and nuclei was labeled with Draq5 (Red) fluorescent dyes (CSLM, Leica DM2500, Germany). Average cell spreading areas of Saos-2 cells that were proliferated on scaffold groups after 7 days of incubation (g). Scale bars (a-f) show 50 μm length. *: Statistically

significant difference of PHBV/PCL/CA:PUL/DS and B-PHBV/PCL/CA:PUL/DS groups from PHBV/PCL group..... 108

LIST OF ABBREVIATIONS

ABBREVIATIONS

ALP: Alkaline phosphatase

BCA: Bicinchoninic Acid

BSA: Bovine Serum Albumin

HFIP: Hexafluoro-2-propanol

FBS: Fetal Bovine Serum

FTIR: Fourier Transform Infrared Spectrophotometer

GTA: Glutaraldehyde

DMEM: Dulbecco's Modified Eagle Medium

DMSO: Dimethyl Sulfoxide

DS: Diatom Silica Shells

DSC: Differential Scanning Calorimetry

H-NMR: Hydrogen Nuclear Magnetic Resonance

PBS: Phosphate Buffer Saline

PCL: Polycaprolactone

PHBV: Poly(3-hydroxybutyrate-co-3-hydroxyvalerate)

pNPP: P-Nitrophenyl Phosphate

PUL: Pullulan

PVA: Polyvinyl Alcohol

SEM: Scanning Electron Microscopy

CHAPTER 1

INTRODUCTION

1.1 Functions of Bone

Bone has many different roles in our body other than being the base of mechanical support. Physical functions of bone tissue include protection of vital organs from external forces, locomotion and support of the body. Bone tissue stores calcium and phosphate minerals and plays important role on regulation of mineral balance. Large bones in the body contains bone marrow which produces blood cells. There are two types of bone marrow; red marrow (Myeloid tissue) produces red blood cells, platelets and most of the white blood cells and yellow marrow (Fatty tissue) that produces some of the white blood cells. Red marrow is located inside spongy bone and contains hematopoietic stem cells that can differentiate into blood cells. Hematopoietic stem cells can differentiate into cells from myeloid and lymphoid lineages by hematopoiesis to produce monocytes, macrophages, neutrophils, basophils, eosinophils, erythrocytes, dendritic cells, and megakaryocytes or platelets, as well as T cells, B cells, and natural killer cells. Yellow marrow is present in central cavities of long bones and yellow marrow contains mesenchymal stem cells that can differentiate into stromal lineages of chondrocytes, osteoblasts, osteoclasts, adipocytes, myocytes, macrophages, endothelial cells and fibroblasts (David B. Burr, 2019).

1.2 Structure of Bone

Bone structure is hierarchical and formed by highly organized micro-nano structures. At the micron level, bone has haversian system that carry, blood vessels, nerves and

lymphatic canals. Osteons contain lamellae layers that surround one another in circular formation. Bone tissue is formed by organization of organic and inorganic phases (Figure 1.1).

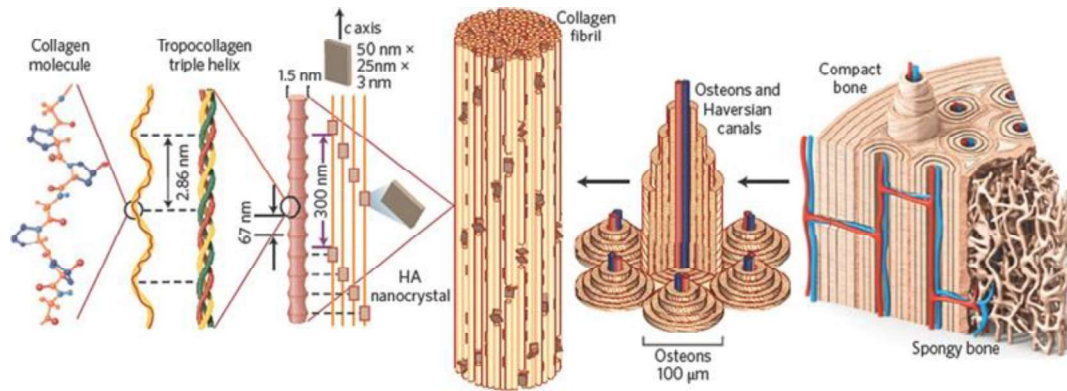


Figure 1.1. Nano to micro size structural organization of bone tissue (Y. Liu et al., 2016).

The organic part of the bone forms 25 wt% of the bone tissue. The main organic component of the bone is type I collagen and forms 90 wt% of the bone's organic phase. Type III and type V collagen also can be found at trace amounts. Remaining approximately 10 wt% organic components of the bone are metabolic proteins that are mandatory for collagen metabolism, regulation of bone modeling and cellular metabolism. The inorganic phase of the bone is mainly carbonated hydroxyapatite that forms 65 wt% of bone. Carbonate is deposited in the form of calcium carbonate alongside with amorphous calcium phosphate. Carbonate ratio of the bone varies with age and is roughly between 4-8 wt% (Landi et al., 2003). Bone mineral, carbonated hydroxyapatite, has low crystallinity. Carbonated apatite minerals fill the gaps at the ends of collagen fibrils and also forms alongside collagen fibrils parallel to their longitudinal axis. This orientation of apatite minerals and collagen fibrils forms the unique mechanical properties of bone. The mineral phase gives stiffness to bone structure while collagen fibrils distribute stress along the structure and support ductility of tissue. Remaining 10% weight of the bone is occupied by water (David B. Burr, 2019; Y. Liu et al., 2016). The bones of adult skeletal system are

formed by 80% of cortical bone and 20% of trabecular bone. Cortical bone tissue is denser than trabecular bone tissue and surrounds the marrow space in bones. While trabecular bone has a network of trabecular plates that forms a porous sponge like structure which contains bone marrow. Cortical bones have less than 5% porosity which increases with the remodeling through aging. A fibrous connective tissue, periosteum sheath, surrounds the surface of cortical bone which contains blood vessels and nerve fibers. Collagenous fibers bind periosteum to the outer surface of bone. Periosteum has higher bone formation than resorption which increases bone thickness in time. The inner surfaces of cortical and trabecular bones are covered by endosteum membrane which contains blood vessels and bone cells (Clarke, 2008).

1.3 Bone Development by Growth, Modelling and Remodeling

Longitudinal and radial growth of bone occurs in childhood and adolescence periods in human life. Longitudinal growth of the bone occurs through growth plates at the epiphyseal and metaphyseal areas of long bones. During growth, initially cartilage proliferates in the growth plates and primary new bone is formed by mineralization of the newly formed tissue. Bone can change structure by modelling in response to physiologic influences or mechanical forces. In adulthood bone remodeling is more frequent than bone modelling (Kobayashi et al., 2003). In order for bone to maintain its strength and mineral homeostasis, bone remodeling occurs. Bone remodeling is also needed for fracture healing (Florencio-Silva et al., 2015). Through bone remodeling, old bone is removed and replaced by synthesized proteinaceous bone matrix which is later mineralized to form bone tissue. Remodeling of bone removes micro damages and preserves bone strength. Osteoclasts and osteoblasts work as a group and remodeling is sustained by resorption of old bone by osteoclasts and formation of new bone by osteoblasts. Remodeling of bone mainly occurs randomly, and targeted remodeling occurs at damaged sites. Biomechanical forces can trigger independent actions of osteoblasts and osteoclasts which initiate widening of bone or surface modification by removing and addition of bone. The independent actions

of osteoblasts and osteoclasts show that there is no tightly coupled bone formation and resorption cycle in bone modelling contrary to bone remodeling (Clarke, 2008).

Remodeling cycle can be divided into four phases; activation, resorption, reversal, and formation (Figure 1.2) (D. B. Burr, 2002; Florencio-Silva et al., 2015; Parfitt, 2002). Activation phase starts by arrival and activation of mononuclear monocyte-macrophage osteoclast precursors cells (Roodman, 1999). Initially, bone surface layer, endosteum, lift up and multinucleated preosteoclasts form by fusion of multiple mononuclear cells. The pH of the area decreases around 4.5 as osteoclasts secrete hydrogen ions. Low pH helps to mobilize the bone mineral (Silver et al., 1988). Osteoclasts start to secrete tartrate-resistant acid phosphatase, cathepsin K, matrix metalloproteinase 9, and gelatinase enzymes in order to degrade bone matrix (Delaissé et al., 2003). Preosteoclasts bind to bone matrix and seal the resorption area. Resorption by osteoclasts completes in 2 to 4 weeks. Multinucleated osteoclasts undergo apoptosis as the resorption phase is completed (Clarke, 2008; ERIKSEN, 1986; Reddy, 2004). Reversal phase follows the completion of resorption. In reversal phase, preosteoblasts become present at resorption cavity and necessary signaling takes place to start bone formation phase. Some of signals known to link bone resorption phase to formation phase are growth factors like TGF- β , IGF-1, IGF-2, PDGF and cytokines like bone morphogenetic proteins. The osteocalcin and alkaline phosphatase levels known to be related with TGF- β concentration. As the bone formation stage starts, osteoblast deposit collagenous bone matrix and matrix is mineralized by release of calcium, phosphate bearing vesicles. As the new bone tissue forms, osteoblasts become trapped in bone matrix and turn into osteocytes. At the end of bone formation step, over 50% of the remaining osteoblasts undergo apoptosis leaving the cell population in the matrix to osteocytes and bone lining cells. Bone lining cells can later differentiate into osteoblasts through chemical or mechanical signaling (Clarke, 2008).

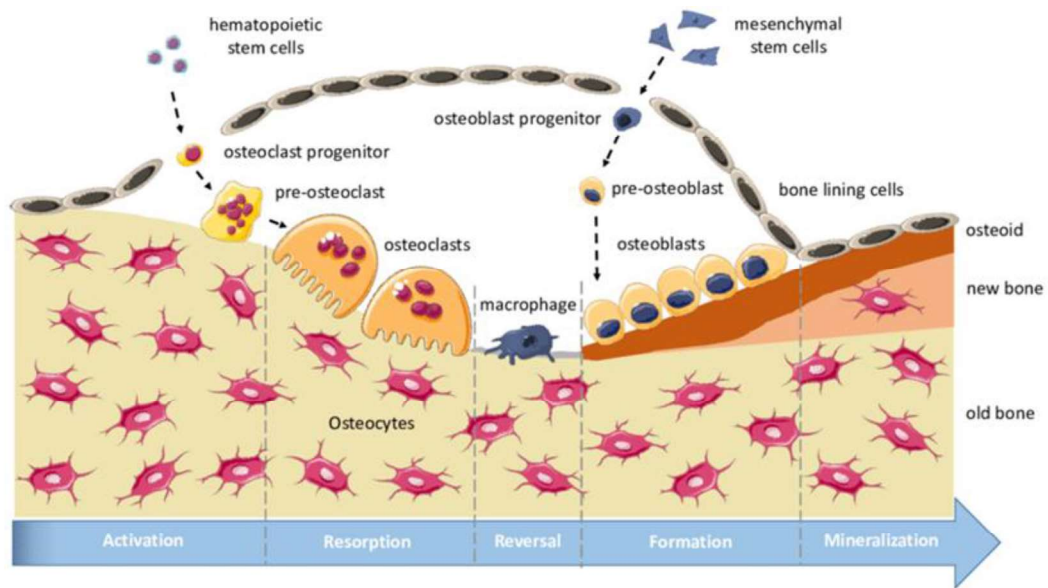


Figure 1.2 Schematic illustration of remodeling cycle of bone (Truesdell & Saunders, 2019).

1.4 Bone Tissue Engineering

Bone tissue loss can occur after an incident like accident, tumor removal, bone infections or osteoporosis. If the defect is larger than a certain size, which can differ for different bone type and defect location, the bone tissue fails to regenerate and heal the defect. This type of defects are called as critical size defects and cannot heal unless there is a planned reconstruction and a second surgery (Schemitsch, 2017). The average size of the defect to form a critical size defect is reported to be 3 cm in radius and ulna, 5 cm in femur and tibia and 6 cm in the humerus (Stewart et al., 2015). In order to fill the place of lost bone and ensure tissue healing, one of the treatment approaches is to take bone tissue from another healthy site of patient or donor to replace the lost tissue. Bone tissue transplantation can be performed in two ways as allograft and autograft. Treatment with allograft means transplantation of bone tissue from another individual. When transplanted, the damaged area is mechanically supported with new bone tissue and bone repair is initiated. With this method, the patient undergoes only one operation and enters the healing process. However, allograft therapy may have negative results as; giving a genetically

different tissue to the patient may cause an immune system. In addition, transplantation of tissue from another individual may cause the transport of diseases. Low number of donors is another problem in the treatment of allograft. Autograft treatment may be preferred to prevent these problems. In autograft treatment, tissue is taken from another bone of patient to be transferred to the damaged area; thus, the risk of rejecting the tissue disappears. However, this process will create a second bone tissue damage in the patient and may cause extra complications as well as need of a second operation (Samorezov & Alsberga, 2015).

Tissue engineering combines interdisciplinary approaches to create treatment options that will perform the function of lost tissue or regenerate the damaged tissues and organs (Meijer et al., 2007). In bone tissue engineering, tissue-like cell carriers are used for therapeutic purposes and it is desirable to develop biomaterials that are close to the properties of bone tissue and/or support bone regeneration. Although there are many new developments, there is still a need for new three-dimensional cell carriers that are biocompatible, contain bioactive components, can be degraded in accordance with tissue regeneration while providing the necessary support after implantation (Lim et al., 2010; Uppal & Ramaswamy, 2011).

A scaffold for bone tissue engineering need to meet some fundamental requirements of biological and structural properties. Biocompatibility of a scaffold is a must; scaffold material itself and scaffold's degradation products must be nontoxic. The bioresorbable and biodegradable materials of the scaffold will release products and body should be able to excrete these materials without any serious side effects and toxicity on other organs (Henkel et al., 2013). The scaffold should be able to integrate with the host tissue without creating an active chronic inflammatory response that will prevent healing (Amini et al., 2012). Alongside with biocompatibility, bioactivity of the scaffold is important for scaffold host interaction and promotion of regeneration. The biological and chemical cues would improve scaffold bioactivity and increase osseointegration by improving cell response via scaffold-host

communication. Osteoinduction would be sustained as inducing osteogenic differentiation of migrated cells on scaffold (J. R. Porter et al., 2009; Roseti et al., 2017). The release of osteoinductive factors from biomaterials to improve cell response or release of calcium phosphate ions from calcium-phosphate biomaterials to trigger osteogenic differentiation are examples (Motamedian, 2015).

The structural properties of biomaterial are another important parameter that will affect biomaterial fate in body. First of all, biomaterial should provide adequate mechanical support to tissue and gradually transfer mechanical support to regenerating bone tissue as the scaffold degrades. The biodegradation rate of the scaffold should be compatible with regeneration rate of the tissue; scaffold should sustain its stability and mechanical support mainly on the early healing stages and the time of healing can vary with age of a person. For young, fracture can heal around 6 weeks up to a point where tissue can bear weight stress (O'Brien, 2011). In terms of micron sized properties, the porosity of the scaffold should be at a level which creates interconnectivity along scaffold. Interconnectivity of pores enable migration of cells and tissue ingrowth while sustaining necessary nutrient flow through scaffold. Porous scaffold is also needed for creating voids for vascularization (Karageorgiou & Kaplan, 2005). For bone tissue engineering scaffolds, 200-500 μm pore size was reported to be optimal for cell colonization and vascularization (Thavornnyutikarn et al., 2014). In terms of nanostructure, when the materials became nano sized, materials show different properties than their micro sized or bulk properties which would be advantageous. For example, nano sized structures possess high torsion and tensile modulus. The ceramics lose their brittleness when the size decreased to nano (Gong et al., 2015). The scaffolds can be doped with nanomaterial at desired concentrations to promote bioactivity and create micro-nano structures for adequate cell response.

In order to increase scaffold-cell and scaffold-host interaction and communication, several bioactive molecules can be combined in scaffold structure. Bioactive

molecules can be incorporated to scaffold surface by physical/chemical links or by doping into scaffold components. Growth factors can be used to initiate osteogenic differentiation, anti-inflammatory drugs can be used to limit inflammatory host reaction or ECM mimicking materials can be incorporated to improve cell response (Matassi et al., 2011; J. R. Porter et al., 2009). The search for optimum scaffold characteristics and modifications continue for bone tissue engineering as new materials and developments arise. The materials used for bone tissue engineering can be classified in three groups; polymers, bioactive ceramics and composites of these materials. Polymers can be classified as natural and synthetic. Natural polymers have advantages like better biocompatibility, cytocompatibility and low immunogenicity but have disadvantages like fast degradation and low mechanical stability. On the other hand, synthetic polymers have controllable slow degradation which doesn't cause fast decrease in mechanical strength. The mechanical properties of synthetic polymers and degradation rates can be tailored to match with desired application. Their production can be done in large batches with less batch to batch variation and cost-effectively. However, synthetic polymers have lower interaction with cells compared to natural polymers that have higher bioactivity potential (Matassi et al., 2011). Bioactive ceramics can also be obtained from natural or synthetic sources. Examples of bioactive ceramics are calcium-phosphate based hydroxyapatite and tricalcium phosphate (TCP), coralline (CaCO_3), calcium silicate and bioactive glass. Scaffolds prepared from ceramics show high compressive strength which improves its stability under load but ceramic scaffolds also show high brittleness (Gao et al., 2014). In order to overcome limitations of polymers and ceramics, composites of polymer/polymer or polymer/ceramic are used to form scaffolds. Some of the scaffold compositions in recent studies are summarized in Table 1.1. Bone itself has two main phases; organic collagen fibers that mineralized with inorganic hydroxyapatite. Composites of polymer/polymer or polymer/ceramic, with natural/synthetic polymers and bioceramics, are used to tailor properties like, controllable biodegradation, hydrophilicity, mechanical strength, surface morphology and bioactivity (Roseti et al., 2017).

Table 1.1 Components and methods used in some recent bone tissue engineering studies.

<i>Material Class</i>	<i>Materials</i>	<i>Production Method</i>	<i>Reference</i>
Polymer (Synthetic)	poly(ϵ -caprolactone)	3D Printing	(Zamani et al., 2020)
Polymer (Synthetic)/Inorganic Composite	Poly-L-lactic acid/MgO nanoparticles	Selective laser sintering	(Shuai et al., 2020)
Polymer (Synthetic, Natural)/Inorganic Composite	Poly(d,L-lactide)/Gelatin/Glass-ceramics	Electro_ spinning	(Bochicchio et al., 2020)
Inorganic/Polymer (Natural) Composite	Nano-HA/type I collagen	3D printing	(Montalbano et al., 2020)
Metal-organic framework/Polymer (Synthetic) Composite	Zeolitic imidazolate frameworks/Poly-L-lactic acid	Selective laser sintering	(Yang et al., 2020)
Polymer (Natural)	Chitosan	Freeze drying	(De Witte et al., 2020)
Polymer (Natural)/Inorganic Composite	Collagen/Nanohydroxyapatite	Hydrogel formation	(Xihe Zhang et al., 2020)
Polymer (Synthetic)/Polymer (Natural) Composite	Polycaprolactone/gelatin	Co-electro_ spinning	(Yi Wang et al., 2019)
Inorganic Calcium Phosphate Composite	Hydroxyapatite/Tri calcium phosphate	3D Printing	(Xiangjia Li et al., 2019)

1.5 Silicone in Bone Tissue Engineering

Silicone (Si) is one of the elements that plays crucial roles on the bone health. Studies have showed the benefits of dietary Si on bone tissue health and its possible effects on collagen synthesis and stabilization, and matrix mineralization (Jugdaohsingh, 2007). The effect of Si is concentrated on mineralization of growing bone. The human exposure of Si is depended mainly on dietary uptake. Si can be taken from food and drinking water and contribute to our metabolism. Higher dietary intake of Si has associated with improved bone mineral density by human studies (Jugdaohsingh et al., 2004). In the literature, Si deprivation studies were conducted on animals and concluded that Si deprivation causes abnormal and immature skeletal growth. Si deprivation in chicks was reported to cause undeveloped legs and beaks that are easily fractured (Carlisle, 1972). In the studies with rats, similar results were observed with defective skull formation (Schwarz & Milne, 1972), and decrease in bone mineral density was reported by additional studies. The obvious effect of Si deprivation on decreased bone mineral deposition and increased collagen breakdown was proven (Nielsen & Poellot, 2004; Seaborn & Nielsen, 2002). The positive effect of Si on osteogenesis of bone related cells was approved in terms of proliferation, alkaline phosphatase activity, matrix deposition levels and osteocalcin synthesis. These findings have motivated the use of silicon in bone implants and cements. Silicon substituted hydroxyapatite and bioglass showed that silicon substitution improves binding of the implant to the bone. Silicon substitution have been shown to induce a biologically active layer deposition on to the surface of the implant (Hench et al., 2004). The Si in the implants partially dissolves and released Si creates an amorphous Si layer on the surface. The released Si ions that are interacting with cells, reported to incline gene upregulation that will trigger osteogenesis by osteoblast proliferation and then differentiation. The Si substituted hydroxyapatite was reported to increase the order of collagen fibrils and create more complete bone structure (A. E. Porter et al., 2004). The toxicity of silica/silicate species have reported to be parallel to long term exposure and/or high doses. In the toxic levels, silica can cause

kidney inflammation and renal stone formation that will damage the kidney. In order to create toxic effect, the exposed level of silicon should be high and perpetual. By normal dietary uptake of silicon and by a silicon containing implant it is unlikely to reach a toxic level (Jugdaohsingh, 2007).

1.6 Diatom Silica Shells as Silicone Source

Diatom algae are single-celled eukaryotic organisms that can survive in all aquatic environments; they play a role in most of the biosilica production in the oceans. The cell walls of the diatoms are composed of amorphous silica involving shells, which are supposed to be created for protection purposes, show high mechanical strength owing to its unique geometry. There are 100 000 different types of diatoms known in nature, each with different forms. Diatom algae produce silica nanoparticles with silicic acid in the cell cytoplasm and take them out of the cell for inclusion in the extracellular shell structure (Nassif & Livage, 2011). Diatom shell is a smooth geometric structure made of amorphous silica, which can be of different sizes with symmetrical and regular nano-sized pores (Figure 1.3).

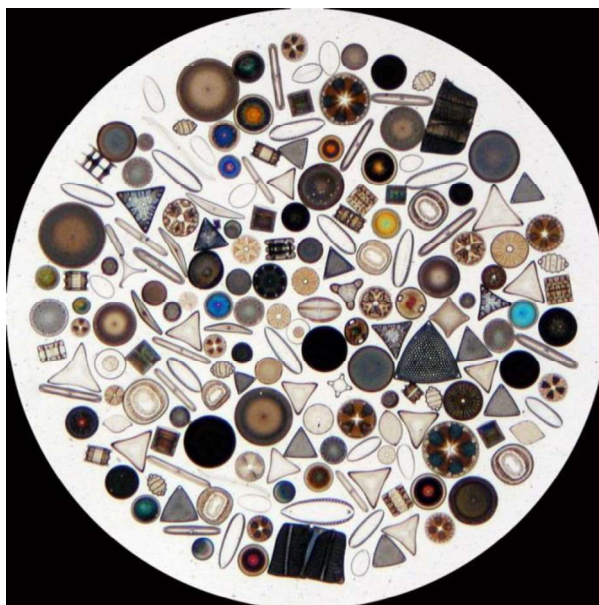


Figure 1.3 Morphology of silica frustules of different diatom species (Frazer, 2016).

This biosilica structures that diatoms synthesize naturally and under normal conditions, possess high mechanical strength and unique geometry; thus are promising for many applications (Aw et al., 2011). Diatoms are now used in oil exploration, toxicity testing, and for the source of biological silica. Diatoms are also used in many industrial areas due to their unique silica geometry as; Water and food filter, building material and chromatography material (Jamali et al., 2012). Diatoms can be easily cultured in a simple aquarium environment. Diatoms can multiply in a very short time and produced diatoms can be collected from by filtering. Nevertheless, the diatomaceous earth is the cheapest and effortless way to obtain silica structures of diatoms.

1.6.1 Diatom Silica Shells in Biotechnology

In the field of biotechnology, diatoms are used as drug delivery systems and in bio-identification and molecular selective separation processes (Dolatabadi & de la Guardia, 2011). The wide surface area, optically active geometry, nano-sized pores, high melting point and the mechanical strength of the DS, support their use in many areas of biomaterials field. The Si-OH groups on the surface of the silica structure are active points for chemical reactions and create a surface that can easily undergo chemical changes. Antibody-modified diatom biosilica structures have been reported as biosensors in the literature (Bismuto et al., 2008; De Stefano et al., 2009; Dolatabadi & de la Guardia, 2011). In recent years, the production of mesoporous silica-based nanoparticles and formation of drug release systems in nano or micro-sizes are highly studied (Bharti et al., 2015; Brunella et al., 2016; Butler et al., 2016). Although mesoporous silica particles have biocompatibility, biodegradability and positive effect on drug solubility by high drug loading capacity with chemical surface modifications, mesoporous silica particles have been highlighted with their long duration of production, high cost and requirement of use of toxic materials in

production cycles limit their use. For these reasons, biosilica structures where diatoms are synthesized naturally, come to the fore (Aw et al., 2011).

In literature, these silica shells were proposed as carriers for controlled drug delivery. Aw et al. (2011) investigated the encapsulation efficacy of indomethacin, an anti-inflammatory drug, and its release behaviour from diatom silica shells. In their studies, they have successfully increased the availability of hydrophobic indomethacin in a hydrophilic environment by diatom shell encapsulation (Aw et al., 2011). In another study, the surface of the diatom silica shells was modified in two different ways to obtain hydrophilic and hydrophobic surfaces. Then, loading and release of drugs of different properties were investigated. While the rate of confinement and controlled release of hydrophilic drugs was more successful with hydrophobic diatom surface, the confinement rates and controlled release of hydrophobic drugs were more successful when the surface of the diatoms was hydrophilic (Bariana et al., 2013). The smallest size of the silica shell structures is about 10 microns in average, so, their controlled drug delivery systems are generally studied for oral administration or local implantation routes. In the study of Zhang et al. (2013), the encapsulation and release of mesalamin and prednisone, drugs for treatment of gastrointestinal diseases, from diatom shells were examined separately. It has been reported that the Caco-2/HT-29 co-culture monolayer permeability of the drugs trapped in the diatom shell increased as DS have decreased TEER charge of the monolayer and improved permeation. In addition, the study reported that silica based diatom shells did not cause toxicity in Caco-2, HT-29, HCT-116 cell lines (H. Zhang et al., 2013).

1.6.2 The Use of Diatom Silica Shell in Bone Tissue Engineering

The use of silica based local drug delivery systems in the concept of bone tissue engineering includes controlled and long-term releases of antibiotics, growth factors, anti-inflammatory and anticancer drugs (Simovic et al., 2011). Alongside to be used

as drug delivery systems, silica-based materials has been widely investigated as biomaterials for bone tissue engineering. In the study of Lopez-Alvarez et al. (2009), the interaction between bone cells and silica was investigated via silica and hydroxyapatite (HA) based coating. It was reported that the Silica/HA coated surface increased the adhesion and proliferation of Saos-2 cells compared to HA coated one. It is stated that this effect is due to the silicon in the silica structure. In the study, silicon-containing, synthetic silica and diatom earth (kizelgur) were used as two different sources of silicon. Diatom/HA surface coating has been reported to increase cell attachment and proliferation relative to the synthetic silica/HA surface coating. The results of this study also demonstrate the potential for the use of diatom in composite polymeric carriers in bone tissue engineering applications. A small amount of silicone released from the diatom or silica structure is thought to cause the improvement in cell viability. Also the presence of other basic elements in the structure of silica diatom shells was likely to trigger osteoblastic cell behavior (López-Álvarez et al., 2009).

In recent years, the idea of the use of diatom silica shells in bone tissue engineering studies has started to find more space in the literature. Le et al. (2018) investigated the compatibility of DS with cells (Le et al., 2018b). To date, only a few studies have investigated the use of DS in scaffold for bone tissue. These diatom shell fragments or diatomaceous earth scaffolds or biomaterial were; silk fibroin carrier (Le et al., 2018b), chitosan membrane (Tamburaci & Tihminlioglu, 2017, 2018) and bone cement (Xiang Zhang et al., 2018). In these studies, the main role of DS added to the carrier structure was being the natural source of silicon. The contribution of silicon to bone formation is explained by increasing the proliferation of bone cells, alkaline phosphatase activity, bone matrix formation and osteocalcin production (Jugdaohsingh, 2007).

1.7 Electrospinning

Electrospinning is a widely used and versatile method to produce tissue engineering fibrous scaffolds. The main working principle of electrospinning is the formation of polymer jet flow towards the collector that is connected to the ground, via the charge transfer with the applied voltage. Mass flow of the polymer from the syringe tip depends on increasing or decreasing the current (Blackwood et al., 2008; Canton et al., 2010). Two important features of the electrospun scaffolds that improve their suitability for tissue engineering applications are the similarity of the fibers obtained by electrospinning to the randomly positioned collagen fibers found in the majority of extracellular matrixes in the body and the high porosity provided by the electrodeposition of fibers, a suitable structure for both cell transplantation and migration, as well as for the transfer of nutrients and cell wastes (Meng et al., 2007). Electrospinning enables control on fiber diameter and orientation. Formation of fibrous scaffolds provide high surface area which can improve cell attachment, spreading and proliferation. Scaffold properties can be tuned by changing several parameters of the electrospinning system such as polymer molecular weight, polymer concentration, solvent type, flow rate, applied voltage and collector distance. Polymer concentration and solvent type have high impact on the success of electrospinning by affecting viscosity and surface tension. Decrease in the viscosity and surface tension will result in thinner polymer fibers. If the viscosity is too low, fiber will not form and polymer solution will come out as droplets and if the viscosity is too high, polymer solution can block the syringe tip with decreased ejection rate. Concentration of the solution needs to be enough to sustain chain entanglement to form fiber structure (Husain et al., 2016; Xue et al., 2019). Volatility of the solvent should be high enough to prevent wet fiber deposition onto collector and low enough to prevent possible solidification of the jet on the solvent drop. The evaporation rate of the solvent can also be affected by ambient conditions like temperature and humidity. Solutions have different dielectric constants and dielectric constant determines the electrostatic repulsion among the surface charges residing on the jet

(Luo et al., 2012). For chain entanglement, polymer molecular weight should also be high enough to create fibers. Lower polymer molecular weight could result in bead formation since chain entanglement will be low (Xue et al., 2019).

Conventional electrospinning uses single hollow needle and produces 2D, sheet like, polymer fibrous mat that is collected on a solid conductive collector. In order to increase thickness and obtain a 3D fibrous mat wet electrospinning can be used (Figure 1.4). In wet electrospinning, electrospun fibers are collected into a collector bath which contain solution that does not dissolve polymer fibers. Wet electrospun fibers will have increased distance in between fibers thus forming 3D scaffolds.

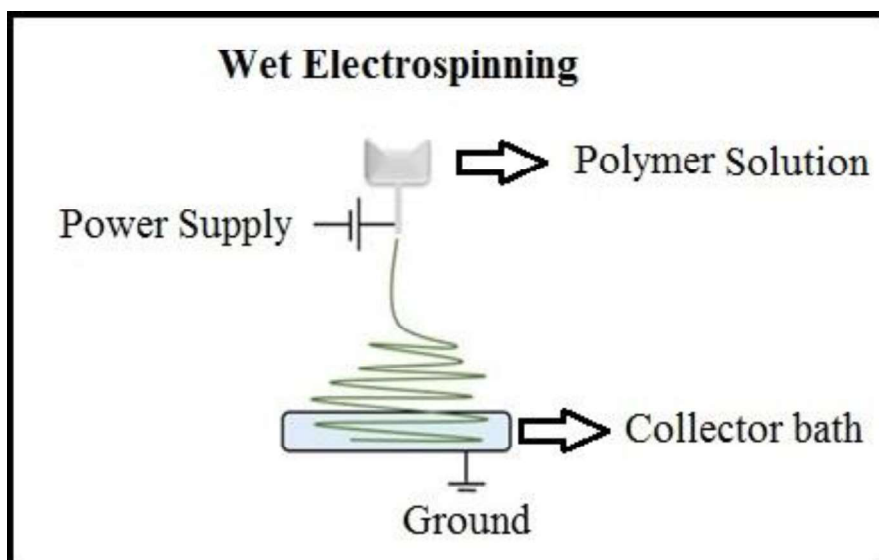


Figure 1.4 Schematic illustration of wet electrospinning.

Co-electrospinning system can be built up with two distinct syringe pumps and two separate voltage supply while using a mutual collector for both. This method enables production of a fibrous mat from randomly oriented fibers of two different polymers. Distinct polymer fibers are produced from different syringe systems that type of the polymer solvent, flow rate, voltage amount and distance from the collector can be optimized separately thus enabling production of electrospun scaffold from two

different polymer fibers with distinct morphology. By this means separate advantages and preferred properties of polymer fibers can be brought together in a single scaffold (Dalgic et al., 2019). Hydrophilic and hydrophobic random fibers can be created to tailor hydrophobicity and create different surface characteristics with distinct polymers. By tailoring these properties protein adhesion mechanisms can be altered which will have direct control on the cell-scaffold interaction and cell fate (Bacakova et al., 2011). In literature, different methods were used to tailor hydrophobicity of electrospun polymer fibers; bringing together different polymers in a fibrous scaffold by electrospinning of polymer blend solution or coating of polymer fibers that was reported to sustain low stability (C. H. Kim et al., 2006).

1.8 Natural Origin Polymers for Tissue Engineering Applications

Natural origin materials have several advantages over synthetic materials like tolerable biodegradation rates and better biocompatibility. These properties make them suitable components for tissue engineering applications (Rehm, 2010). The production of wide range of natural polymers can be achieved using microorganisms. The cultivation of microorganisms for polymer production is accepted as an environmentally friendly method (Bhattacharya & Gupta, 2005). However, some of the natural production methods can become costly since the purification steps of the polymer increases the cost compared to synthetic production of a polymer. On the other hand, some polymers can be obtained at fairly low costs by natural production methods with optimized industrial production systems (Basnett & Roy, 2010; Sionkowska, 2011). One of the biggest advantages of using natural origin polymer in tissue engineering over chemically synthesizing the polymer is the ability of sustainable production of natural origin polymers from renewable resources. The optimized industrial production methods, inherent biocompatibility and biodegradability makes natural origin polymers preferred constituents of tissue engineering scaffolds (Rehm, 2010).

1.8.1 Polyhydroxyalkanoates

Poly-hydroxyalkanoates (PHA) are biodegradable and biocompatible thermoplastic polyesters produced by intracellular energy and carbon deposition by soil bacteria, blue green algae and some genetically modified microorganisms (Sombatmankhong et al., 2007; Suwantong et al., 2007). Bacteria store PHAs as granules with a size between 0.2 to 0.5 μm in cytoplasm. PHA producing bacteria can be divided into two groups as bacteria need to be under specific nutrient limitation to produce PHA and bacteria which do not require nutrient limitation (Muhammadi et al., 2015). Bacteria like *Ralstonia eutropha*, *Pseudomonas oleovorans* and *Pseudomonas putida* do not produce PHA in growth phase and need to be under nutrient limitation to trigger PHA production. On the other hand, bacteria like recombinant *Escherichia coli* can produce PHA in growth phase, so, does not need nutrient limitation to trigger PHA production (Nitschke et al., 2011; Raza et al., 2018). PHAs are seen as potential materials to be used in the health industry since they can be obtained from natural origin. Poly-3-hydroxybutyrate (PHB) and hydroxyvalalate (HV) are used in various ratios to produce the co-polymer PHBV (Figure 1.5). In addition, as a result of the co-polymerization of PHB with HV, the crystallinity glass transition and melting temperatures can be reduced, and flexibility can be increased, and thus, it can be made into a material that can be processed more easily (Lü et al., 2012; Suwantong et al., 2007). Among PHAs, PHB and PHBV can spontaneously be degraded in blood and tissues to form a natural molecule d, l- β -hydroxybutyrate that is readily available in the body and create less inflammatory response since degradation products are readily available in body (Naznin Sultana & Khan, 2012; Suwantong et al., 2007). PHBV hydrolyses by acid-base catalysis for esters and normally hydrolysis rate can be low at natural pH and body temperature. However, in body, PHBV degradation can happen at a faster rate compared to in vitro with the effect of nonspecific esterases and lysozyme enzymes secreted by immune cells (H. Li & Chang, 2005; Naznin Sultana & Khan, 2012). In the literature, biocompatibility of PHBV based scaffolds produced by film-cast and solute-leaching methods have been reported in

many in vitro studies with various cell types; osteoblasts, epithelial cells and chondrocytes (Lü et al., 2012; Sombatmankhong et al., 2007; Suwantong et al., 2007). Healthy osteoblast proliferation was reported in PHBV foams for bone tissue engineering (Köse et al., 2003). In literature, PHBV composite cell carriers are mixed with other materials, such as hydroxyapatite, gelatin and collagen, in order to improve their physical and chemical properties. In addition, cell adhesion and proliferation properties of PHBV scaffolds were attempted to be improved by modifying surface properties of PHBV (Lü et al., 2012). In the literature, fibrous scaffolds produced from PHBV and similar polymers and their various composites are mostly in two dimensions like membrane structures (Bai et al., 2015; Kouhi et al., 2018; Sajesh et al., 2016; Zou et al., 2016). Production of a PHBV based 3D fibrous scaffolds with adjustable thickness would improve the application areas for bone tissue engineering.

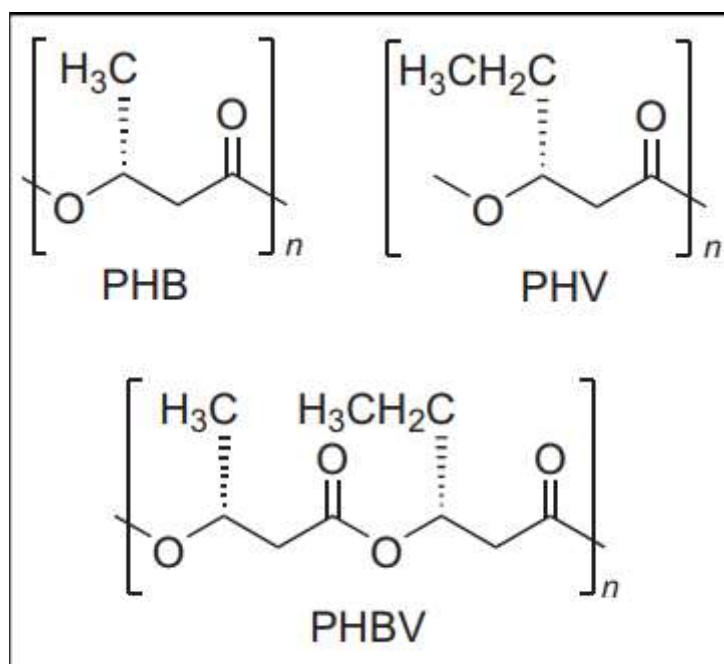


Figure 1.5 Chemical formula of PHB, PHV and PHBV polymers (Ross et al., 2017).

1.8.2 Poly(ϵ -caprolactone)

Poly(ϵ -caprolactone) (PCL) is a biodegradable, semi-crystalline polyester that has main route of synthesis by ring-opening polymerization of cyclic ϵ -caprolactone. Other less common synthesize methods are radical ring opening polymerization of 2-methylene-1,3-dioxepane and condensation of 6-hydroxycaproic acid (Figure 1.6) (Ross et al., 2017). As the molecular weight of the synthesized polymer decreases, its crystallinity increases. PCL is a hydrophobic polymer that has high stability in body. The degradation of PCL under physiological conditions occurs by random hydrolysis ester cleavage and complete degradation of PCL can prolong up to two years (Sabir et al., 2009). PCL polymer is highly used to form bone tissue engineering scaffolds due to its biocompatibility, biodegradability and mechanical stability. The high mechanical strength of PCL can be used to improve overall mechanical properties of scaffolds as used in blends with other polymers (Patrício et al., 2013).

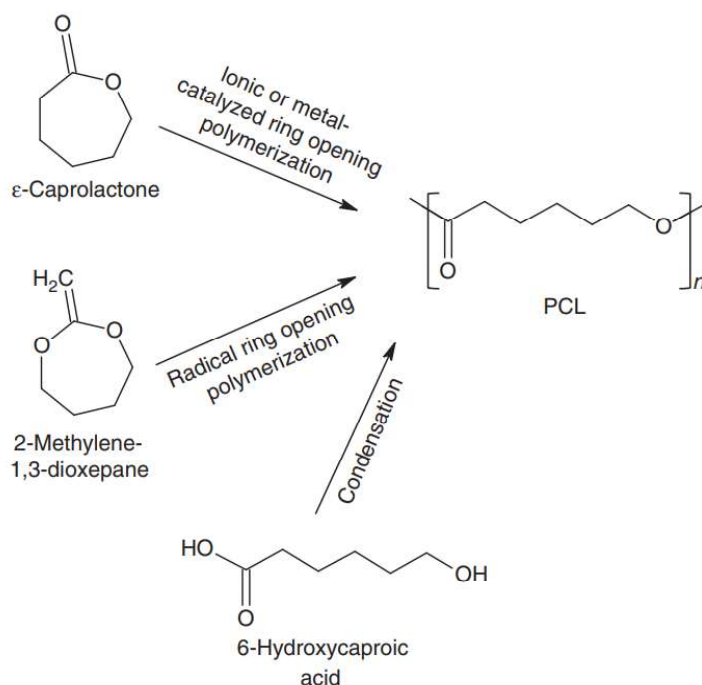


Figure 1.6 Chemical synthesis routes of PCL (Guarino et al., 2002).

1.8.3 Pullulan

PUL is a natural polysaccharide produced and secreted out of the cell by *Aureobasidium pullulans*, a fungal species (Figure 1.7). This natural polymer, which is widely used in areas such as tissue engineering and drug release, is not toxic, immunogenic or mutagenic and has no carcinogenic effects. PULs' properties like high solubility, biodegradability, ability to form thin transparent film in water, adhesion to surfaces etc. make this polysaccharide preferable for tissue engineering applications (Cheng et al., 2011; Mishra et al., 2011). In the literature, polysaccharides are divided into three groups according to their electrospinning characteristics; i) which can create jet and fiber, ii) cannot form a jet and iii) cannot create fiber. It was determined that PUL was a highly electrospinnable polysaccharide. It is also known that it can be subjected to electrospinning by using only water as a solvent (Islam et al., 2010; Stijnman et al., 2011). In addition, it has been seen in previous studies that PUL, which can be transformed into thick fibers by electrospinning, increases the thickness of the electrospun fiber matrix and adds 3 dimensions to the structure (Atila et al., 2016). In order to ensure that the structure does not deteriorate very quickly due to the PUL fibers to be used in scaffold, the cross-linking methods with have been proposed in the literature.

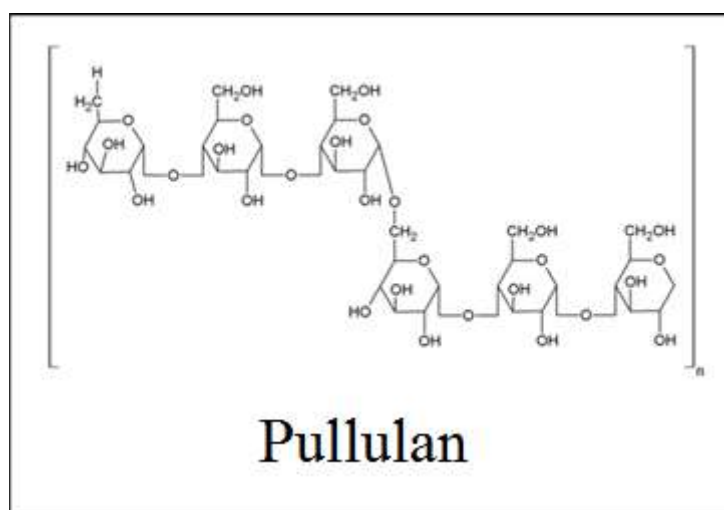


Figure 1.7 Chemical formula of Pullulan (Ferreira et al., 2015).

Studies have shown that PUL does not affect calcium absorption and bone mineral content in mice (Tsukimura et al., 2009). Also a porous scaffold bearing crosslinked PUL was shown to sustain necessary porosity for bone tissue growth (Lalande et al., 2011). In addition, in vivo studies of nano-hydroxyapatite loaded PUL composite matrices have been shown to induce high mineralization in tissue and higher bone regeneration in direct contact with the matrix (Fricain et al., 2013). Therefore, the use of PUL polysaccharide in bone tissue scaffold is promising to obtain improved bone regeneration and bone tissue formation.

1.9 Local Treatments of Bone via Drug Delivery from Bone Implants/Scaffolds

Local delivery of osteoinductive agents is a strategy that is used to improve treatment potential of synthetic bone tissue scaffolds. Biomaterials releasing compounds like growth factors, hormones and drugs have been developed and aimed to be an effective alternative to autogenous bone grafts. Local delivery of a compound enable delivery of high doses/amounts at the target site while eliminating the risk of systemic overdose and minimizing systemic side effects (Martin & Bettencourt, 2018). Growth factors like bone morphogenetic proteins (BMPs) are compounds of interest for local delivery at bone tissue for increasing osteogenic activity. BMPs belong to transforming growth factor-beta (TGF- β) superfamily and BMP-2, BMP-3, BMP-4 and BMP-7 are the ones mostly studied (Anusuya et al., 2016). Vascular endothelial growth factor (VEGF) which has role in upregulation of BMP-2 was also explored for local delivery (Khojasteh et al., 2016). Platelet lysate which contains growth factors and bioactive molecules that induce bone repair is another compound that was investigated for local delivery (Babo et al., 2016). Hormones and phytohormones as estrogens, growth hormones and thyroid hormones that has direct effects on bone metabolism are being used to improve regeneration of bone by local delivery (Martin & Bettencourt, 2018). Drugs with specific activity on bone cells

and metabolism have been used for local delivery in many studies. Some of the examples are; Alendronate, that inhibits the osteoclasts activity on bone and increases osteoblastogenesis while upregulating BMP-2, ALP, COL1 and osteocalcin (OCN) gene expression (Tenenbaum et al., 2002), Simvastatin, known to increase BMP-2 expression (Y. S. Liu et al., 2014), and Raloxifene, which has effects similar to estrogen on bone (Maximov et al., 2013). Antibiotics are another important class of drugs used for local therapy for bone tissue against infections and some antibiotics also have direct effect on bone metabolism (Martin & Bettencourt, 2018). Antibiotic treatment prior to and after a surgery is necessary to prevent any possible infection. Systemic antibiotic application is the main route of antibiotic therapies. In order to improve local concentration and effect of antibiotics, local antibiotic delivery is applied alongside with systemic antibiotic therapy. Antibiotic loaded biomaterials as local antibody delivery systems were used to prevent and treat bone infections. As an example, many studies have confirmed that the use of antibiotic loaded cement alongside systemic antibiotic treatment is reducing the risk of infection compared to only systemic antibiotic treatment (Chiu et al., 2002; Uçkay et al., 2013). In the study of Logoluso et al., effectiveness of gemcitabine and vancomycin loaded calcium phosphate bone substitutes as an implant coating was evaluated with a clinical study and reported successful prevention of infection (Logoluso et al., 2016). Collagen sponges loaded with antibiotics like Gemcitabine have reported to be used in the treatment of chronic osteomyelitis (van Vugt et al., 2018). Antibiotics can be easily loaded into electrospun fibers by electrospinning of antibiotic dissolved polymer solutions. Local delivery of antibiotics from antibiotic loaded electrospun fibers as an implant coating surface was reported as a method to prevent possible infections and improve implant tissue interaction by improved cell viability and bone regeneration by electrospun mat surface (Puppi et al., 2011; L. Zhang et al., 2014). The chronic infection of bone tissue, chronic osteomyelitis, can cause serious bone tissue damage and tissue loss. In the treatment of chronic osteomyelitis, surgery is necessary to eradicate bone infection. In order to remove infection and support the dead space in the infection site, antibiotic loaded grafts,

beads and ceramic systems are necessary (Ikpeme et al., 2010). Especially in the treatment of this disease, a local antibiotic releasing scaffold would improve the treatment completely. Some antibiotics have very short serum half-life and low oral absorption which results in low tissue accumulation and loss of effect in vivo (Finn et al., 1987; Scott et al., 2001). Local delivery of such antibiotics would improve the bioavailability and local dose of antibiotic in the target location that achieves therapeutic concentration at the disease site and prevents possible systemic side effects.

1.10 Aim of the study

In this thesis, a novel 3D scaffold for bone tissue engineering was produced by co-electrospinning of hydrophilic and hydrophobic fibers (Figure 1.8). This natural and synthetic polymer combination (PUL, PHBV and PCL) was used together for the first time in a scaffold system. The aim of using hydrophilic PUL and hydrophobic PHBV/PCL fibers was to tailor degradation and bioactivity of the scaffold. The PUL fibers dissolve faster and gradually opens spaces for tissue ingrowth and circulation of nutrients/wastes while PHBV/PCL fibers stay undissolved maintaining mechanical stability and structure of the scaffold for longer period. One of the aims was to use materials with natural origin; PHBV, pullulan polymers and Diatom silica shells (DS) in order to benefit from biocompatibility of natural materials. For the first time DS was electrospun within a polymer solution to be incorporated in a scaffold by this study. DS was achieved to be covered by polymer coating and encapsulated by polymer in line with the electrospun fiber. As part of the study, PHBV was produced by *Cupriavidus necator* bacterial strain and used to produce co-electrospun scaffold for comparison with scaffolds produced by commercially obtained PHBV. In the literature, PUL was electrospun in polymer blends to prevent its fast dissolution and loss. In order to produce stable singular PUL fibers, a novel crosslinking strategy is proposed and for the first time stable singular PUL fibers used to form a scaffold. PHBV/PCL fibers were used as a platform for loading and

release of a hydrophobic antibiotic and showed that scaffold with dual fiber characteristics can enable loading of drugs with the specific character in individual fibers.

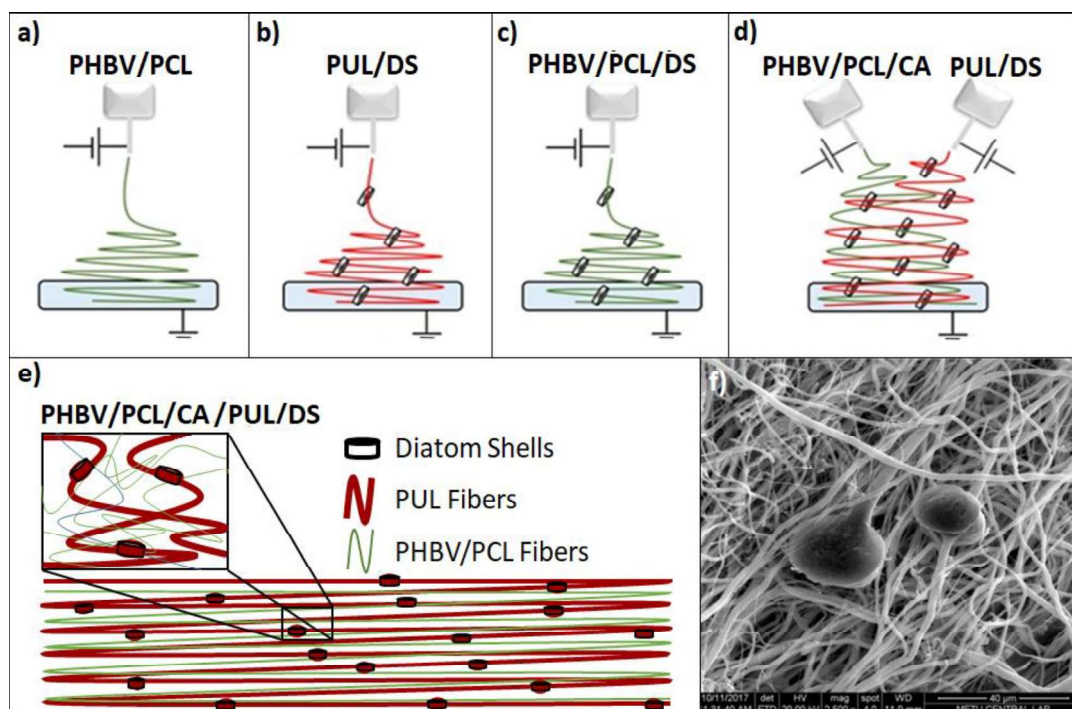


Figure 1.8 Schematic illustration of electrospinning systems of scaffold groups; PHBV/PCL (a), PUL/DS (b), PHBV/PCL/DS (c), PHBV/PCL/CA:PUL/DS (d). Schematic illustration of co-electrospun PHBV/PCL/CA:PUL/DS scaffold (e). SEM image of co-electrospun PHBV/PCL/CA:PUL/DS scaffold (f).

CHAPTER 2

MATERIALS AND METHODS

2.1 Materials

Poly (ϵ -caprolactone) (PCL) were used in the commercial form for the preparation of scaffolds. Commercial PHBV (8 mol%) polymer was purchased from Aldrich (Missouri, USA) for optimization studies and also synthesized by Prof. Dr. Ayten Karaştaş Yazgan's lab group for other studies. PUL (200 kDa) was gift from Hayashibara Inc. (Okayama, Japan). PCL (Mn: 80000), glutaraldehyde, DMSO, Triton x-100, LB medium, bacteriological agar, yeast extract, citric acid and glucose solution were taken from Sigma (Missouri, USA). Fresh water diatom silica shells were originated from Peru (Food grade). Cefuroxime axetil was kindly supplied by Bilim Pharmaceutical Co. (Istanbul, Turkey). 1,1,1,3,3,3-Hexafluoro-2-propanol (HFIP) and ethanol absolute were the products of Merck (Darmstadt, Germany). PHBV was synthesized by *Cupriavidus necator* (DSMZ 428) bacterial strain. For *in vitro* cell culture studies, human osteosarcoma (Saos-2) cell line and mouse fibroblast cell line (L929) were used. For *in vitro* studies, Dulbecco serums modified eagle medium, (DMEM, high glucose), trypsin-EDTA, penicillin streptomycin, L-ascorbic acid, L-glutamine and fetal bovine serum were used.

2.2 Production, Purification and Characterization of Synthesized PHBV

2.2.1 PHBV Production by *Cupriavidus necator*

The production studies of PHBV from bacterial strains were conducted by study group of Prof. Dr. Ayten Yazgan Karataş at Istanbul Technical University and sent to Middle East Technical University for purification and characterization of the polymer. PHBV production potential of *Cupriavidus necator* (DSMZ 428) was investigated. The growth conditions were adopted from the study of El-Sayed et al (Azhar et al., 2009). *C. necator* was incubated both in broth (Shaking at 150 rpm) and agar media for 48 h at 30°C. Inoculum (5%) from the bacteria grown in broth was transferred into polymer production medium (Glucose, 10 g/L; (NH₄)₂SO₄, 1 g/L; KH₂PO₄, 1.5 g/L; Na₂HPO₄·12H₂O, 9 g/L; MgSO₄·7H₂O, 0.2 g/L; minimum essential elements solution, 1 ml. 10 mg/L ZnSO₄·7H₂O; 3 mg/L MnCl₂·4H₂O; 30 mg/L H₃BO₃; 20 mg/L CoCl₂·6H₂O; 1 mg/L CuCl₂·6H₂O; 2 mg/L NiCl₂·6H₂O; 3 mg/L NaMo₇O₄·2H₂O) and incubated for 48 h while shaking at 150 rpm at 30°C. Then the pellet was precipitated by centrifugation at 13 000 rpm for 5 min and dyed with 0.003% Sudan Black B solution. Pellet was washed with dH₂O and dried for 2 days at 80 °C followed by 2 days incubation under vacuum.

2.2.2 Optimization of PHBV Production by *Cupriavidus necator*

PHBV production with *Cupriavidus necator* (DSMZ 428) strain was successfully achieved by using a mineral medium (Mineral Medium: 6.7 g/L Na₂HPO₄·2H₂O; 1.5 g/L KH₂PO₄; 1 g/L (NH₄)₂SO₄; 0.2 g/L MgSO₄·7H₂O; 0.01 g/L CaCl₂·2H₂O; 0.06 g/L Fe(NH₄)₂(SO₄)₂; 1 ml/L minimum essential elements solution. minimum essential elements solution: 0.3 g/L H₃BO₃; 0.2 g/L CoCl₂; 0.1 g/L ZnSO₄·7H₂O; 0.03 g/L MnCl₂·4H₂O; 0.02 g/L NaMo₇O₄·2H₂O; 0.02 g/L NiCl₂·6H₂O; 0.01 g/L CuSO₄·5H₂O) that was reported in the literature was used (Berezina, 2012). Briefly, an inoculum of 5% from *C. necator* that was grown on nutrient agar petri was

transferred to rich mineral medium (100 ml) that has additional 10 g/L glucose and 10 g/L glutamate and incubated for 24 h while shaking at 150 rpm at 30°C. A 5% inoculum was transferred into mineral medium that contains additional 1 g/L sodium propionate and incubated for 48 h at 30°C. The pellet was collected as described.

2.2.3 Isolation and Purification of Synthesized PHBV

The purified PHBV polymer was obtained after separation and purification steps (Figure 2.1). In order to completely disintegrate bacterial cells, pellet was incubated overnight in 0.1% SDS solution while stirring. After collecting of pellet by centrifugation at 8000 rpm for 12 min, pellet was transferred in (30%) sodium hypochlorite solution and incubated in 60 °C water bath for 3 min. Then pellet was precipitated by centrifuge and washed with dH₂O and acetone:ethanol (1:1) solution for 2 times. Then for PHBV extraction pellet was dissolved in chloroform and boiled at 50 °C for 5 h in condensation system, followed by stirring at RT for 16 h. Undissolved materials were removed by filtration and cold methanol was added drop wise to chloroform solution to precipitate purified PHBV. This step was repeated to collect purified PHBV (Rambo et al., 2012; Shishatskaya & Volova, 2004; Wilkinson, 2015).

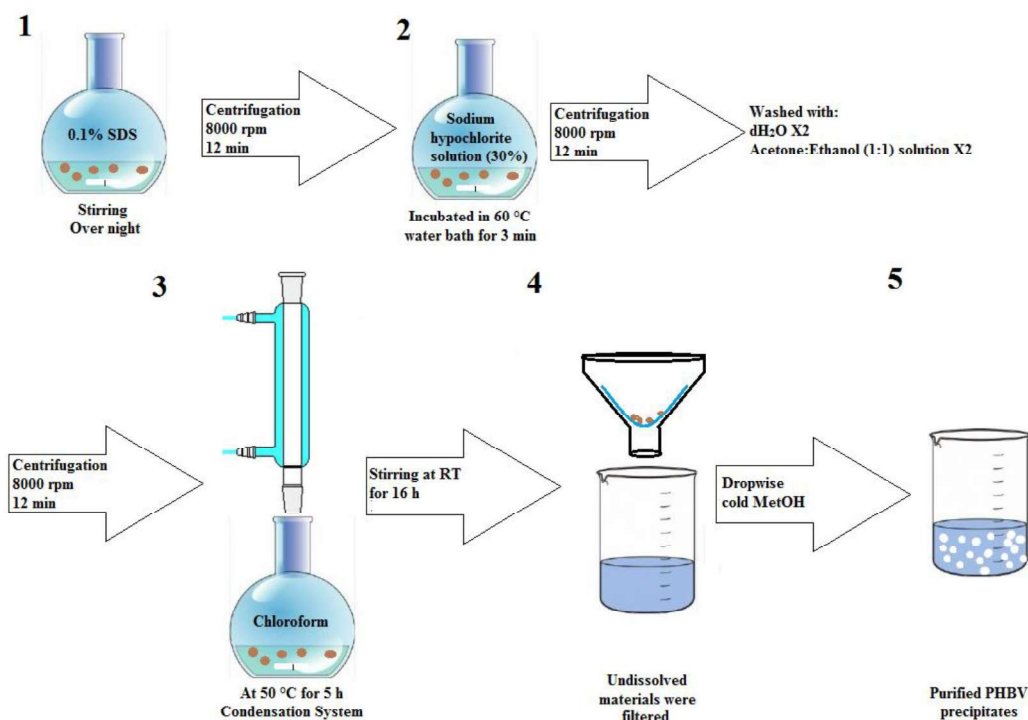


Figure 2.1. Schematic illustration of separation and purification steps of PHBV polymer which produced by bacteria.

2.2.4 Characterization of Produced Synthesized PHBV

2.2.4.1 Hydrogen Nuclear Magnetic Resonance (H-NMR) Analysis

The chemical structure of commercial and produced PHBV was investigated by H-NMR analysis. Experiment was performed with high performance super conductive magnet with active shield (Ultrashield™ 300 MHz), 5 mm BBO 1H prob and 300 MHz high definition digital H-NMR spectrometer device (Bruker Biospin, USA). Analysis was performed on 40 mg of PHBV polymer sample that dissolved in deuterated chloroform (CDCl_3).

2.2.4.2 Calculation of Valerate Percentage

Percentage of valerate content of produced PHBV was calculated from H-NMR graph of PHBV by using areas under the peaks of valerate specific group (CH₃; at 0.9 ppm) and butyrate specific group (CH₃; at 1.3 ppm). The basic steps of the method are as follows: The relative mole percentage of valerate groups are calculated by dividing integral value of valerate specific CH₃ group to the number of protons of that group, which is 3. The same calculation was done for the butyrate specific CH₃ group. The valerate percentage was calculated with the formula:

$$\text{Mole \% of valerate in PHBV} = \frac{(\text{Relative moles of valerate copolymer})}{(\text{Sum of relative moles of valerate and butyrate})} \times 100 \quad (1)$$

2.2.4.3 Determination of Molecular Weight by Static Light Scattering Analysis

PHBV stock solutions were prepared in chloroform (30 mg/mL) for static light scattering analysis. Samples were analyzed at four different dilutions between 30 to 150 degree angles with steps of 10 degrees at 20°C. Analysis was performed as triplicates for 10s at each angle point. Refractive indexes of the samples were measured, and dn/dc values were calculated. Results were obtained by Guinier plot.

2.2.4.4 Fourier Transform Infrared Spectrophotometer (FTIR) Analysis

FTIR analysis was performed with PerkinElmer L1050002 series spectrophotometer (PerkinElmer, Inc., UK, METU, Central Laboratory). The software program was run in the 100/100 N spectrum in transmission mode. The analysis was carried out in between 4000-400 cm⁻¹ wavenumbers, with a resolution of 4 cm⁻¹, with a total of 50 scans per sample. The samples were pounded with mortar and mixed with KBr at a ratio of 1:10 to measure. Samples spectrum were corrected for background and atmosphere.

2.2.4.5 Differential scanning calorimetry (DSC) Analysis

The thermogravimetric analyzes of the synthesized and commercially available PHBV samples were performed at the DSC instrument (Perkin Elmer DSC Diamond, USA) in the METU Central Laboratory at a temperature range of -20 ° C to 240 ° C and at a heating rate of 10 ° C / min.

2.3 Purification and characterization of DS

2.3.1 Purification and Pulverization of DS

In order to separate original size DS from fragmented shells, several washing steps were applied. Briefly, DS were dispersed in dH₂O and heavier particles that formed by aggregation of DS fragments were precipitated by 3 min incubation. After removal of bigger particles, DS in original size and shape were precipitated by 30 min incubation. After 30 minutes, floating particles were removed with supernatant leaving original sized DS as precipitated. In order to sterilize DS and remove any possible organic material, DS were incubated 200 °C for 1 h. Morphology of collected DS were examined under light microscopy to verify purification.

In order to decrease the size of DS and obtain DS particles with different size diameters two different methods were used. First method was to dismember DS by chemical fractionation method. The DS were regularly stirred in the NaOH solution (0.2 M, 20 mL) at 95 °C for 3 h and DS sizes were reduced (Suroy et al., 2014). In the second method, agate grinder (RETSCH RS-200 Disc Agate Grinder, Germany) in METU Central Laboratory was used to disintegrate DS skeletons in different sizes. Samples were milled in the apparatus for 1, 5, 10 and 15 min to obtain different size ranges.

2.3.2 Morphology and Size Analysis of DS

Scanning electron microscopy (SEM, Quanta 400 F Field Emission, FEI, USA) was used to examine morphology of DS. Gold and palladium coating were applied by sputter coating (Anatech Hummle VII, Istanbul, Turkey). Diameter of randomly selected DS particles were measured from SEM images to calculate average diameter of DS. Measurements were performed using ImageJ software (National Institutes of Health, Bethesda, USA). After the grinding of DS, particle size distribution was analyzed with laser scattering method using Zeta sizer (Nano ZS90, Malvern Instruments, METU Central Laboratory).

2.3.3 Chemical Characterization of DS

Energy Dispersive X-Ray Analyzer was used to determine elemental composition of DS during scanning electron microscopy imaging. The instrument used for imaging has electron probe micro-analyzer (JEOL, JXA – 8230, U.S.A.) Elemental analysis was also carried out with Electron Spectroscopy for Chemical Analysis (ESCA) at METU Central Laboratory. Surface elemental composition was determined with PHI 5000 VersaProbe. As the X-Ray source, Al K α anode was used at 26 W power and 200 μ m beam size. Measurements were taken at 45 degree starting angle. In order to prevent charge build up, 187.85 eV electron cloud blaster was used.

2.4 In Vitro Cytotoxicity Analysis of DS

Human osteosarcoma cell line (Saos-2) was used for *in vitro* cell viability analyses. *In vitro* cytotoxicity analysis of DS was performed in several different experimental designs. MTT assay was used to measure cell viability for direct contact cytotoxicity experiment of DS. In this experiment DS particles at determined concentrations were placed at the bottom of the wells. MTT method was chosen since no replacement or rinsing step that may lead to removal of DS, was needed. Groups were incubated in

regular cell culture medium (High glucose Dulbecco's modified Eagle medium, DMEM, 10% FBS, 1% penicillin/streptomycin) overnight at 37°C, prior to cell seeding. Cells were incubated in carbon dioxide incubator with 5% CO₂ and 95% humidity at 37°C. Cells were passaged at 80-90% confluency with 0.1% trypsin-EDTA solution. DS were sterilized by dry heat at 200°C for cell culture experiments.

2.4.1 MTT Cell Viability Assay

MTT (3-(4,5-dimethylthiazol-2-yl)-2,5-diphenyl-tetrazolium bromide) (Sigma Aldrich, USA) assay was used to determine cell viability in direct contact experiments of DS. In this test, metabolically active cells produce dehydrogenase enzyme at their mitochondria and turn yellow tetrazolium salt into purple formazan crystals. Experimental groups were incubated with cells and at determined time points MTT solution (5 mg/ml) that was prepared in DMEM without phenol red was added at 10% concentration to wells. Following incubation for 4 h media was removed and formazan crystals that were formed in cells cytoplasm were dissolved in DMSO. The optical density change was quantified with microplate reader (μ Ouant™, Biotek Instruments Inc., USA) at 570 nm wavelength.

2.4.2 Indirect Cell Viability Assay of DS

The cell seeding density was 3000 cells/well in 96 well plate. Both ground and original DS were incubated in regular medium as a stock at 50mg/mL concentration. Stock was incubated at 37 °C for 1, 3 and 7 days. After incubation period extract was filtered by 0.22 μ m syringe filter. The concentration groups 3.12, 6.25, 12.5 and 25 mg/mL DS were prepared from the medium that was incubated with DS and cells were cultured in these media. Through the experiment media were replenished with the media that was in contact with DS. MTT analysis was performed to compare cell viability.

2.4.3 Direct Cell Viability Assay of DS

In order to determine optimum dose of DS that will be incorporated into scaffolds and best polymer combination, a direct contact cell viability experiment was conducted. PHBV and PHBV/PCL polymer films with different DS concentrations (0, 3, 6, 12 and 25 $\mu\text{g/mL}$) were prepared by firstly dissolving polymers in 1,1,1,3,3,3-Hexafluoro-2-propanol (HFIP) and adding and mixing DS homogenously. After evaporating HFIP solution formed polymer films were incubated in 70% ethanol for 2 h and subjected to UV light for 30 min. prior to cell culture experiment for sterilization. Before cell seeding, polymer films were incubated in regular growth media in 48 well plate overnight to check sterility. Film groups were seeded with Saos-2 cells (3×10^4 cells/ 0.95 cm^2 film) and incubated for 1, 4 and 7 days. Cell viabilities were determined with Alamar Blue Assay (Alamar blue assay, Invitrogen, USA). Briefly, Alamar Blue solution (10%) was prepared in DMEM without phenol red. At determined incubation time points, media were removed from wells and films were incubated in 0.5 mL Alamar Blue solution for 6 hours. Then, Alamar blue solution of each sample was transferred into a new well and the optical densities were determined with microplate reader at 570 and 600 nm wavelengths. Membrane groups were then washed with sterile phosphate buffered saline (PBS, 0.01M, pH: 7.4) and incubations continued in regular growth medium. Percentage reduction of Alamar Blue solution for experimental groups was calculated according to manufacturers' guidelines. The results are presented as relative Alamar Blue reduction in graph as percentage Alamar Blue reduction of TCP group was accepted as 100%.

2.5 Production of 3-D Fibrous Bone Tissue Engineering Scaffold Groups

2.5.1 Electrospinning of Control Group Scaffolds

The groups with single fiber phase (PHBV/PCL, PHBV/PCL/CA and PHBV/PCL/DS) were prepared by wet electrospinning (Figure 2.2). Polymer solution (14% wt/v) of PHBV/PCL (7/3 wt/wt) was prepared in HFIP solution and polymer to DS ratio was 20/1 in DS containing PHBV/PCL/DS group. All groups were collected in ethanol bath which was placed at a distance of 15 cm from the tip of needle and under 13-15 kV electric field. Polymer solutions were delivered at 4 ml/h flow rate. The scaffold was rinsed with dH₂O until the ethanol was replaced and lyophilized at -80 °C for 2 days.

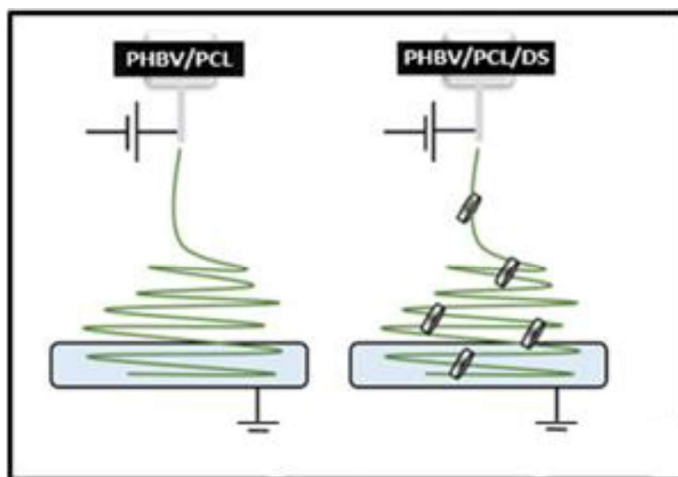


Figure 2.2. Schematic illustration of wet electrospinning system for production of electrospun PHBV/PCL (Left) and DS bearing PHBV/PCL/DS fibrous scaffolds.

2.5.2 Co-electrospinning of PHBV/PCL/CA:PUL/DS Scaffold

Co-electrospinning of PHBV/PCL/CA:PUL/DS was fully optimized by the development of an in situ crosslinking technique. Unlike electrospinning mentioned above co-electrospinning system is composed of two syringe pumps (NE-1000, New

Era, USA), two high voltage power supplies (Gamma High Voltage Source ES30) and one rotating bath collector. The system is built up vertically that enables collecting of fibers into an ethanol bath (Figure 2.3).

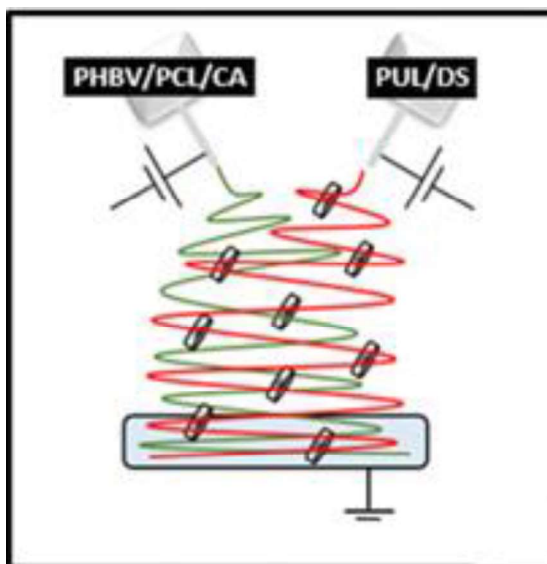


Figure 2.3. Schematic illustration of wet co-electrospinning system for production of PHBV/PCL/CA:PUL/DS scaffold.

The first polymer solution was prepared by dissolving PUL (15%) in dH₂O. The crosslinking agent glutaraldehyde (GTA) was added to PUL solution; at 1/3 wt ratio of PUL and p-toluene sulfonic acid (0.1%) was added to sustain acidity (pH: 4). GTA and p-toluene sulfonic acid were also added into the collector ethanol bath in order to sustain same concentrations of crosslinking agents after fiber formation. The PUL solution was stirred for 1 h at 60 °C to initiate crosslinking prior to co-electrospinning. Then DS were added into PUL solution (PUL/DS, 10/1, wt/wt) and distributed homogeneously just before the co-electrospinning. The second solution was prepared by dissolving PHBV/PCL (7/3, wt/wt) (Total Polymer concentration: 14%) in HFIP solution. The CA was added to this solution at 2.5 mg/mL concentration. Distance between syringes and ethanol bath collector was set to be 18 cm. PUL/DS solution was electropun with 3 ml/h flow rate at 15 kV and PHBV/PCL/CA solution was electropun with 3 ml/h at 13kV into same ethanol bath

collector. The scaffold was rinsed with dH₂O until the ethanol was replaced and lyophilized at -80 °C for 2 days. Excess GTA was removed from scaffolds by mounting mats in laminar flow hood at RT for 24 h.

2.5.3 Production of B-PHBV/PCL/CA:PUL/DS Scaffold Using B-PHBV

The three-dimensional scaffold containing two fiber bearing CA and DS were re-prepared with B-PHBV according to method described above (Co-electrospinning of PHBV/PCL/CA:PUL/DS Scaffold) which was produced and characterized by synthesized PHBV in place of commercial PHBV. The first polymer solution was prepared using the same PUL and DS components and ratios. As the second polymer solution, a blend of B-PHBV/PCL (7/3, wt/wt) polymers was prepared at a concentration of 10% in HFIP. For the production of antibiotic loaded fibers, CA was added to the B-PHBV/PCL polymer solution.

2.6 Characterization of Scaffolds

2.6.1 Scanning Electron Microscopy Analysis

The morphology of produced scaffolds was observed by SEM analysis. Prior to analysis, scaffolds were coated with 10 nm gold/palladium layer with sputter coating (682 PECS, Gatan, Inc., USA). Then images were taken with SEM (FEI, Nova Nano SEM 430, USA, METU Central Laboratory).

2.6.2 Pore Size Distribution and Porosity Analysis

Pore size distribution and porosity analysis of scaffold groups were performed in METU Central Laboratories (Ankara, Turkey). Mercury Porosimeter (Coremaster 60, Qunatochrome Cooperation, Florida, USA) and Helium Ultrapycnometer 1000 (Quantachrome Corporation, Florida, USA) were used to determine pore size

distribution and overall porosity of scaffolds. Measurements were performed under low pressure at 0–50 psi per 200–4 μm diameter.

2.6.3 Weight Loss, Enzymatic Degradation and Water Retention Analysis

For the weight loss analysis, scaffold groups were prepared to have similar weights and shapes (Cylindrical, $1 \times 1 \text{ cm}^2$, diameter \times height). Samples were incubated in 4 mL PBS (0.01 M, pH 7.4, with 0.1% sodium azide); in shaking water bath (Nüve Bath NB 5, Turkey) for 21 days at 37 °C. At determined time points, samples were rinsed with dH₂O and dried by freeze-drying (Labconco Corporation, Kansas City, USA). The weights of the dried samples were also measured. The percent weight loss was calculated according to their initial weights.

The weight loss of scaffolds were also analyzed under enzymatic degradation. Scaffold groups were prepared to have similar weights and shapes. Samples were incubated in lysozyme solution (1 mg/mL) prepared in PBS (0.1 M, pH 7.2, 0.01% sodium azide); in shaking water bath (Nüve Bath NB 5, Turkey) for 14 days at 37°C. In determined time points, samples were rinsed with dH₂O and dried by freeze-drying. The weights of the dried samples were measured, and percent weight loss was calculated according to their initial weights. The SEM images of degraded samples were observed to identify the structure of polymer coating on DS. The formulations that were used for calculation of weight loss:

$$\text{Weight loss (\%)} = \frac{(\text{Initial dry wt.} - \text{dry wt. at time } t)}{(\text{Initial dry wt.})} \times 100 \quad (2)$$

For the water retention analysis, scaffold groups were prepared to have similar weights and shapes (Cylindrical, $1 \times 1 \text{ cm}^2$, diameter \times height). Samples were incubated in 4 mL PBS (0.01 M, pH 7.4, with 0.1% sodium azide); in shaking water bath (Nüve Bath NB 5, Turkey) for 21 days at 37 °C. At determined time points, the

wet weights of samples were measured. Then, samples were rinsed with dH₂O and dried by freeze-drying (Labconco Corporation, Kansas City, USA). The weights of the dried samples were also measured. The percent water retention was calculated with following equation:

$$\text{Weight retention (\%)} = \frac{(\text{Wet wt. at time t} - \text{dry wt. at time t})}{(\text{dry wt. at time t})} \times 100 \quad (3)$$

2.6.4 Water Contact Angle Analysis

Water contact angle measurements of samples were made with sessile drop method using goniometer (Attension, Biolin Scientific, Sweden) at RT. Drop of dH₂O (7 μ L) was placed on three different spots on each sample. The contact angle measurements on samples were made for both sides of the drop and average contact angle values were reported.

2.6.5 Calcium Adsorption on Scaffolds

Scaffolds were cut into similar size and shape (Cylindrical, 1 \times 1 cm diameter \times height) and incubated in 3 mL of simulated body fluid (SBF) (Na⁺ 142.0, K⁺ 5.0, Mg²⁺ 1.5, Ca²⁺ 2.5, Cl⁻ 148.8, HCO₃⁻ 4.2, HPO₄²⁻ 1.0, SO₄²⁻ 0.5 mM, pH:7.4) in a shaking water bath at 37 $^{\circ}$ C (L. Li et al., 2004). The samples were taken from the SBF that was surrounding the scaffold groups after 7 and 14 days of incubation and calcium in these SBF samples was determined with calcium assay. Briefly, o-cresolphalein complexone (0.024% w/v) and 8-hydroxyquinone-5-sulfonic acid (0.25% w/v) solutions were prepared in dH₂O. Two solutions were mixed in equal volumes. A third solution was prepared by dissolving 2-amino-2-methyl-1,3-propanediol (0.5 M) in dH₂O and added to previously prepared mixture at the same volume of the mixture solution to form the reaction solution for calcium detection assay. Prior to Ca²⁺ detection, sample solutions (100 μ L) were mixed with 0.1 M HCl solution (900 μ L) in Eppendorf tubes and incubated for 1 h. Then incubated solutions

(25 μ L) were mixed with reaction solution (125 μ L) in 96 well plate. Spectrophotometer (Hitachi U-2800A, Japan) was used to measure optical density of samples at 560 nm wavelength. The decrease in the SBF calcium content was compared to zero day of incubation and the difference was considered to be due to calcium deposition amounts of the groups.

2.6.6 Cefuroxime Axetil Loading and Release Studies

The specific absorbance value for CA detection was determined by UV spectrophotometer (Hitachi U-2800, Japan) as 270 nm wavelength in ethanol. The CA release from DS only, PHBV/PCL, CA loaded DS bearing PHBV/PCL and co-electrospun PHBV/PCL/CA:PUL/DS scaffolds was compared. The loading of CA into the PHBV/PCL fiber phase of the scaffold groups was determined indirectly by measuring the unloaded CA that dissolved in the collector ethanol bath. After electrospinning of each group, samples were taken from collector bath and unloaded CA amount was determined by absorbance measurement at 270 nm wavelength microplate reader. Amount of CA was determined from CA calibration curve that was plotted with known CA concentrations in ethanol (Appendix A. Fig.1). The loaded CA amount was found by subtracting this unloaded CA amount from the initially added CA amount. CA release study was performed by placing scaffold samples into dialysis bags and incubating samples in PBS (pH: 7.4, 0.01 M, 4 mL with 0.1% sodium azide). Dialysis bag was used to eliminate any scaffold debris from getting mixed in release media and effecting optical density results. Through 21 days of incubation PBS samples were collected and incubation media was replenished. Collected samples were dried in vacuum oven and aggregate was dissolved in chloroform. The undissolved salt particles of the PBS were separated from chloroform by centrifugation. Then absorbance of the chloroform solutions was measured at 281.5 nm wavelength with UV spectrophotometer. Amount of CA

released was determined from CA calibration curve (Appendix A. Fig.2) that was plotted with known CA concentrations in chloroform.

2.6.7 Tensile and Compressive Strength Tests

Uniaxial tensile test and compressive strength test was applied to compare scaffolds strength under tensile and compressive stresses. Mechanical tests were performed with Univert biomaterial mechanical testing device (Cell scale, Canada). 10 N load cell used for the measurements in experiments. For tensile strength test preload was applied as 0.1 N and rectangular shape ($25 \times 10 \times 0.2 \text{ mm}^3$: length \times width \times thickness) samples were stretched at 0.5 mm/s rate. Compressive strength test was applied on cylindrical shaped samples of electrospun scaffolds (Diameter: 9-9.5 mm, height: 8-10 mm). Cylindrical samples were obtained by freeze-drying wet electrospun scaffolds in 48 well plate which samples took the shape of cylindrical wells. Compression was applied at 5 mm/min rate and 0.1 N preload was applied. Samples were compressed up to 40% of their initial size. Stress-strain curves were plotted and ultimate tensile strengths (UTS), or compressive strengths and Young's modulus (E) values were calculated.

2.6.8 SEM Observation of Fiber Break Points Under Tensile stress

The PUL/DS fibers were forced to break under uniaxial tensile force. Tests were performed with Univert biomaterial mechanical testing device (Cell scale, Canada). 10 N load cell used for the test. Fiber samples were stretched with 0.5 mm/s rate until break. Break point of fibers were observed under SEM.

2.7 In Vitro Cell Culture Studies

Human primary sarcoma cell line (Saos-2) was used to investigate osteocompatibility while mouse fibroblast cells line (L929) was used to assess

general cytotoxicity of scaffolds. Cells were incubated in high glucose Dulbecco's Modified Eagle Medium (DMEM) supplemented with fetal bovine serum (10%) and penicillin/streptomycin solution (1%). Cells were incubated in CO₂ incubator with 5% CO₂ at 37°C. Growth medium was replenished after 2-3 days of incubation and cells were passaged after 80% confluency reached. Scaffold samples (7 × 7 × 3 mm³, width × length × height) were sterilized with 2 h of incubation in 70% ethanol and 30 min of UV light exposure. Cells seeding density was 2.5×10⁴ cells per scaffold sample for in vitro studies. In order to obtain better initial cell attachment, all media was withdrawn from wells and cell solution was dropped on wet scaffolds. The cell solution was dropped 3 times in 20 µl volume onto wet scaffolds and in between all addition cycle, scaffolds incubated in CO₂ incubator at 37 °C for 30 min. After the 3rd cycle of cell seeding and total of 1.5 h incubation, scaffolds were transferred to a new plate and immersed in growth media. When the scaffolds were transferred into a new plate after cell seeding incubation, only the cells which were attached onto scaffolds were successfully separated for experiment from the ones that fell to the bottom of the wells.

2.7.1 Alamar Blue Cell Viability Assay

This test is based on the metabolic reduction of 7-Hidroksi-3H-fenoksazin-3-one 10-oksit (Invitrogen, USA) substrate. The cell viability of PHBV/PCL, PHBV/PCL/DS, PHBV/PCL/CA and PHBV/PCL/CA:PUL/DS scaffolds were compared after after 1, 4 and 7 days of incubation with Saos-2 and L929 cells. The scaffolds were incubated overnight in regular medium at 37 °C prior to cell seeding. Cell seeding density was 2.5×10⁴ cells/scaffold. Alamar Blue solution (10%) was prepared in DMEM without phenol red. At determined incubation time points, media were removed from wells and scaffolds were incubated in 0.5 mL Alamar Blue solution for 6 hours. After 6 hours, Alamar Blue solutions from groups were collected into a new 48 well plate and absorbance was read with microplate reader at 570 and 600

nm. Groups were then washed with sterile phosphate buffer saline (PBS, 0.01M, pH: 7.4) and incubation was continued in regular medium.

2.7.2 Determination of Alkaline Phosphatase Activity and Intracellular Calcium Amount

Alkaline phosphatase activities (ALP) of groups were determined after cells were incubated with differentiation media prepared by supplementing regular growth medium with ascorbic acid (Sigma, USA) (50 µg/mL), β-glycerophosphate (Sigma, USA) (10 mM) and dexamethasone (Merck, Germany) (10^{-8} M). At incubation time points, in order to lyse cells, plate was incubated in -80°C for 30 min and thawed at 37°C for 30 min. Same freeze-thaw process was repeated after adding PBS to sample wells (500 µL/well, 48 well plate) under shaking. Then cell lysates (75 µL) were transferred to 96 well plate with MgCl₂ solution (25 µL) and p-nitrophenyl phosphate (pNPP) solution (75 µL) and incubated for 1 h at 37°C. After incubation optical densities were measured by microplate reader at 405 nm wavelength. ALP activities were calculated from previously plotted ALP activity calibration curve. In order to calculate specific enzyme activities (nmol/µg protein/min), amount of protein content in sample groups were determined by BCA assay. Briefly BCA solution was prepared by adding Copper (II) sulfate solution (CuSO₄) to BCA at 1:50 v:v ratio. BCA solution (125 µl) and cell lysates (75 µL) of groups were collected in 96 well plate. Plate was incubated for 15 min at 60°C and optical density readings were obtained at 562 nm wavelength. Protein amount was determined from previously plotted calibration curve of BCA assay of bovine serum albumin protein. Cell lysates of the groups were used to determine intracellular calcium amount via calcium assay. Briefly, o-cresolphthalein complexone (0.024% w/v) and 8-hydroxyquinone-5-sulfonic acid (0.25% w/v) solutions were prepared in dH₂O. Two solutions were mixed in equal volumes. A third solution was prepared by dissolving 2-amino-2-methyl-1,3-propanediol (0.5 M) in dH₂O and added to previously prepared mixture at the same volume of the mixture solution to form the reaction solution for calcium detection

assay. Prior to Ca^{2+} detection, sample solutions (100 μL) were mixed with 0.1 M HCl solution (900 μL) in Eppendorf tubes and incubated for 1 h. Then incubated solutions (25 μL) were mixed with reaction solution (125 μL) in 96 well plate. Spectrophotometer (Hitachi U-2800A, Japan) was used to measure optical density of samples at 560 nm wavelength.

2.7.3 Analysis of Cell Attachment and Morphology on Scaffolds

Attachment and Morphological properties of the cells on scaffolds' surfaces were examined with SEM (Quanta 200 FEG, Netherlands). SEM images of Saos-2 cells after 7 days of incubation on PHBV/PCL, PHBV/PCL/DS, PHBV/PCL/CA and PHBV/PCL/CA:PUL/DS scaffold groups. Briefly, scaffolds with proliferated cells were immersed into 4% paraformaldehyde solution in PBS and incubated at RT for 10 minutes for fixation. Paraformaldehyde solution was removed by rinsing with PBS and in order to start drying, scaffolds were incubated in increasing concentrations of ethanol (20–100%) for 10 min cycles. For complete removal of water scaffolds were subjected to hexamethyldisilazane for 20 minutes. Hexamethyldisilazane was removed under fume hood and samples were stored in desiccator. Scaffolds were coated with gold and palladium layer prior to SEM imaging.

2.7.4 Confocal Laser Scanning Microscopy Analysis

Confocal laser scanning microscopy examination was performed on cells after 7 days of incubation on scaffold groups. Cell seeding density was 2.5×10^4 cells per scaffold sample in 48 well plate. Paraformaldehyde (4%) solution was used to fixate the cells. For permeabilization cells were subjected to 1% Triton X-100 solution for 5 min. Scaffolds were immersed in BSA solution (1% in PBS, pH: 7.4, 0.01 M) at 37 °C for 30 min to block background fluorescence. Scaffolds were immersed in FITC (1% in 0.1% BSA solution) solution for 1 h followed by removal of excess dye via PBS

rinsing. Then scaffolds were immersed in PI (1 $\mu\text{g}/\text{ml}$) for 10 min and rinsed with PBS. Confocal laser scanning microscopy (Leica DM2500, Germany) images were taken using z-stack analysis and image layers were combined to form final images.

2.7.5 Statistical Analysis

The mean and standard deviation values of all data were calculated and SPSS 22 Software (SPSS Inc., USA) program was used for the one-way ANOVA test used in the analysis of variance ($n=3$). In addition, Tukey multiple comparison analysis was performed to determine whether there was a difference between groups for $p<0.05$ significance values.

CHAPTER 3

RESULTS AND DISCUSSION

3.1 Results of Production, Purification and Characterization of PHBV produced by Bacteria

The production studies of PHBV from bacterial strains were conducted by study group of Prof. Dr. Ayten Yazgan Karataş at Istanbul Technical University and sent to Middle East Technical University for purification and characterization of the polymer. *Haloferax mediterranei* was reported to support high production of PHBV by the study of Lu et al. (Lu et al., 2008). However, as stated in the method part, efficient growth of strain cannot be achieved through trailers with various media. Then potential of *Bacillus polymyxa* to produce PHBV was investigated. The production of polymer granules in bacteria cells was observed after Sudan Black B staining. In Figure 3.1, dark blue-black dots that indicate presence of PHB granules are shown.

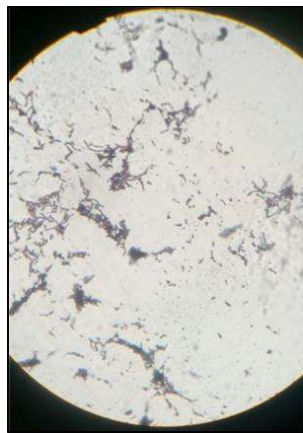


Figure 3.1. The production of polymer granules in *Bacillus polymyxa* bacteria cells was observed after Sudan Black B staining.

Collected bacteria pellet was send to METU for purification and characterization of produced polymer before use in scaffold studies. Purification study, which was also a preliminary study of producing PHBV from bacteria, was completed and the chemical structure of the obtained PHBV was examined by H-NMR. In order to verify the H-NMR peaks of purified PHBV, studies reporting H-NMR peaks of PHBV was investigated. Purified PHBV was reported to have peaks at 0.8-1.8 ppm, 2-3 ppm and 5.2 ppm (Jian Tao et al., 2009) yet after H-NMR analysis of polymer produced by *Bacillus polymyxa*, it was observed that polymer peaks were not exactly matching with peaks for PHBV (Figure 3.2).

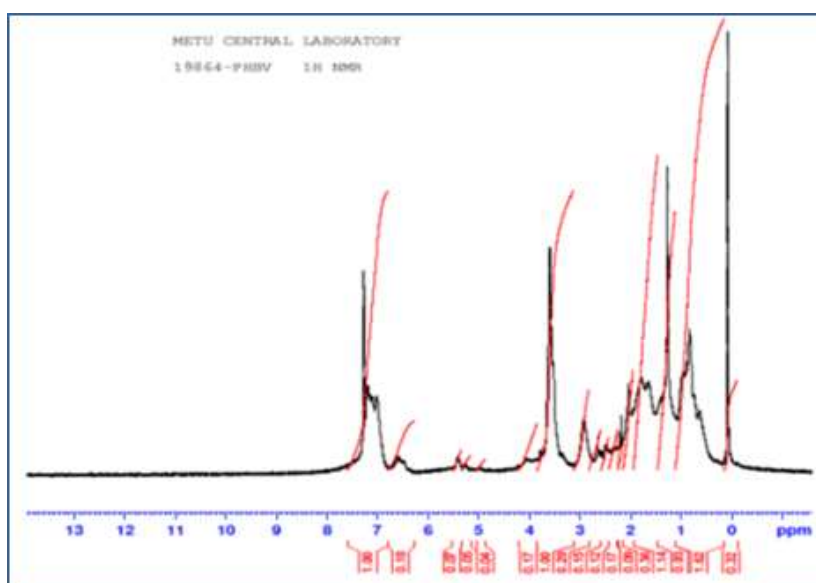


Figure 3.2. H-NMR peaks of purified polymer produced by *Bacillus polymyxa*.

Following experiments were conducted with the strain, *Cupriavidus necator* (Figure 3.3 and 3.4). Several different growth media were used to optimize PHBV production of the strain. Initial trial was adopted from the study of Wang et al. (2013) and Fe-citrate was included in MSM media (Yuanpeng Wang et al., 2013). However, H-NMR analysis revealed that produced polymer was not PHBV. The H-NMR result showed that produced polymer lacks characteristic valerate group peaks where the red arrows point in the Figure 3.3a. On the other hand, produced polymer has shown all the characteristic peaks for butyrate group. In the second trial same method was

repeated with using Fe(III)NH₄ citrate instead of Fe-citrate. However, H-NMR analysis revealed similar result indicating that produced polymer was not PHBV
Figure 3.3b.

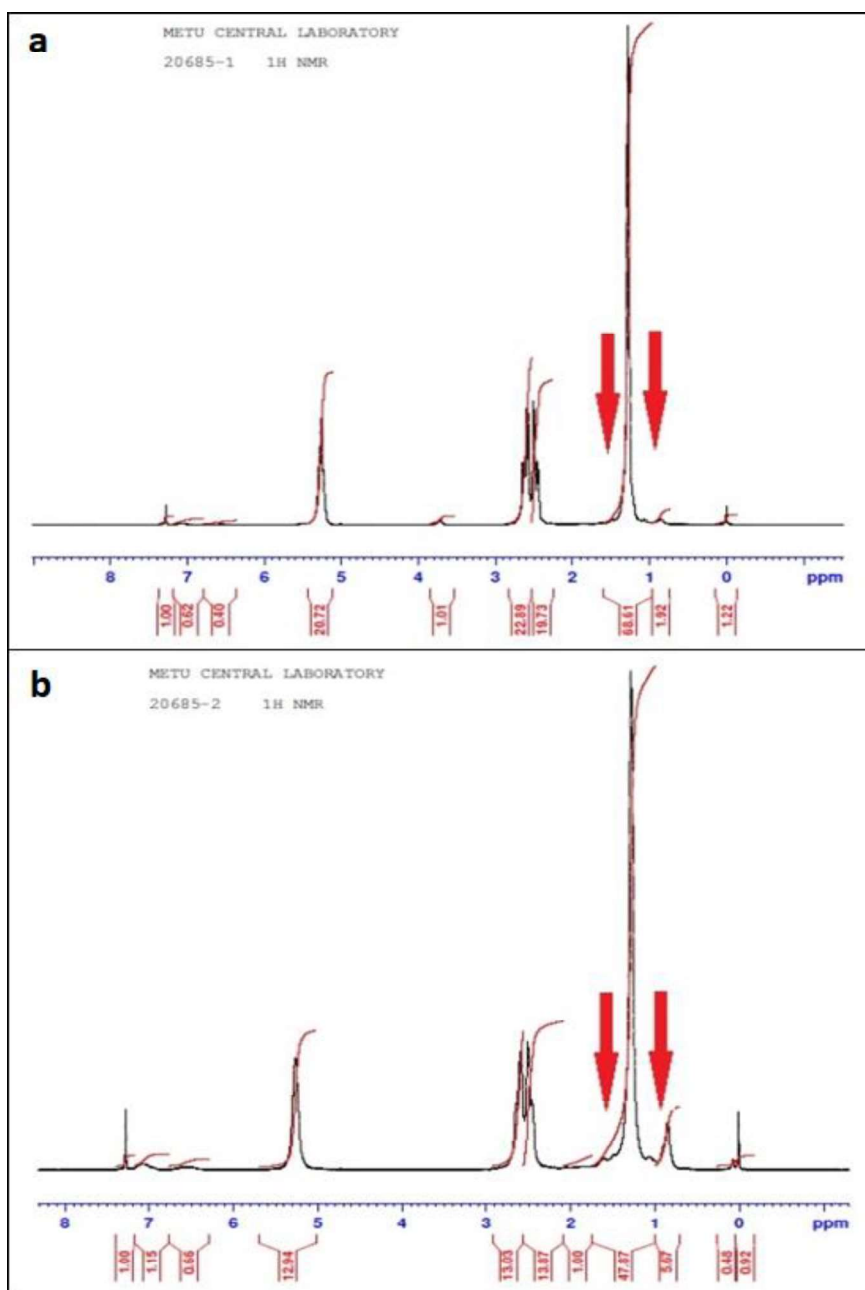


Figure 3.3. H-NMR peaks of purified polymer produced by *Cupriavidus necator*, first (a) and second (b) trials.



Figure 3.4. The production of polymer granules in *Cupriavidus necator* bacteria cells was observed after Sudan Black B staining. (400 X magnifications).

For the third trial of PHBV production, a different growth media that is defined as “mineral medium” was adopted from the study of Berezina et al. (Berezina, 2012). The H-NMR results revealed the successful production of PHBV. Both characteristic peaks of hydroxy butyrate and hydroxy valerate were identified on H-NMR graph (Figure 3.5a) (Bhattacharyya et al., 2012). The H-NMR analysis result of commercially obtained PHBV is present in Figure 3.5b which also has all the characteristic peaks of PHBV (Figure 3.5b). The scaffold group produced by synthesized PHBV is referred as B-PHBV through the study.

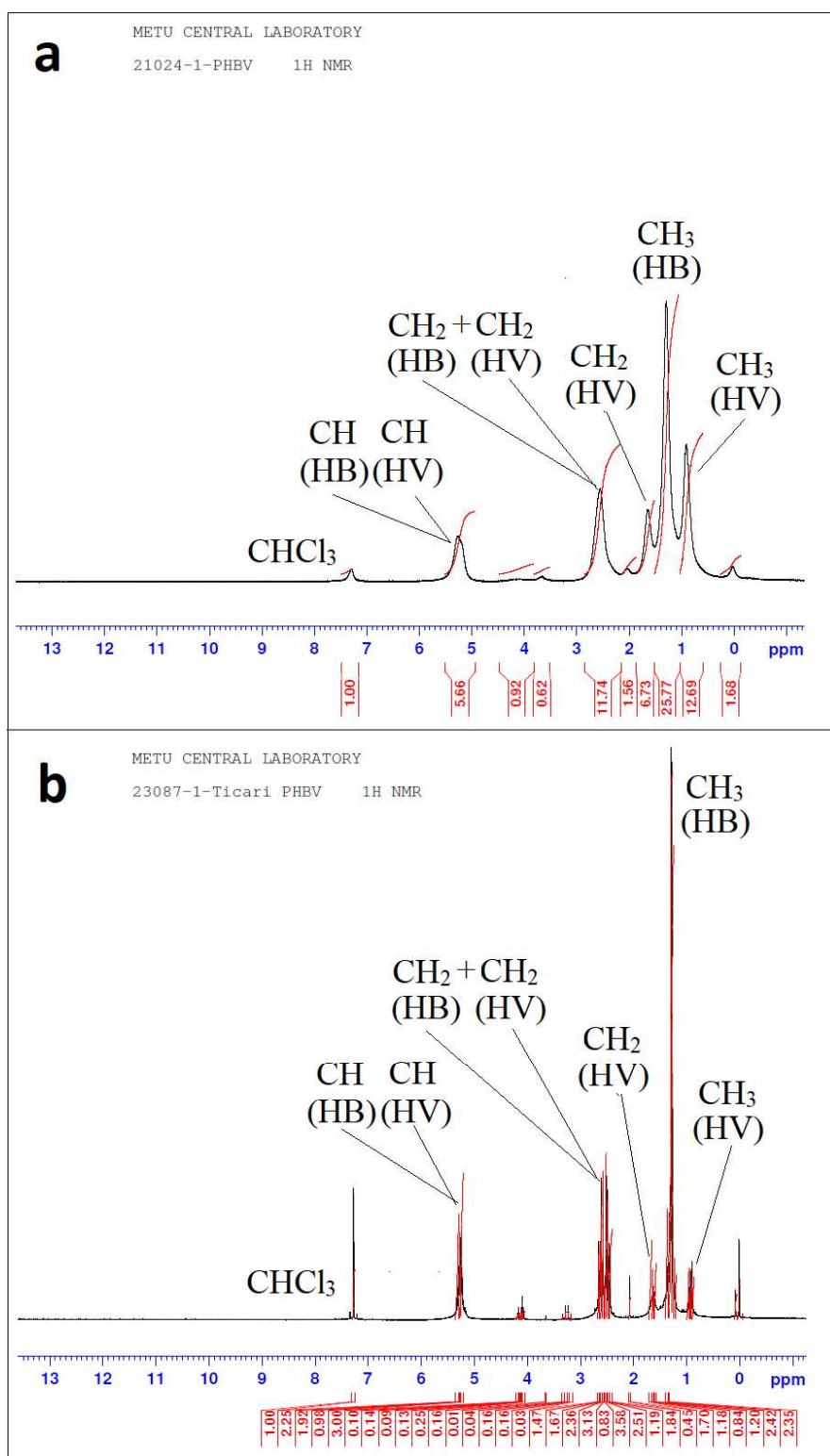


Figure 3.5. The H-NMR peaks of PHBV produced by *Cupriavidus necator* strain (a). The H-NMR peaks of commercially obtained PHBV (b).

3.1.1 Valerate Mole Percentage of Synthesized PHBV

The mole percentage of valerate component of PHBV copolymers was calculated from the H-NMR graphs as described in the method section, and the average valerate mole percentages of the different batches was found to be $8.2 \pm 2.7\%$. The valerate percentage of commercially obtained PHBV which was used in previous scaffold related experiments was reported as 8% by the supplier. The valerate mole percentage of the PHBV produced using *C. necator* bacteria was successfully reduced to the valerate percentage of the commercial PHBV. This result was considered to be important for comparison of scaffold groups produced with PHBV from two different sources.

3.1.2 Molecular Weight of PHBV Determined by Static Light Scattering Spectrometry

Molecular Weight of commercially obtained and produced PHBV was determined by static light scattering spectrometry method. In order to determine molecular weight of the polymer from static light scattering spectrometry measurements via Zimm plot, equation representing the relation between scattered light intensity and molecular weight, dependent on scattering light angle and solution concentration is used (Eqn. 4).

$$\frac{K_c}{R_\theta} = \frac{1}{M_W} \left\{ 1 + \left(\frac{16\pi^2}{3\lambda^3} \right) R_g^2 \sin^2 \left(\frac{\theta}{2} \right) \right\} + 2A_2c \quad (4)$$

In the equation, λ and R_g represent, wavelength of the laser and radius of gyration. A_2 is the second virial coefficient which is determined by the solute-solvent interactions. A_2 is a positive value when the solute-solvent affinity is greater than solute-solute affinity in good solvents (Schärfl, 2007). K represents the optical constant which changes with wavelength of scattered light (λ), refractive index increment (dn/dc), refractive index of solvent (n_0) and scattering angle (Eqn. 5).

$$K = \frac{2\pi^2 n_0^2}{\lambda^4 N_A} \left(\frac{dn}{dc} \right)^2 (1 + \cos^2 \theta) \quad (5)$$

The R_θ in the Eqn. 4 is Rayleigh ratio, which is represented with the equation dependent on incident (I_0) and scattered (I_θ) light intensities measured on specific angle (θ), scattering volume (V) and distance between detector and scattering volume (r) (Shaheen et al., 2018; Völker et al., 2016).

The method of analyzing Zimm plot to reveal molecular weight, can be understood by observing 2 parts of K_c/R_θ equation (Eqn. 4) which depend on measurement angle and concentration. When the measurement angle (θ) becomes zero, $\left\{ 1 + \left(\frac{16\pi^2}{3\lambda^3} \right) R_g^2 \sin^2 \left(\frac{\theta}{2} \right) \right\}$, the sin value becomes zero and the value of parenthesis becomes 1. Which leaves the equation to be concentration dependent, $\frac{K_c}{R_\theta} = \frac{1}{M_w} + 2A_2 c$. If the concentration is zero, then the equation becomes completely dependent on angle measurement. However, in the case of experiment, concentrations and measurement angles will never be zero. The Zimm plot is plotted with 2 different experimental sets; first set for changing concentrations at constant measurement angle and second set for changing measurement angles at constant concentration. Then the results for changing angle and concentrations were extrapolated to zero to obtain two different lines for $\theta=0$ and $c=0$. The intersect of these two lines with y axis, indicates the point where “ $\frac{K_c}{R_\theta} = \frac{1}{M_w}$ ”, since angle and concentration dependent parts of the equation is extrapolated to zero. The experimental Zimm plot is given in Figure 3.6.

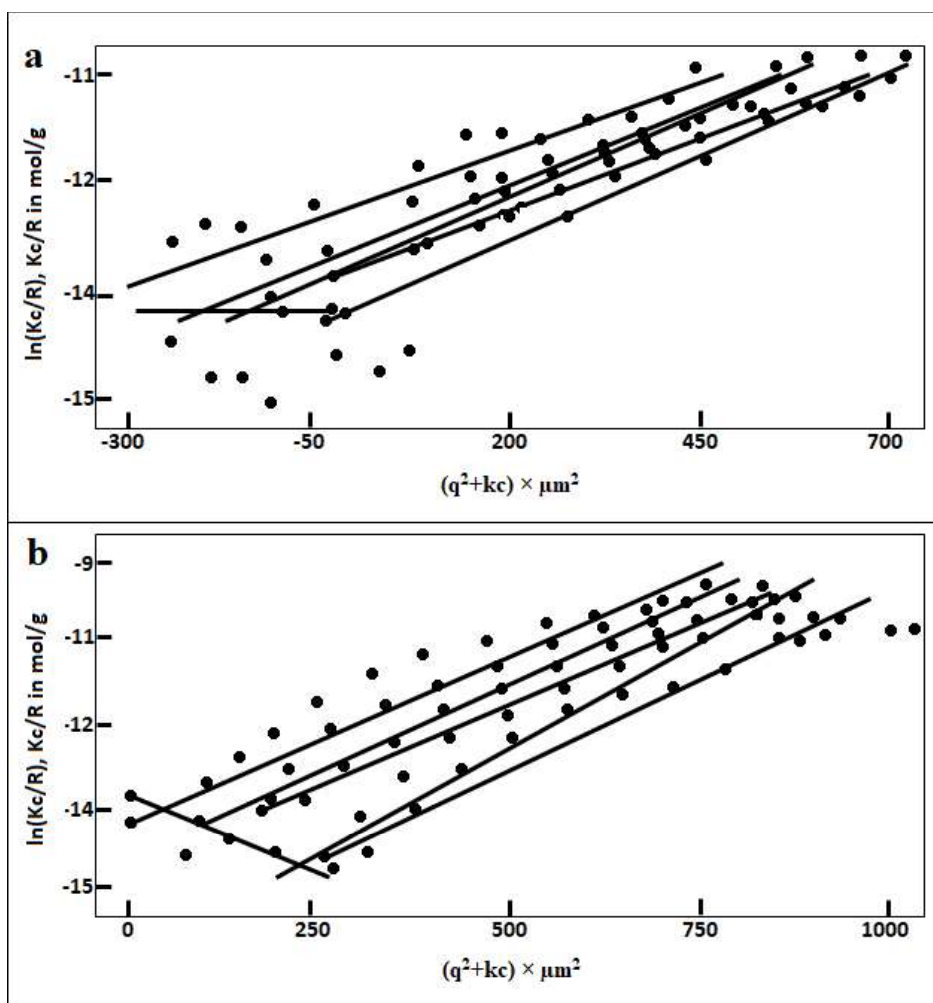


Figure 3.6. Zimm plot of static light scattering spectrometry data of commercially obtained PHBV (a) and produced PHBV (b) at different concentrations and angles.

Results have showed that commercially obtained PHBV has 778.4 kDa while produced PHBV has 611.6 kDa weight-average molecular weights. The correct interpretation of molecular weight results by static light scattering data is highly depend on obtaining a highly dilute polymer solution with no interaction between dissolved polymer chains in solvent. The second virial coefficient calculated in analyses is used to determine solution nonideality which is the reason of two body interactions in solvent. Positive second virial coefficient indicates repulsion between bodies while negative second virial coefficient indicates attraction and possible interaction of bodies in the solvent (Alford et al., 2008). The second virial coefficients

for obtained and produced PHBV was determined as -1.86×10^{-6} and -3.5×10^{-5} . The second virial coefficients for PHBV polymers are both close to zero and negative. This result indicates that there could be possible interaction between polymer chains in the solvent which will affect the static light scattering results and show a higher molecular weight values than which already are. However, results being close to zero indicates that predicted interactions could be very small or non-existent. Similar weight-average molecular weights have reported by the study of Taepucharoen et al., as 543 kDa for PHBV with 5.5 mol% HV content and 752 kDa for PHBV with 6.5 mol% HV content (Taepucharoen et al., 2017). The determined weight-average molecular weights of obtained and produced PHBV are compatible with the study of Taepucharoen et al., which supports the accuracy of the results. The molecular weight of the polymer determines the solution viscosity and while electrospinning, viscosity has a huge impact on fiber morphology. As the viscosity of the solution increase, viscoelastic forces increase which results in higher resistance against the stretching of polymer fibers during whipping motion under electric field (Nezarati et al., 2013). Higher resistance to stretching should results in fibers with increased diameter under same conditions. The molecular weight results have showed that commercially obtained PHBV has higher molecular weight compared to produced PHBV, although the difference was not large. However, commercially obtained PHBV was in the pellet form and prepared PHBV solution was formed a suspension rather than complete dissolution in the HFIP solvent. As a result of this, higher molecular weight could not create a high viscosity since the solubility of the polymer will determine the effect of molecular weight on viscosity. On the other hand, produced PHBV was able to be dissolved completely and created a viscous solution which resulted in fibers with increased diameter. The solubility difference between PHBV samples can also be identified from Zimm plot data, as data of commercially obtained PHBV is more scattered while data of produced PHBV is more in order (Figure 3.6a).

3.1.3 Results of Fourier Transform Infrared Spectroscopy Analysis of PHBV

FTIR spectrum of PHBV polymer produced from bacteria within the scope of the thesis is shown in Figure 3.7. The characteristic bands of PHBV are seen in this spectrum. The band showing the carbon-oxygen stretching is seen at 1720 cm^{-1} wavenumber and the band belonging to the carbon-hydrogen groups is seen at 2977 cm^{-1} wavenumber (Nair et al., 2015). In addition, symmetrical stretching vibrations due to carbon-oxygen-carbon bond have bands at 978, 932, 896 and 826 cm^{-1} and each is present in the spectrum (Malaquias Barboza et al., 2014). In addition, anti-symmetrical stress vibrations due to the chemical bond of carbon-oxygen-carbon groups are observed at $1060, 1101$ and 1134 cm^{-1} (Raşoga et al., 2017). Although the crystal phase specific band appears predominant at 1722 cm^{-1} wavenumber (Farago et al., 2008), the band here has a width from 1746 to 1722 cm^{-1} wavenumber, indicating that the amorphous and crystal phases coexist (Raşoga et al., 2017).

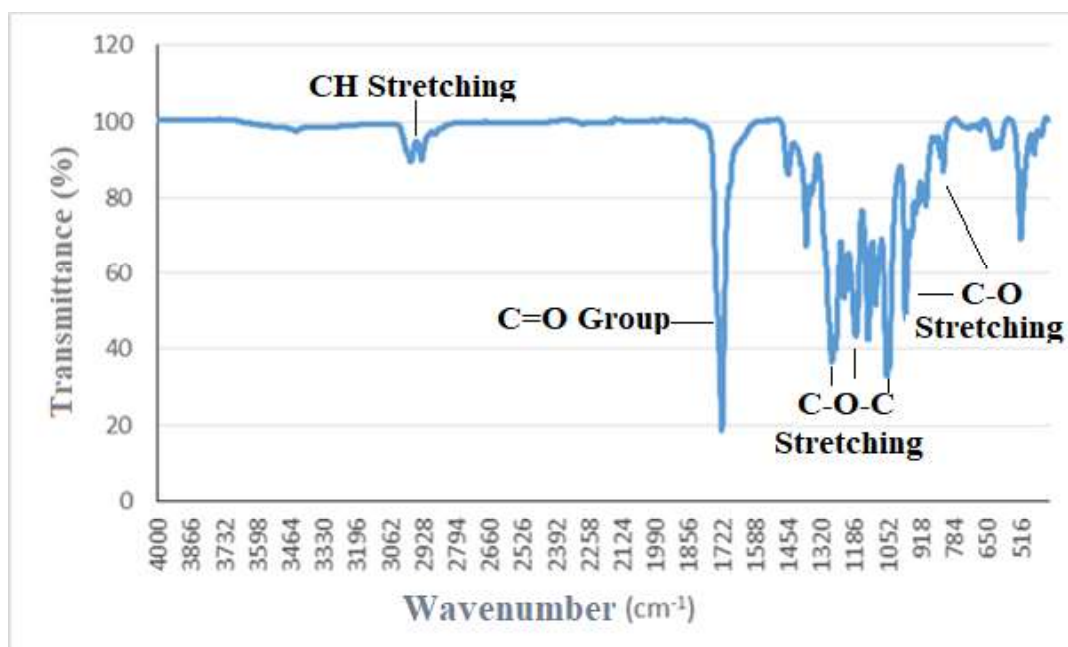


Figure 3.7. Fourier transform infrared spectroscopy curve of PHBV produced by *Cupriavidus necator* bacterial strain.

3.1.4 Results of Differential Scanning Calorimetry Analysis of PHBV

Differential scanning calorimetry (DSC) analysis heat curves of commercially obtained PHBV and produced PHBV is presented in Figure 3.8. DSC curve of commercially obtained PHBV shows triple melting peaks (Figure 3.8a). The first lower peak occurs when thin lamellae of the polymer starts to melt (135-145 °C). The second (145-150 °C) and third (150-165 °C) melting peaks occurs as a result of melting-recrystallization and second melting stages. This double peak points occur when polymer regions with less crystalline structure starts to melt before the regions with high crystalline structure. In this case, second melting temperature (145-150 °C) should be accepted as the melting point of the polymer (B.-J. Wang et al., 2013). Multiple endothermic peaks are attributed to semi-crystalline polymer structure which contain amorph and crystalline parts in the structure (Bianco et al., 2013). The triple melting point peaks are lack in DSC curve of produced PHBV which indicates a more crystalline structure compared to commercially obtained PHBV. The produced PHBV has melting temperature peak at 174.66 °C. In the study of Aramvash et al., PHBV produced by *Cupriavidus necator* with lower hydroxy valerate content (2.98%) also have shown to have similar DSC curve with melting temperature at 173.6°C (Aramvash et al., 2016).

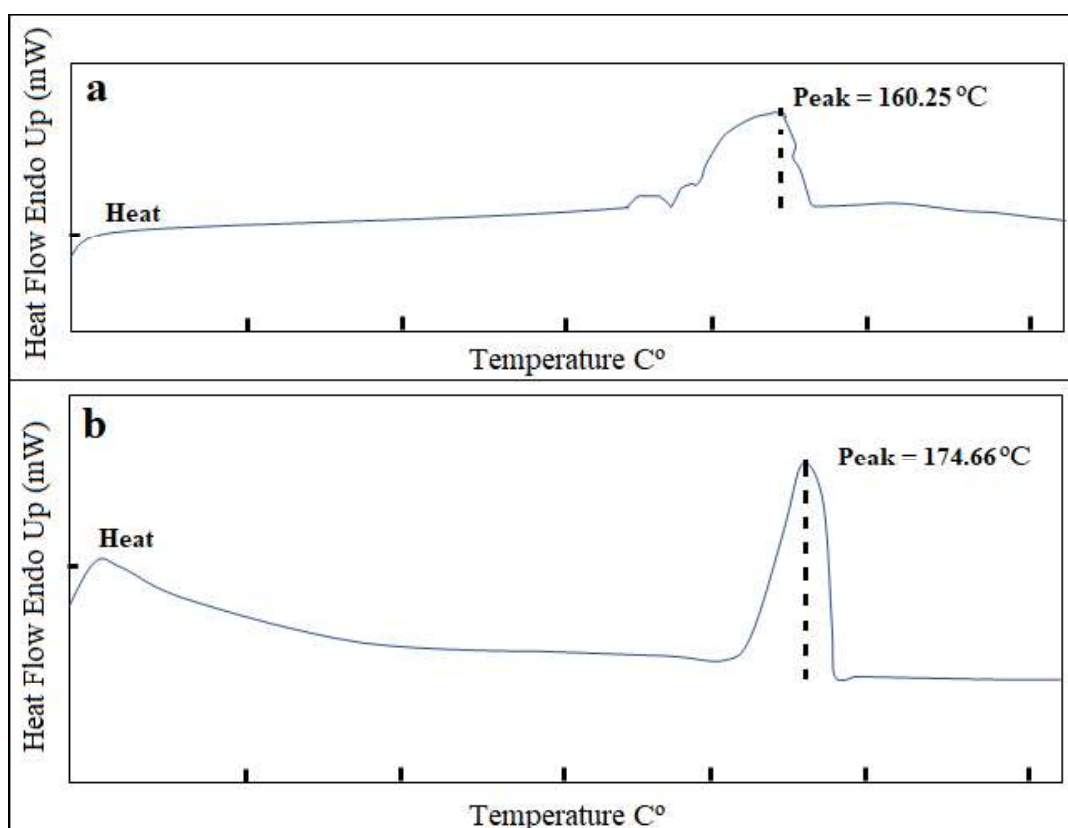


Figure 3.8. Differential Scanning Calorimetry heat curves of commercially obtained PHBV (a) and PHBV produced by *Cupriavidus necator* bacterial strain.

3.2 Results of Purification and Chemical Analysis of Diatom Silica Shells

Diatom silica shells (DS) were obtained in intact and pure form after removal of fractured DS particles. Light microscope was used to examine success of purification. The DS powder was observed under light microscope before and after purification. As shown in the images mostly individual whole DS structures were obtained with purification process (Figure 3.9a and b). The average size of DS was calculated from these images as $18.3 \pm 4.1 \mu\text{m}$. Symmetrical micro-nano structure and pores of DS were investigated by SEM analysis (Figure 3.9c). Energy-dispersive X-ray spectroscopy (EDX) (Figure 3.9d) and X-ray photoelectron spectroscopy (XPS) systems (Table 3.1) analyses were used to determine elemental composition of DS. Analyses showed that highest atomic percentage in DS structure belongs to O and Si

elements (O: 64.54 and 63.2%, Si: 25.46 and 23.1%) since the main structure of DS is formed by silicate. Adventitious carbon is detected by XPS at high percentage which tent to form a film on the samples during analysis comes from an external source. Aluminum (1.9%) and calcium (0.7%) elements were also detected in DS shells at trace amounts. DS particles when obtained from natural sediment areas, contain some impurities depending on the age and environmental conditions. Inorganic oxides can be found in diatomaceous earth are Al_2O_3 , Fe_2O_3 , CaCO_3 , CaO , P_2O_5 , K_2O , Na_2O and MgO . An example of chemical impurities recorded in an obtained raw diatomaceous earth was reported as approximately 1–3% aluminum oxide (Al_2O_3), 0.5–1% ferric oxide (Fe_2O_3), 0.1–0.3% magnesium oxide (MgO), 0.2–0.5% calcium oxide (CaO), 0.07–0.1% potassium (K_2O), with traces of titania (TiO_2) and phosphorous ferric oxide (P_2O_5) (Aw et al., 2011). Al, at high concentrations has reported to interrupt osteoblast mineralization and known as an accumulating toxic metal (M. Song et al., 2017). However, at low concentrations Al have shown to be nontoxic to osteoblasts and shown to has no negative effects on osteoblast proliferation, viability and mineralization were reported (Saldaña et al., 2006).

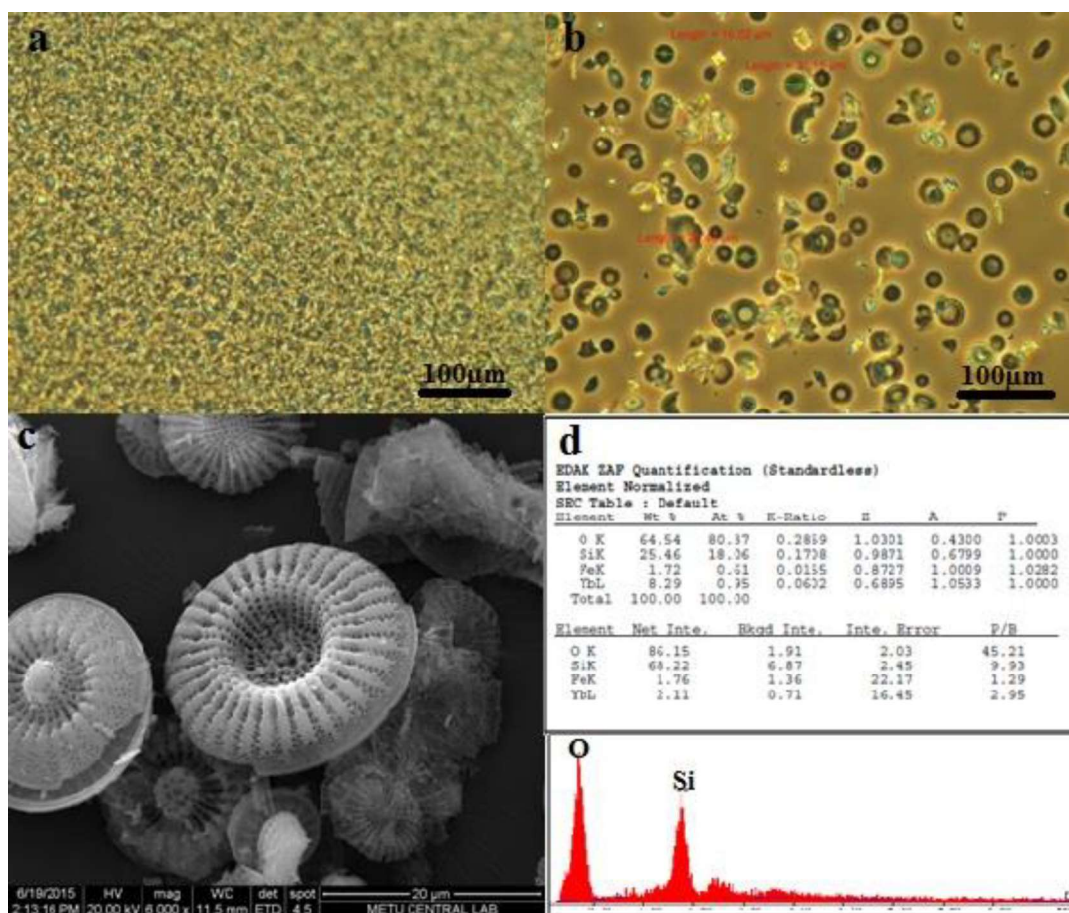


Figure 3.9. Light microscopy images of DS before (a) and after (b) purification. SEM images of micro-nano structure of DS (c). Elemental composition results obtained by EDX analysis of DS (d).

Table 3.1 Elemental compositions of DS determined by X-ray photoelectron spectroscopy

	O	Si	C	Al	Ca
Elemental Composition of DS (Atomic %):	63.2	23.1	11.1	1.9	0.7

3.3 Results of Purification and Chemical Analysis of Diatom Silica Shells

After purification two methods have been applied to obtain smaller, known sized particles from whole DS. The first method is the basic lysis (with NaOH) to downgrade DS sizes. The chemical etching of diatom frustules with 1 N NaOH was previously reported by Umemura et al., (2007) which was used to control pore size of frustules (Umemura et al., 2007). In this study similar approach was used to decrease size of DS to nanometers. SEM analysis revealed that DS were broken up into smaller having the smallest size around 1 micron width (Figure 3.10). However, DS fragments were also stuck together forming larger masses. Therefore, this protocol was not used in later studies since DS fragments were not homogeneously distributed and very few separate DS fragments could be obtained by this method.

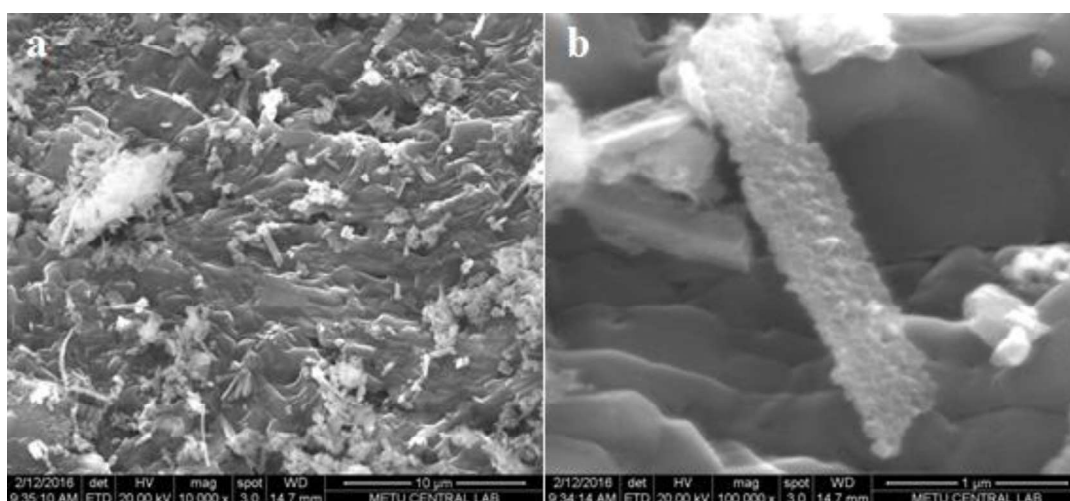


Figure 3.10. Scanning electron microscopy images of DS particles after basic lysis at 10 000X (a) and 100 000X magnifications. Scale bars show 10 μm (a) and 1 μm (b).

In the second method, DS were broken with agate grinder and observed under SEM and light microscopy (Figure 3.11). Light microscopy images showed that as the grinding time increased, the dimensions of DS were further reduced. After short-

term (1 min) milling, DS were largely disintegrated, but some DS with 15-25 microns size were still intact. After medium time (5 min) grinding process, all whole DS were disintegrated and largest shredded DS were around 11 microns. After long period of grinding (10-15 min), the maximum particle size decreased further to around 5 microns as measured from light microscopy images (Figure 3.11c-f). The size distribution of agate ground DS was examined by particle size distribution analysis. When the size distributions of DS after grinding for 1, 5, 10 and 15 minutes were examined, no significant difference between 5, 10 and 15 min grinding was found. The peak of the average size distribution graph of 1 min ground DS was around 10 μm while the peak was shifted to around 8 μm after 15 min of grinding (Figure 3.11g and h). Since there was no significant size difference between grinding groups in terms of average size, ground DS particles were obtained by 15 min of grinding for further experiments considering higher remaining of larger particles in less grinding periods.

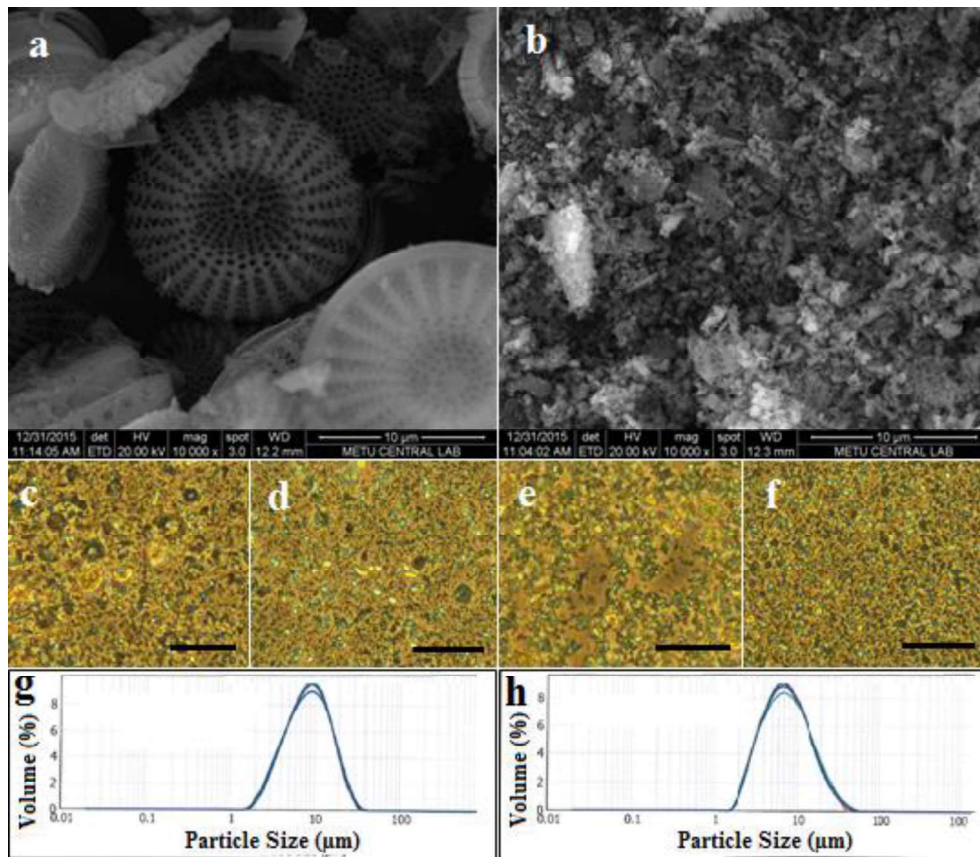


Figure 3.11. Scanning electron microscopy of DS particles as a whole (a) and after grinding for 1 min (b). Images were taken at 10 000X magnification and scale bars show 10 μm length. Light microscopy images of DS after 1 (c), 5 (d), 10 (e) and 15 (f) min of grinding. Images were taken at 10X magnification and scale bars show 30 μm length. Particle size distribution graphs of DS particles after 1 min (g) and 15 min (h) of grinding.

3.4 Evaluation of Effects of DS on Cell Viability

3.4.1 Results of Cell Viability After Direct Contact with DS

In order to investigate the effects of DS on cell viability cells were first exposed directly with DS. Two forms of purified DS was studied at different concentrations; DS in original shape and in ground form. In Figure 3.12, cell viability results after

one and two days of incubation are presented. After the first day of incubation, the cell viability decreased parallel to increasing concentrations of the DS for both ground and not ground forms. However, in ground group, up to 0.125 $\mu\text{g/ml}$ the results were comparable with control cells. The increased DS content could have released more ions that could reach to toxic levels and DS powder at the bottom of the wells could have created contact stress in initial attachment to plate. Thus, overall results suggest that the ground form of DS supported higher cell viability in the first day at low (less than 0.25 $\mu\text{g/ml}$) concentrations. The reason of this could be the smaller size of ground DS particles did not interrupt the initial contact between cells while bigger DS in their original size could interrupt cell to cell interaction in an increasing way with the amount of DS during initial attachment and spreading of cells. In the second day all groups had similar cell viability percentages and two highest DS concentrations 0.5 and 1 $\mu\text{g/ml}$ even enhanced cell viability compared to control (No DS) and other concentration groups. This experiment proved the positive effect of DS on Saos-2 cell proliferation.

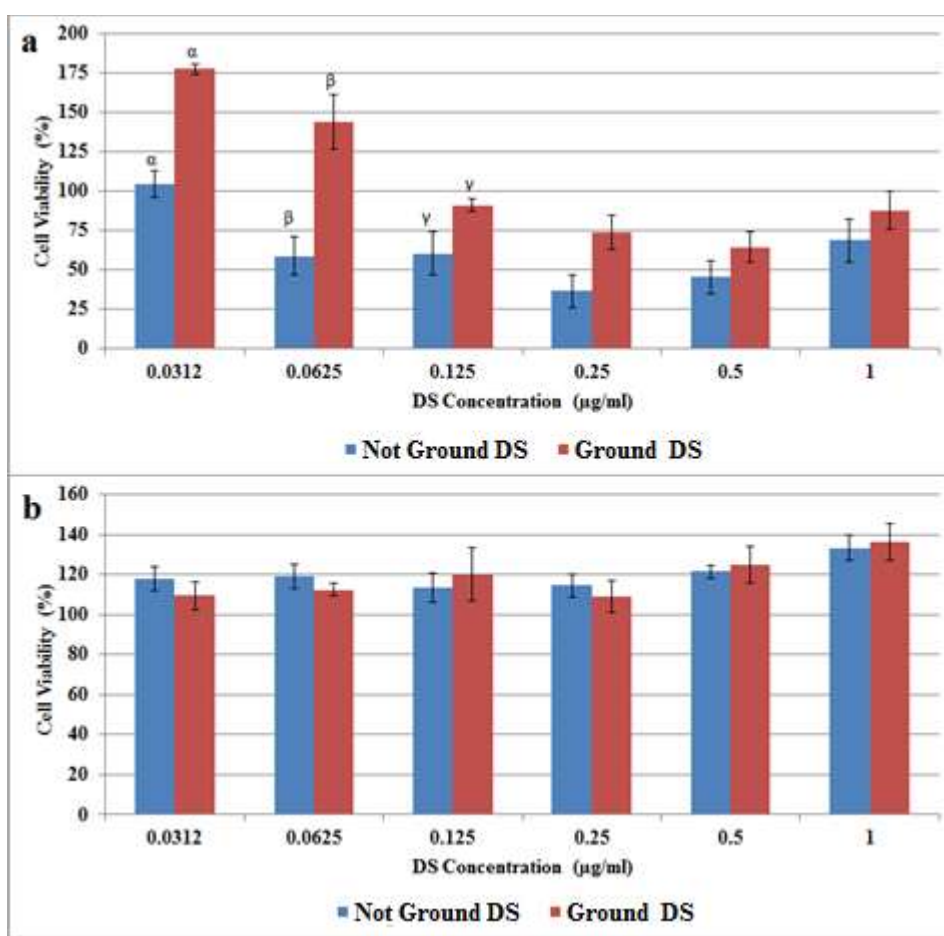


Figure 3.12. MTT assay results of direct cell interaction of different concentrations of ground and not ground DS groups after 1 day (a) and 2 days (b) of incubation. The percent cell viabilities were calculated with respect to control group involving cells without DS direct contact. α , β , γ : The statistically significant differences between ground and not ground groups ($p < 0.01$).

3.4.2 Results of Cell Viability After Direct Contact with DS

As DS was aimed to be introduced as incorporated to polymer fibers in the final form of scaffolds, they were considered to be not directly exposing to cells as investigated with direct contact assay. Therefore, a second study with indirect test was applied for deciding which form (ground-not ground) would be better for scaffold preparation. In this case, cells were grown in media at which DS (at different

concentrations) were incubated for 24 h. The viability results of Saos-2 cells after 1, 3 and 7 days are presented in Figure 3.13. The not ground DS groups showed parallel cell viability with control group from the first day while ground DS showed decrease in cell viability to around 80%. After 3 day of incubation of Saos-2 cells, not ground DS groups showed enhanced cell viability compared to control and ground DS groups. Ground DS groups were still having lower cell viability than control after the 3 days. After 7 days of incubation DS groups showed similar cell viability results and the group with 12.5 mg/ml DS showed improved cell viability. Through the 7 days not ground DS incubated media sustained higher cell viability compared to ground DS; therefore, not ground DS in their original size were chosen to be used in scaffold related experiments. Similarly, in the study of Zhang et al., 2018, larger DS in their original size were reported to be least cytotoxic while smaller DS with irregular shapes were reported to be toxic on osteoblasts and fibroblasts (Xiang Zhang et al., 2018).

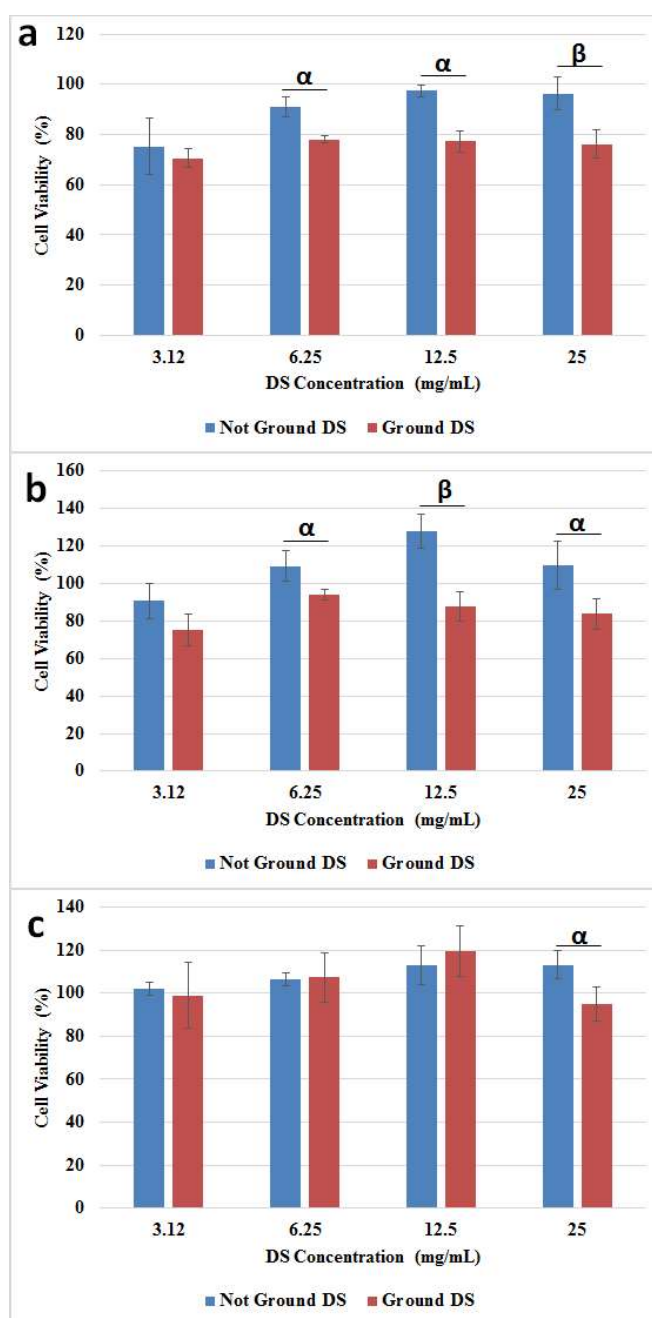


Figure 3.13. MTT assay results of indirect cell interaction of different concentrations of ground and not ground DS groups after 1 (a), 3 (b) and 7 (c) days of incubation. The percent cell viabilities were calculated with respect to control group; cells without DS interaction. α : The statistically significant differences between not ground and ground DS groups ($p < 0.05$). β : The statistically significant differences between not ground and ground DS groups ($p < 0.01$).

3.4.3 Results of Cell Viability on Scaffolds with Different Polymer/DS Concentrations

In order to determine optimum DS concentration to be incorporated into scaffolds in vitro cell culture tests were performed with electrospun PHBV/PCL scaffolds containing different amounts of DS. The group names are presented as the weight ratio of Polymer to DS (Figure 3.14). At both time points, trend of increase in reduction percent of the Alamar blue (thus indicating increase in cell viability) was observed in relation to increase in ratio up to 20/1. After this point further increase in ratio resulted in a decrease in viability. Thus, highest cell viability was achieved with the group having ratio: 20/1 and it was chosen as the optimal polymer/DS ratio for later scaffold studies.

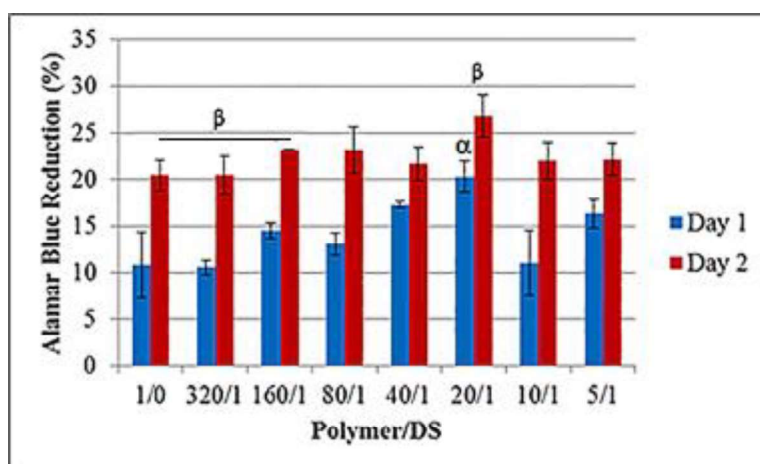


Figure 3.14. Alamar Blue assay results of cell viability study of scaffolds with different polymer/DS ratios. α : The statistically significant difference between 20/1 ratio group and all other groups at day 1. β : The statistically significant difference of 20/1 ratio group from other groups after 2 days of incubation ($p < 0.05$).

3.5 Production and Morphological Characterization of Scaffold Groups

A wet co-electrospinning system was developed in order to form a scaffold from homogeneous collection of fibers with two different compositions; PHBV/PCL

fibers loaded with an antibiotic, cefuroxime, CA and PUL fibers incorporated with DS. Prior to production of this multi-component, dual fiber scaffold group (PHBV/PCL/CA:PUL/DS), the production of individual fiber phases, PHBV/PCL and PUL/DS were optimized by single phase wet electrospinning studies.

3.5.1 Optimization of Production of the PHBV/PCL Fiber Phase

During the optimization of PHBV electrospinning procedure initial experiments were conducted with PHBV polymer solution prepared with chloroform as volatile organic solvent. For production of PHBV fibers both conventional (dry) and wet electrospinning methods were tried. The micro structure and fiber morphology of resulted forms were examined by SEM. PHBV fibers that were collected on alumina collector formed a thin scaffold structure by spreading to a large area. On the other hand, fibers collected by wet electrospinning, formed a 3 dimensional structure in ethanol pool (Figure 3.15a and b). Initial trials were conducted with several increasing concentrations of PHBV (5, 8, 10 12 and 14%) was studied and proper jet formation was achieved at 14% PHBV concentration. However, bead formation in the fibers could not be removed despite changing parameters such as flow rate, distance to collector screen and applied voltage. Various solvents were tried to find the suitable solvent to obtain smooth PHBV fibers. Electrospinning with double solvent systems such as chloroform/acetic acid (1/1) and chloroform/HFIP (1/1) did not yield fibers with desired structure (Figure 3.15c and d). The pilling of the fibers could not be removed when the solvents were chloroform and chloroform/acetic acid (1/1). The bead formation on fibers tend to occur when there is not enough charge density on polymer jet which fails the complete stretching of fibers (Lin et al., 2004). Low viscosity and high surface tension of a solution can also initiate bead formation on fibers (Fong et al., 1999; Zuo et al., 2005). Bead formation on fibers created an irregular scaffold structure that will vary physical responses of the scaffold in terms of structural stability, degradation and mechanical force (Figure 3.15c). The beads on the fibers have caused scaffold structure to collapse which decreased 3D thickness

and porosity. The uncontrolled distribution of beads on the fibers would create scaffolds with different structural properties at each production which will decrease reproducibility (Lin et al., 2004). Beads had thicker polymer content compared to fibers which would cause early degradation of fibers in the structure and remaining beads would fail to support tension without fibers in between. The uneven polymer distribution through the fibers would cause mechanical failure of thinner parts. Because of these reasons, fibers have needed to be optimized to be bead free. The use of solvent composition; chloroform/HFIP (1/1) created structures that looked like fibers coiled on each other around an imaginary axis to form thick rows of fibers (Figure 3.15d), standing separately from each other. Thus, there were large pores-spaces between fibers. The coiled fibers were thicker (Figure 3.15d) and have created a brittle 3D structure that was vulnerable to mechanical failure. Therefore, these scaffold microstructures were far from the desired fibrous structure and further optimization studies have conducted.

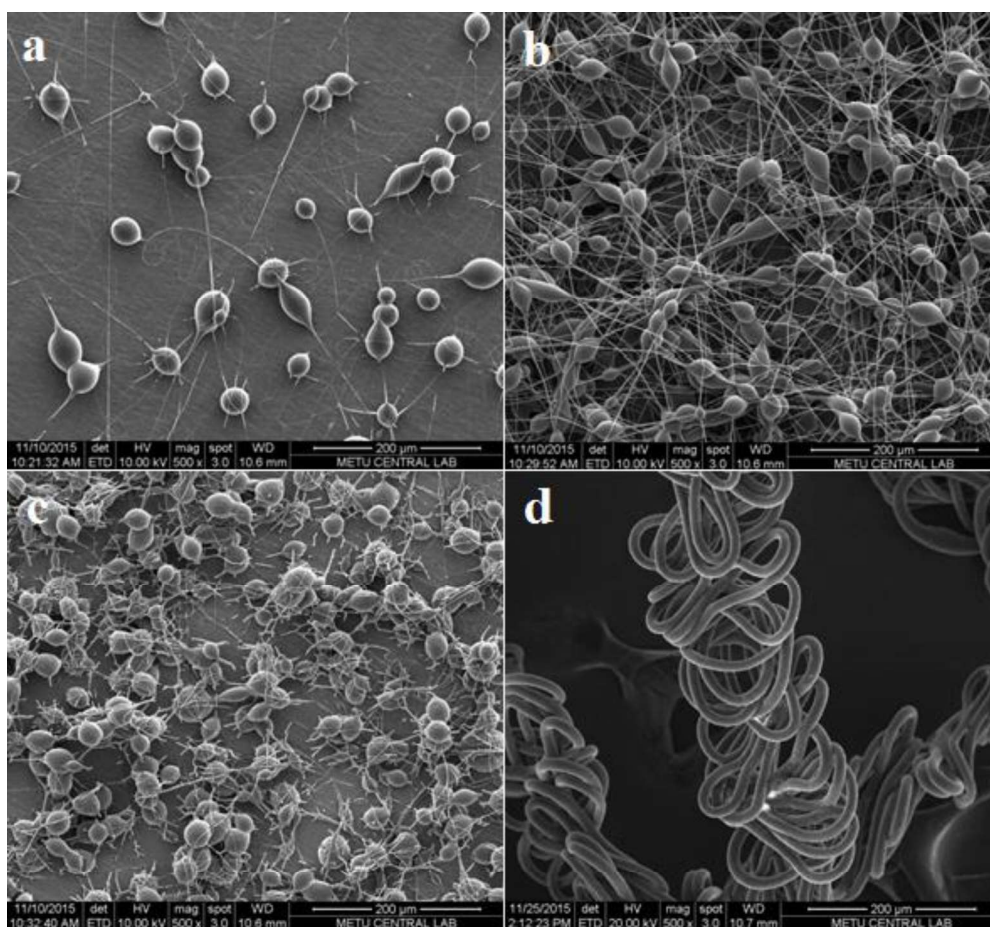


Figure 3.15. SEM images of PHBV fibers produced by dry (a) and wet (b) electrospinning methods using chloroform as the solvent. SEM images of PHBV fibers produced by dry electrospinning using chloroform/acetic acid (1/1) (c) and chloroform/HFIP (1/1) (d) as the polymer solvents. Images were taken at 500X magnification and scale bars show 200 μm length.

Electrospinning with chloroform as polymer solution did not produced smooth fiber structure, so experiments were carried out using HFIP as the solvent. These trials resulted in desired bead-free smooth fiber structure but fractures on the PHBV fibers were observed on the SEM images (Figure 3.16).

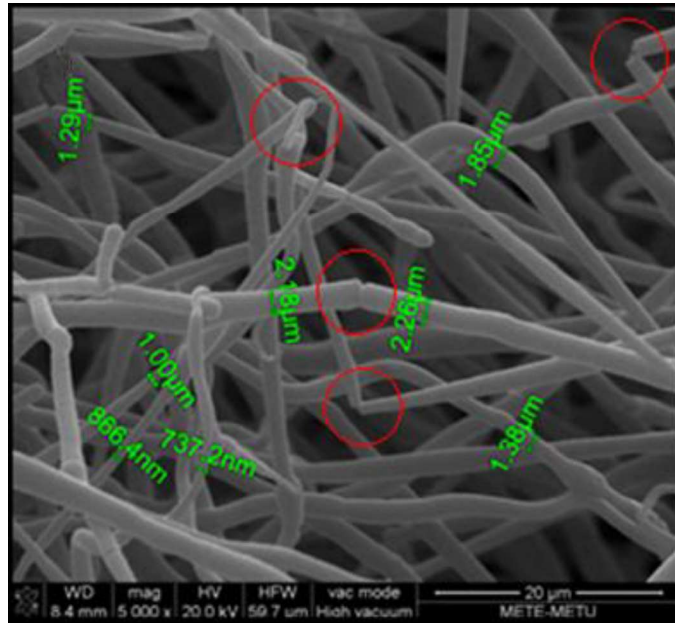


Figure 3.16. SEM images of PHBV fibers produced by wet electrospinning using HFIP as the polymer solvent. Red circles indicate fractures on fiber structure. Image was taken at 5000X magnification and scale bars show 20 μm length.

The main solution parameter that has reported to be effective on fiber morphology is viscosity. In order to support smooth fiber formation viscosity of the solution should be high enough to create necessary viscoelastic forces (Fong et al., 1999). As electrospinning system operates, fiber jet forms at the tip of the syringe and whipping of the fibers starts under the effect of charge. Oppositely, the surface tension of the polymer solution creates opposite forces to fiber formation which tend to form spheres (bead formation) instead of smooth fibers as Rayleigh instability favors. Viscoelastic forces at certain level should withstand against Rayleigh instability and prevent deformation of fiber morphology. If the solution concentration/viscosity is low, viscoelastic forces will not be enough to support continues fiber formation in the process of axial stretching during whipping of polymer solution (Gupta et al., 2005; Nezarati et al., 2013; Jing Tao & Shivkumar, 2007). Another reason of fiber breakage has reported to be high charge density on jet that depends on applied voltage and relative humidity. The applied voltage creates a charge density on solvent jet, while some of the charge discharges to water molecules in the atmosphere

created with humidity (Kalayci et al., 2005). This discharge balances the charge density on the jet. Study of Nezarati et al., have reported that if the relative humidity is low (<50% RH), breakages tend to form on electrospun PEG and PCL fibers. In the study, smooth PCL fibers have shown to form under 10 kV voltage with 50% RH but breakages have formed when voltage was increased to 16 kV even the relative humidity was kept same. The results showed the effect of charge density on the fiber morphology (Nezarati et al., 2013). In this thesis, the commercial PHBV used was in the pellet form and prepared PHBV solution was formed a suspension rather than complete dissolution in the HFIP. The high concentration does not always result in high viscosity since the solubility of the polymer will determine the effect of concentration on viscosity. That is why the viscosity of PHBV suspension solution was low which can explain the formation of breakage on the fibers. Therefore, it was decided to increase viscosity of polymer solution and modify morphology of PHBV fibers by adding a second polymer to prevent possible negative effects of the fractured fibers. PHBV fiber with some broken fibers in micro-structure was not recognizable in 3D macro structure of the scaffold. However, such micro defects are known to change mechanical and degradation like properties as well as batch to batch variation in structure. For this reason, first polyvinyl alcohol (PVA) was selected to combine with PHBV since it is known to contribute to fiber formation. PVA, used in polymer blends to overcome charge repulsive forces, increase chain flexibility and ease the electrospinning of polymers (Bonino et al., 2011). Three different PHBV:PVA ratios were used in trials as; 9:1, 8:2 and 7:3 w/w (Figure 3.17a-c). After wet electrospinning, fiber morphologies were examined by SEM. As shown in Figure 3.17a-c, PVA blending was not successful to prevent fracture formation. Secondly, PCL was selected for blending trials and blends with PHBV was prepared at ratios; 9:1, 8:2 and 7:3 w/w (Figure 3.17d-f). PCL was soluble in HFIP and increased the viscosity of the blend solution. PCL has reported to have lower elastic modulus and electrospun PCL/PHBV blend fibers have reported to have decreased elastic modulus compared to pure PHBV fibers. The decreased elastic modulus means ability to elongate more under mechanical force before break which decreases

brittleness of the structure (Del Gaudio et al., 2011). PCL is also a preferred polymer in bone tissue scaffold studies with proven compatibility with bone cells (H. H. Song et al., 2007). SEM images of different blends of PHBV:PCL scaffolds is shown in Figure 3.17. When PHBV was mixed with PCL at a ratio of 7:3 w/w, the fracture formation of the fibers was prevented (Figure 3.17f). The solution viscosity increased by blending with PCL and improved viscoelastic forces prevent the defect formation while electrospinning. Also blending of PCL into the structure have increased elongation at break which decreased brittleness, preventing breakage of fibers. The 7:3 w/w ratio was seen as the most suitable polymer composition for PHBV:PCL fiber formation.

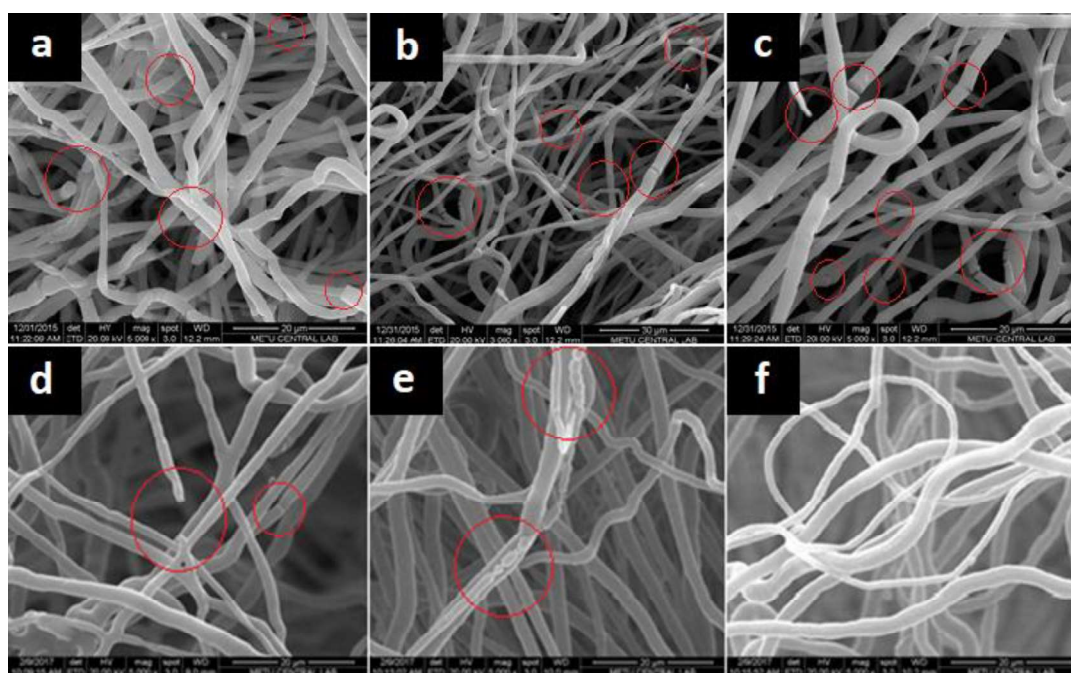


Figure 3.17. SEM images of fiber morphology of electrospun PHBV/PVA and PHBV/PCL scaffolds prepared by different blend ratios; The PHBV:PVA ratio is 9:1 (a), 8:2 (b) and 7:3 (c). The PHBV:PCL ratio is 9:1 (d), 8:2 (e) and 7:3 (f). Red circles indicate breakages on fiber structures. Image was taken at 5000X magnification and scale bars show 20 μ m length.

3.5.2 Optimization of Production of the PUL/DS Fiber Phase

In order to see the possibility of electrospinning of DS skeletons in polymer solution, DS were mixed with PUL in water and electrospinning trials were performed. In the optimization experiments, different PUL/DS wt/wt ratios (20/1, 10/1, 5/1 and 4/1 wt/wt) were tested (Figure 3.18). Homogeneous fiber structure in these trials were achieved at DS ratio up to PUL/DS 5/1 w/w (Figure 3.18c). When DS content in the PUL solution was increased up to 4/1 wt/wt PUL/DS ratio, DS in the solution has blocked the solution flow through the electrospinning needle and disrupted electrospinning process. As a result, fiber formation failed and collected structure consisted of incomplete fibers with lots of bead formation (Figure 3.18d). The SEM image of PUL/DS 5/1 w/w scaffold showed that structure was very crowded with DS which created unbalanced distribution through the structure (Figure 3.18c). PUL/DS group with 10/1 wt/wt ratio had balanced distribution of DS among fibers and smooth fiber structures (Figure 3.18b). For these reasons, group with PUL/DS 10/1 wt/wt ratio was selected to build dual fiber scaffolds. The PUL/DS solution containing highest DS (15-25 μm) were successfully electrospun together with PUL and were found as retained in PUL/DS fibers as initially aimed. For the first time in the literature, DS was electrospun within a polymer solution to form DS incorporated fibers.

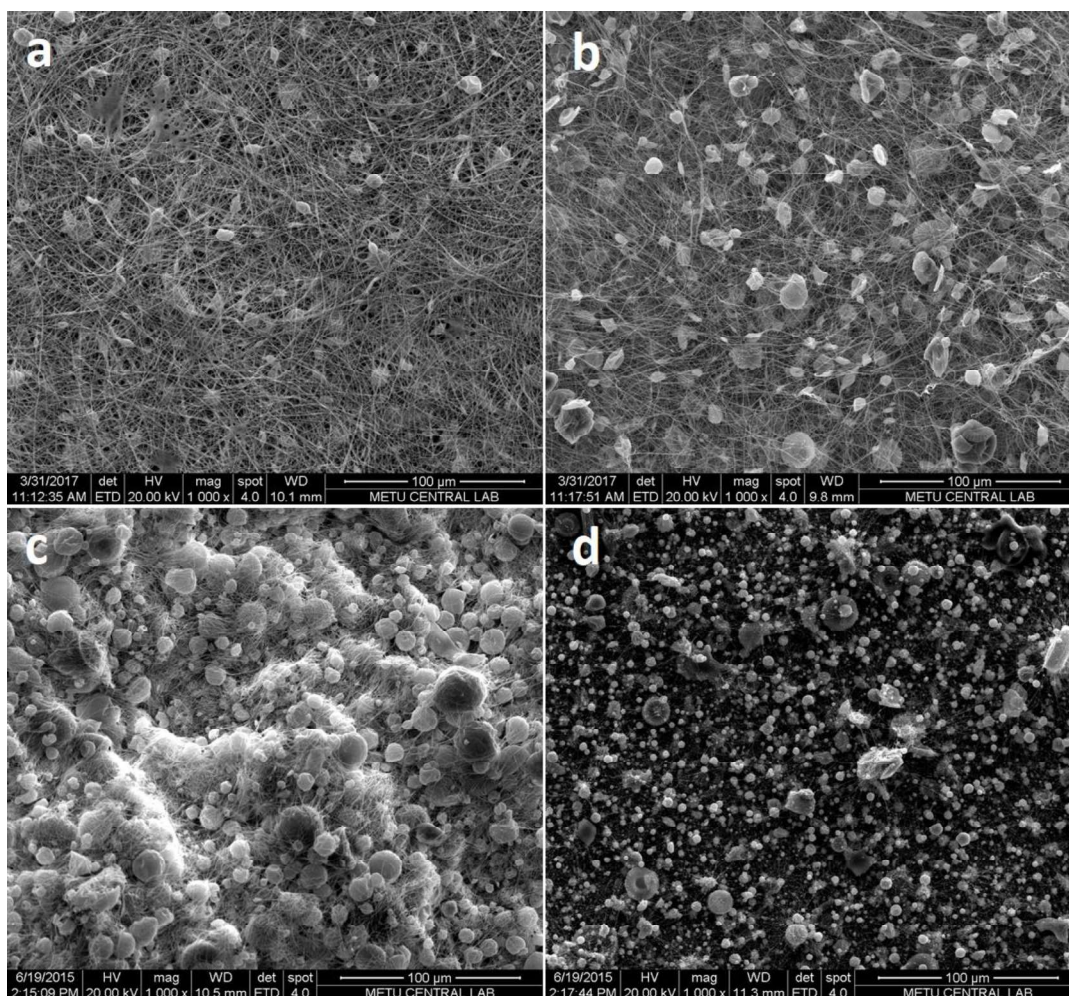


Figure 3.18. SEM images of electrospun PUL/DS scaffolds prepared by PUL/DS blend at 20/1 (a), 10/1 (b), 5/1 (c) and 4/1 (d) wt/wt ratios. Images were taken at 1000X magnification while scale bars show 100 µm length.

PUL is a hydrophilic polysaccharide that quickly dissolves in aqueous environments. Electrospun PUL fibers can easily dissolve when interacted with media and in order to prevent dissolving of PUL fibers, it should be cross-linked. Several cross-linking methods were applied to optimize PUL crosslinking in the fiber form. In the first studies, STMP was used as cross-linking agent for PUL (Lack et al., 2004). PUL/STMP weight ratio was adjusted to be 7/3 and STMP/NaOH weight ratio was set as 10/1 for cross-linking attempt. Firstly, STMP was dissolved in PUL solution and electrospun to form PUL fibers and then the fibers were cross-linked by

incubating in alkali aqueous medium containing NaOH for 10-12 min to initiate cross-linking reaction. In order to prove the successful cross-linking of PUL fibers, fibrous mat was incubated in PBS but PUL fibers dissolved, thus, cross-linking was not achieved. The second attempt was to make in situ cross-linking of PUL fibers. With this method, it is aimed to initiate the cross-linking reaction of the fibers during electrospinning so that the fibers are cross-linked until the moment they reach the collector bath under electric current. To this end, the mixture was mixed with NaOH solution just before electrospinning. However, since the cross-linking process began at the time NaOH was added, the PUL polymer solution rapidly turned into gel which prevented the formation of fiber. Therefore, electrospinning was repeated by mixing with NaOH for each 0.5 mL volume. The syringe assembly was renewed every 0.5 mL volume and the electrospinning was completed discontinuously. As a result of the in situ cross-linking process, the fiber structure was found to be much more durable than the fibers produced by the previous system. However, during the 1 day PBS incubation, it was observed that it was dispersed again and the structure was not preserved for the intended times. Then, another cross-linking agent, glutaraldehyde (GTA) was introduced to the method. By adding GTA as a cross-linking agent, aim was to increase the cross-linking efficiency by binding $-OH$ and $-NH_3$ groups. In the first trials, the double crosslinking method was tried by using STMP and GTA consecutively. Then, cross-linking studies with GTA alone were continued and the most successful result was obtained. All cross-linking trials are summarized step by step in Table 3.2. Groups were initially subjected to either in situ GTA or STMP cross-linking and followed by additional steps stated with “+” sign in the table. In the groups 4 and 5, GTA was added to polymer solution and solution was incubated at 60 °C which was expected to initiate/speedup crosslinking. Effect of drying on GTA crosslinking was investigated by drying at RT or Lyophilized to obtain final form. A second GTA crosslinking step was included for some groups, indicated as GTA in the table. After this second GTA treatment scaffolds were dried either at RT or by Lyophilization. The integrity of the scaffolds was investigated in PBS and success of crosslinking was evaluated.

Table 3.2 Optimization trials for crosslinking PUL. RT: Drying at RT, L: Lyophilization, 60 °C: High temperature was applied to polymer solution with GTA for 1 h, GTA: GTA crosslinking. PBS: Degradation experiment. Table was first divided into two parts according to in situ cross-linking method; GTA (groups 1-9) or STMP (groups 10-15) and additional operations are marked in the order. The success of crosslinking was presented as stability in PBS.

Experimental Groups		Steps of Cross-linking Method						Results
		60°C	RT	L	GTA	RT	L	PBS
<i>in situ</i> GTA	1							Degraded
	2		+					Stable
	3			+				Stable
	4	+	+					Stable
	5	+		+				Stable
	6		+		+	+		Stable
	7		+		+		+	Stable
	8			+	+	+		Stable
	9			+	+		+	Stable
<i>in situ</i> STMP	10							Degraded
	11		+					Degraded
	12			+				Degraded
	13				+	+		Degraded
	14				+		+	Stable
	15			+	+		+	Degraded

In addition, trials were also conducted by adding 1/10 additional solvent DMF to the electrospinning solutions in order to facilitate the electrospinning process since DMF is a polyelectrolyte with high dielectric constant (Lee et al., 2003). All experimental groups (1-15 in Table 3.2) were repeated by addition of DMF and the degradation tests were performed in PBS. Among the experimental groups, group 1 treated with in situ GTA has degraded in PBS and required additional processing. The other in situ GTA groups (2-9) were stable in PBS. Among the groups treated with in situ STMP, only group 14 were not disintegrated. All other in situ STMP groups were observed to be dispersed in PBS. Analysis was performed by SEM to see the morphology of all groups (2-9 and 14) that could maintain their integrity after PBS incubation (Figure 3.19). According to the result of SEM analysis, it was observed that the fibrous structures were fused together and disrupted. The porous structures of the samples (group 2) which were dried after electrospinning at room temperature decreased with the addition of DMF as solvent. On the other hand, it was observed that the samples (group 3) which were dried by lyophilization after electrospinning and were produced with the addition of DMF had rough surface. Groups 4 and 5, which were incubated in 60 °C without any drying did not have porous or rough structure. On the other side, relatively more porous structure was obtained when DMF was included in polymer solvent for electrospinning. The positive effect of lyophilization was observed in groups 6, 7, 8 and 9. The lyophilized samples electrospun with DMF addition and subjected to double crosslinking had decreased porosity (groups 5, 9 and 14). The reason of this could be the remaining trace amount of DMF that does not freeze at very low temperatures (-80 °C). As a result, the presence of DMF during the lyophilization process dissolved the polymer and disrupted the porous structure. After this conclusion, the use of DMF was not used for further experiments.

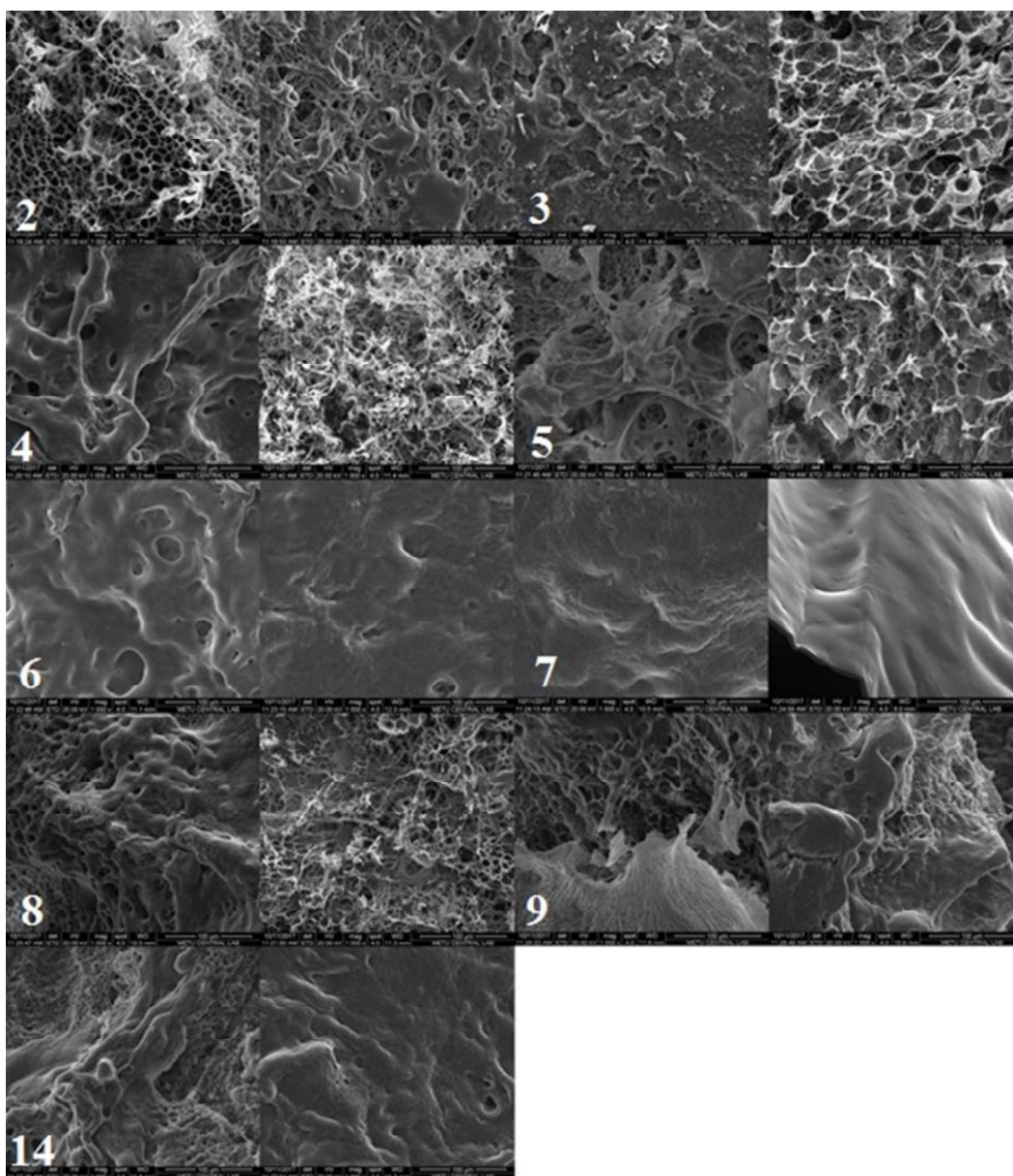


Figure 3.19. SEM images of intact groups (2-9 and 14) with PUL cross-linking, after PBS incubation. The image to the right of each numbered image is the version of the same experimental group produced using DMF as solvent. (All scale bars: 100 μm).

At the end of the experiments, the most successful method was obtained after one-time in situ crosslinking with GTA and this method was used during co-electrospinning experiments. The successfully selected group is shown in Table 3.2 as the third group. In situ crosslinking was adapted from a study in literature. The

study of Chen et al., have proposed GTA for crosslinking of a pullulan film in order to improve its physical properties. In addition, p-toluene sulfonic acid (0.1%), an acidic catalyst, was added to increase the efficiency of the cross-linking process (Chen et al., 2017). GTA crosslinks PUL molecules by forming acetal bridges (C-O-C), formed as a result of reaction between hydroxyl groups of pullulan and aldehyde groups (-CHO) (Figure 3.20). The pH of the solution influences GTA confirmation which would determine speed and fate of the crosslinking reaction. At acidic pH, GTA molecule forms hemiacetal rings with two aldehyde groups and at basic pH GTA polymerize into α,β -unsaturated glutaraldehyde polymer (Barbosa et al., 2014; Hermanson, 2013). In this study p-toluene sulfonic acid (0.1%) was used to obtain acidic pH to form hemiacetal rings of GTA with two aldehyde groups which has reacted with hydroxyl groups of PUL to form acetal bridges.

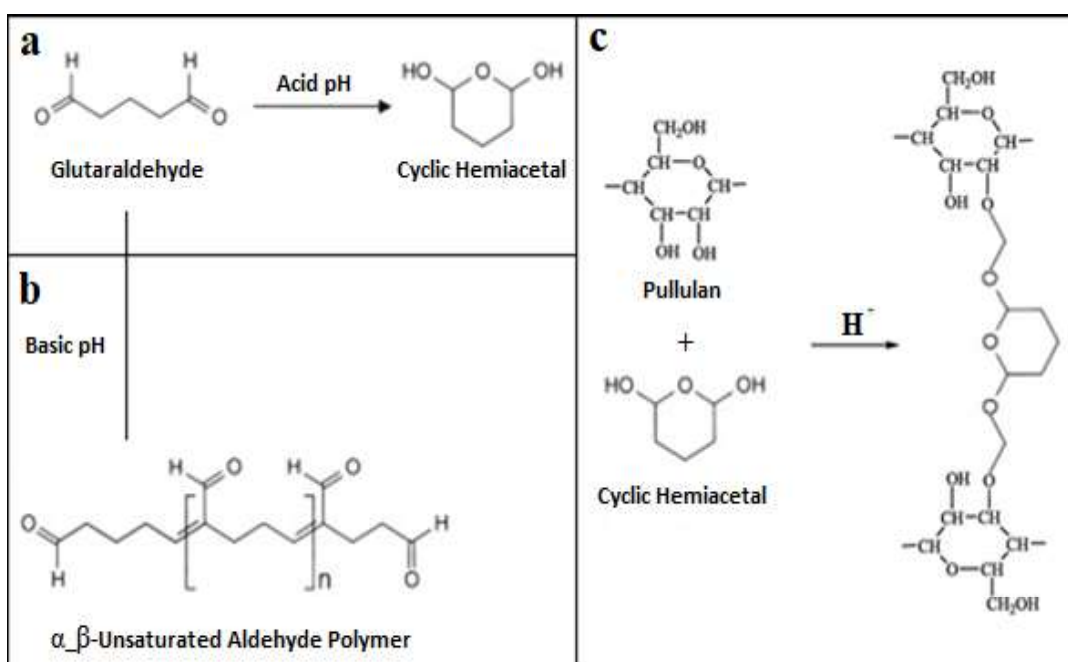


Figure 3.20. Cyclic hemiacetal formation by GTA in acidic pH (a) α,β -unsaturated glutaraldehyde polymer formation by GTA in basic pH (b). Crosslinking of PUL by acetal bridge formation with GTA hemiacetal ring (c). Shema was modified from studies of Hermanson and Li et al., (Hermanson, 2013; Y. Li et al., 2018).

Electrospinning was performed immediately after stirring the polymer solution at 60 °C for 1 h. In the first trials of electrospinning, GTA and p-toluene sulfonic acid in the resulting fibers were dispersing into ethanol bath collector and in further experiments GTA and p-toluene sulfonic acid were added to the collecting bath at the same concentration with polymer solution in order to prevent a decrease in concentration. The fibers collected in ethanol were dried by lyophilization. The drying process took about 1 day, during which time the crosslinking reactions of the fibers were completed. The resulting scaffolds were able to maintain their integrity in PBS.

3.5.3 Properties of Co-electrospun Scaffold

In preliminary studies the ability to produce PHBV fibrous scaffold was investigated. High polymer concentration resulted in brittle fibers which have broken in the process of production. Continuous fiber morphology was achieved by electrospinning when PHBV/PCL ratio was used at 7/3 wt/wt and this ratio was set to be used through the study. Co-electrospun scaffolds which were prepared by simultaneous electrospinning of two different polymer solutions contained two types of fibers with opposite characteristics: hydrophobic and hydrophilic phases together. This dual characteristic of co-electrospun scaffold was aimed to enhance cell adhesion. Bauer et al, was reported enhanced cell adhesion by introduction of hydrophilicity to super-hydrophobic surfaces (Bauer et al., 2008). Another study have reported enhanced cell attachment and spreading by co-electrospinning of PCL with PVA in order to improve hydrophilicity (C. H. Kim et al., 2006).

Hydrophobic PHBV/PCL fibers were also suitable for loading and controlled release of a hydrophobic antibiotic CA that would be beneficial for anti-inflammatory purposes in ultimate use of such scaffolds and, hydrophilic PUL fibers were suitable (as shown in previous optimization studies) to incorporate DS particles that will enhance mechanical properties while providing Si for bone regeneration.

PHBV/PCL and PHBV/PCL/DS scaffolds were produced by conventional wet electrospinning to investigate the effect of DS doping and to compare scaffolds of single-phase wet electrospinning with multiphase wet co-electrospinning. After wet electrospinning fiber scaffolds were collected in a bath and needed to be dried to obtain final form. However, if scaffolds are dried in RT, as the liquid evaporates, fibrous mat collapses and losses thickness. In order to preserve 3D structure of scaffolds freeze-drying method was used. When frozen, water in pores freeze with fibers in their 3D orientation and lyophilization makes water sublimate under negative pressure. As the water in the pores evaporate directly from frozen phase, fibers stay in their 3D formation and interconnected pores can be preserved (Yokoyama et al., 2009). Co-electrospun scaffold was formed with relatively more compact fiber distribution owing to collecting fibers from two polymer solutions which is doubling the rate of fiber formation at the same spot. GTA crosslinking of PUL was modified from literature, and optimized to be used in electrospinning and crosslink PUL in fiber form (Chen et al., 2017). The DS were observed to be covered and stabilized in PUL fibers after crosslinking with GTA (Figure 3.21).

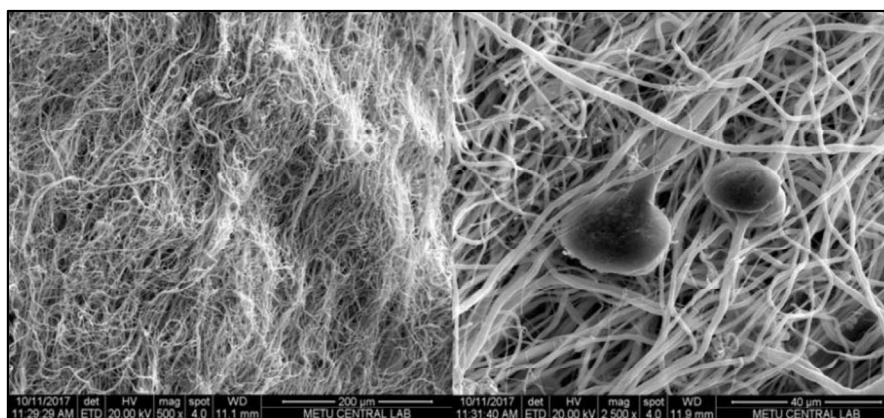


Figure 3.21. SEM images of co-electropun PHBV/PCL/CA:PUL/DS scaffold at different magnification. Images were taken at 500X (Left) and 2500X (Right) magnifications while scale bars show 200 (Left) and 40 μm (Right) lengths.

3.6 Comparison of Pore Size Distribution and Porosity of Scaffold Groups

Porosities and pore size distributions of the scaffold groups are presented in Figure 3.22. Electrospun PHBV/PCL scaffold showed the highest porosity (75.85%) compared to electrospun PHBV/PCL/DS (58.47%) and co-electrospun PHBV/PCL/CA:PUL/DS (42.17%) scaffolds. DS loading had a major decreasing effect on porosity of the scaffolds. The DS particles cover more space between fibers and fibers incorporating DS became heavier; and thus, resulted in more compact structure. Co-electrospun scaffold has more dense fiber mesh since two different fibers were deposited on each other resulting in a lower porosity value. Scaffold groups showed relatively homogeneous pore size distribution with small deviations. The pore size of PHBV/PCL scaffold was around 10 μm while PHBV/PCL/DS and PHBV/PCL/CA:PUL/DS scaffolds had higher number of pores between 40-50 μm pore size (Figure 3.22). In the B-PHBV/PCL/CA:PUL/DS scaffold produced by synthesized PHBV with co-electrospinning method, porosity increased to 54.71% compared to PHBV/PCL/CA:PUL/DS (42.17%) scaffold. The reason of the increase can be explained with thicker B-PHBV/PCL fibers produced using synthesized PHBV that can support the 3D structure, preventing the scaffold from collapsing. The pores in B-PHBV/PCL/CA:PUL/DS scaffold which were less than 20 μm in size were much less in amount compared to other groups. The thick structure of B-PHBV/PCL fibers produced using synthesized PHBV was increased pore size in the scaffold. As a result, scaffold became conducive to cell migration and spread as fibrous mat contains densely wider pores that support cell migration. Previously, osteoblast cells have been reported to proliferate at 40 μm diameter pore size and migrate into the scaffold at 100 μm diameter pore size (Loh & Choong, 2013).

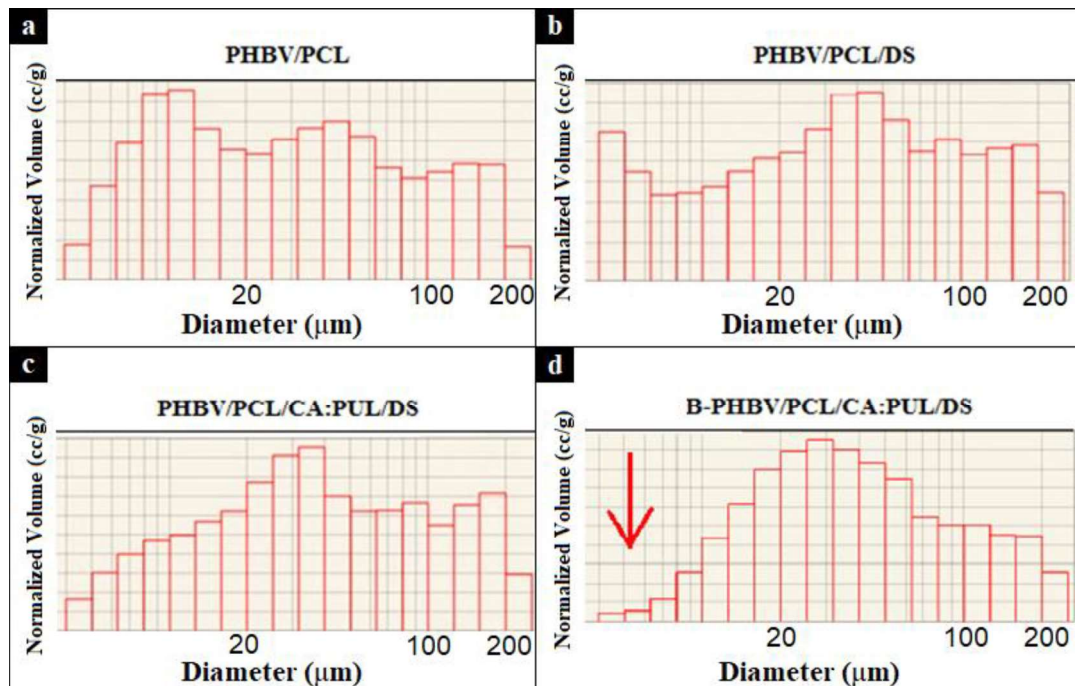


Figure 3.22. Pore size distributions of the scaffold groups; PHBV/PCL (a), PHBV/PCL/DS (b), PHBV/PCL/CA:PUL/DS (c) and B-PHBV/PCL/CA:PUL/DS (d). Red arrow indicates the decrease in amount of smaller pore size in B-PHBV/PCL/CA:PUL/DS scaffold compared to other groups.

All groups possessed large number of pores between 40 to 200 μm pore sizes. It was reported that presence of pores with size distribution between 100 and 400 μm enhances new bone tissue and capillary formation while improving cells metabolism by enabling nutrient and oxygen transfer (Bose et al., 2012; Yoshimoto et al., 2003). Additionally, the organic matrix deposited prior to maturation of bone tissue has a pore size distribution between 75 to 100 μm (Muzzarelli, 2011).

3.7 Weight Loss, Water Retention and Enzymatic degradation Results of Scaffold Groups

Cumulative weight losses of scaffold groups were compared to evaluate the swelling and degradation properties of the scaffolds as this will affect their success when used for BTE purpose. As presented in Figure 3.23a there was no significant difference

between cumulative weight losses of groups through 21 days of incubation period; all groups had a final cumulative weight loss around 3%. The cumulative weight loss of PHBV/PCL and PHBV/PCL/CA:PUL/DS groups showed nearly no change after an initial loss about 3.5 % and 2.8%, respectively. PHBV is a hydrophobic polymer which was reported to have very slow degradation rate in in vitro physiological conditions (Nargis Sultana et al., 2012). After crosslinking of PUL, better integration of DS into PUL fibers was observed. This might have prevented such loss of DS (Figure 3.23a). Thus, PHBV/PCL/CA:PUL/DS group conserved its weight through 21 days of incubation which also proves the successful crosslinking of PUL fibers. In previous studies stable PUL fibers were reported to be obtained by blending PUL within a second polymer (Atila et al., 2016; Shi et al., 2011; Xiao & Lim, 2018) and as far as our knowledge there is no study reporting crosslinking of PUL fibers through electrospinning. In this study a successful method for GTA crosslinking of PUL without blending with another polymer phase, during electrospinning is reported. B-PHBV/PCL/CA:PUL/DS group lost more mass than the other groups after the 7th day of the weight loss experiment. When we compare the B-PHBV/PCL/CA:PUL/DS group with PHBV/PCL/CA:PUL/DS group, they both contain hydrophilic PUL fibers while the mass loss of B-PHBV/PCL/CA:PUL/DS group was higher. This result is thought to be related to the fact that the B-PHBV/PCL/CA:PUL/DS scaffold contains more amount of larger pores compared to other scaffolds that increase the weight loss rate by allowing more water to enter fibrous structure. Similar results were also observed in the water retention experiment.

Percent water retention values of scaffolds are presented in Figure 3.23b and results showed a parallel pattern with groups' porosity values. B-PHBV/PCL/CA:PUL/DS group was found to be the most water-retaining group. The higher number of large pores in the structure allowed the water to be transported more easily to the interiors with hydrophilic PUL fibers, thereby allowing the scaffold to draw more water. PHBV/PCL group has the highest porosity degree (75.85%) among groups and

percent water retention rate up to 15 days of incubation was highest in this group. Compared to this group, water retention for same time period was less in PHBV/PCL/DS group which also had less porosity value (58.47%). Lowest water retention percentage was observed with PHBV/PCL/CA:PUL/DS group. The main reason for this outcome might be the low porosity degree compared to other groups. The water retention of this group, despite its low porosity would be expected to be higher due to the presence of hydrophilic PUL fibers. Contrary to the expectations; successful crosslinking of PUL and formation of denser fibrous network with dual fibers prevented absorption of high amounts of water. The water retention of scaffolds should be in controllable levels since high amount of water retention means swelling of the scaffold which creates the risk of dislocation of an implanted scaffold in tissue engineering studies (Nazemi et al., 2014). PHBV/PCL/CA:PUL/DS group showed very stable swelling behavior through 21 days of water retention experiment compared to single fiber groups.

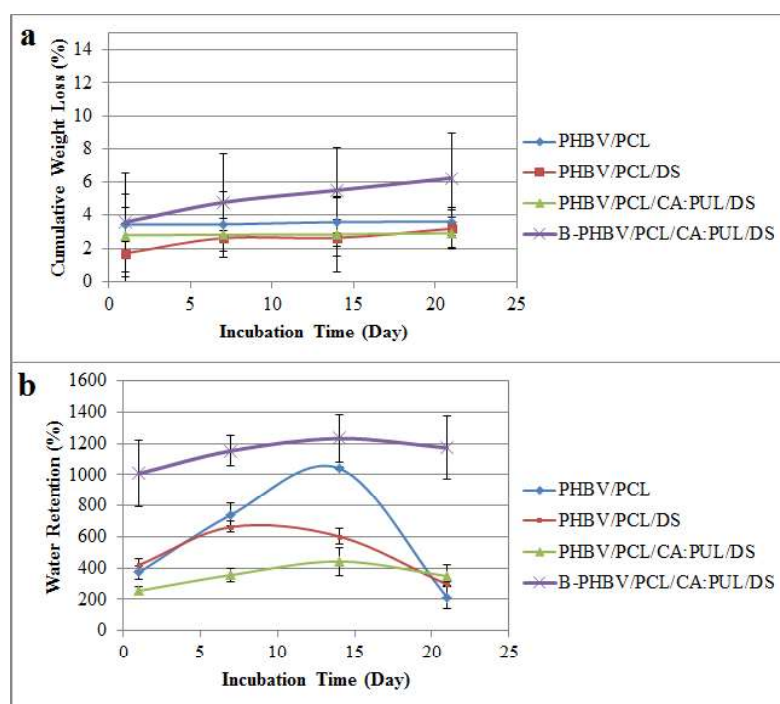


Figure 3.23. Cumulative weight loss (a) and water retention (b) results of scaffold groups incubated for 21 days.

Cumulative weight loss of scaffold groups under enzymatic degradation is presented in Figure 3.24a. Scaffold samples were subjected to lysozyme solution (1 mg/mL) for 14 days and weight change was measured after 4, 7 and 14 days of incubation. The weight loss of scaffold groups containing only PHBV/PCL fibers was slow and at the end of 14 days both PHBV/PCL and PHBV/PCL/DS scaffold groups showed around 8% weight loss. This result showed that presence of DS in line with PHBV/PCL fibers did not create difference in fiber weight loss. Due to hydrophobic nature of PHBV and PCL polymers a slower weight loss was expected for PHBV/PCL and PHBV/PCL/DS scaffold groups. On the other hand, co-electrospun scaffold groups, PHBV/PCL/CA:PUL/DS and B-PHBV/PCL/CA:PUL/DS, showed increasing weight loss. The presence of PUL in co-electrospun fibers was increased total weight loss since pullulan fibers were more hydrophilic and susceptible to degradation. The smaller diameter of PUL fibers ($1.58 \pm 0.2 \mu\text{m}$) in the structure with high surface to volume ratio could have further increased the weight loss for PUL fibers. After 7 and 14 days of weight loss the change in the polymer coating of DS was observed by SEM (Figure 3.24b). After 7 days of incubation approximately half of the DS were still covered in polymer coating while some DS was lost surface polymer coating through polymer loss. After 14 days of incubation majority of the DS was lack of polymer coating on their surface which was occurred due to increasing weight loss of PUL fibers.

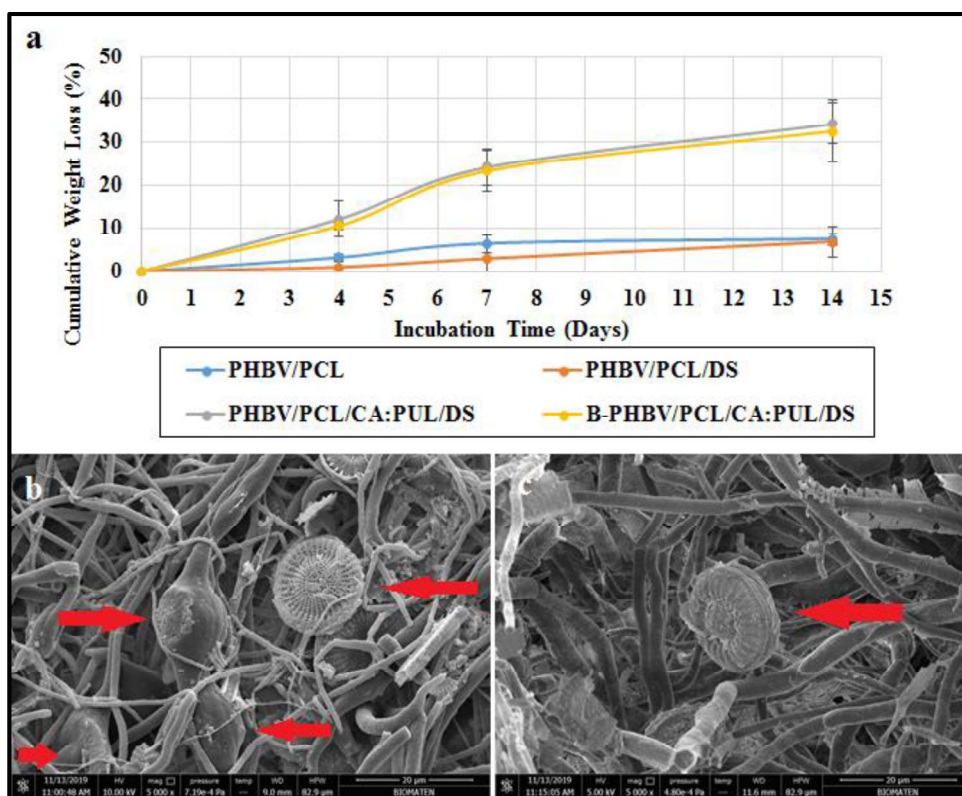


Figure 3.24. Cumulative weight loss of scaffold groups under lysozyme (1 mg/mL) degradation through 14 days of incubation (a). SEM images of B-PHBV/PCL/CA:PUL/DS scaffold after 1 (b) and 2 (c) weeks of degradation. Arrows show DS morphology in between fibers. Scale bars show 20 μ m length.

3.8 Calcium Deposition on Scaffold Groups

The amount of calcium deposited on the scaffolds was calculated from the decrease in the calcium amount in their incubation medium (SBF). Results were converted to percentages by accepting calcium amounts of control SBF as 100% (Figure 3.25). After 14 days of incubation, the calcium deposition on PHBV/PCL scaffold was nearly zero. However, scaffold with same polymer composition showed an increased calcium deposition up to 20% when DS is incorporated into fibers. This outcome indicates the positive effect of DS on calcium deposition. The calcium deposition on CA loaded group (PHBV/PCL/CA scaffold) was also around 20%. This was an

unexpected outcome related with CA as there is no direct report on interaction between CA and calcium in literature. However, study of Sultana et al., have investigated influence of essential and trace elements on CA antibiotic activity and showed that calcium can be an antagonist for CA antibacterial activity which could show possible binding off calcium (Najma Sultana & Arayne, 2002). The observed increase in calcium deposition on scaffold with CA presence, creates an advantage for CA use for bone infections. CA loading could support a dual effect which are antibiotic treatment and increased calcium deposition. Calcium deposition on co-electrospun group have increased after 7 days of incubation which shows the positive effect of DS and CA on calcium deposition. After 14 days, calcium deposition of groups become similar and the reason of decrease in calcium deposition on co-electrospun scaffold could be separation of deposited calcium plaques from the scaffold surface as the media was replenished at 7 day time point since high calcium deposition can create unstable aggregation points on the scaffold. Amount of calcium deposition on B-PHBV/PCL/CA:PUL/DS scaffold increased on the 7th day and decreased on the 14th day, which was a similar result with PHBV/PCL/CA:PUL/DS scaffold.

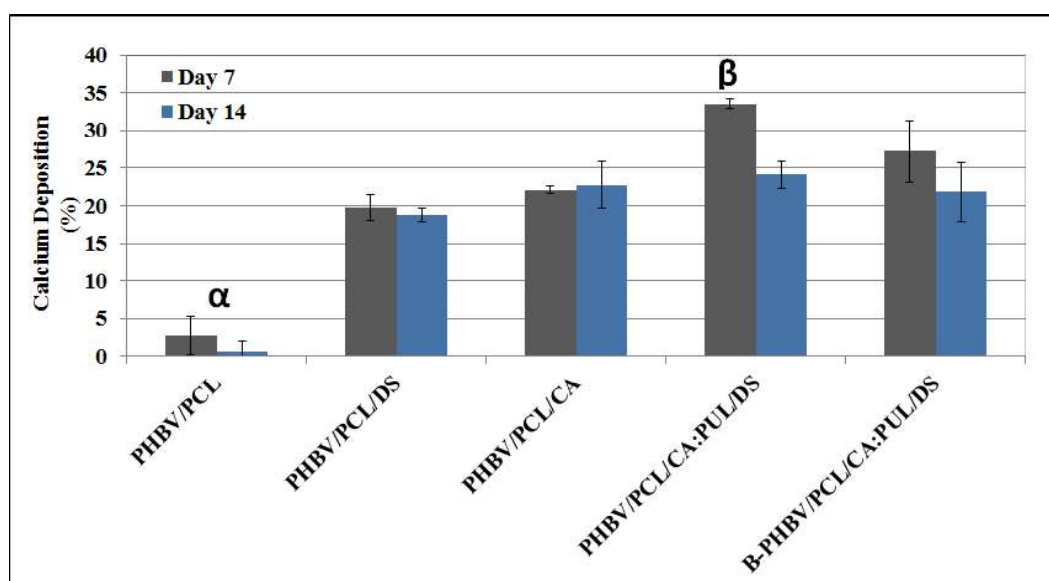


Figure 3.25. The amount of calcium deposited onto scaffold groups after 7 and 14 days of incubation in SBF. α : Indicates the statistically significant difference of PHBV/PCL group from other groups after 7 and 14 days of incubation. β : Indicates the statistically significant difference of the co-electrospun group from PHBV/PCL/DS and PHBV/PCL/CA groups after 7 days of incubation. ($p < 0.05$).

3.9 Fiber Morphology of Scaffold Groups

Average fiber diameters of PHBV/PCL, PHBV/PCL/DS and PHBV/PCL/CA scaffold groups were measured as 1.38 ± 0.2 , 2.47 ± 0.5 and 1.62 ± 0.2 μm . Average fiber diameters of PHBV/PCL/CA and PUL/DS phases of the co-electrospun scaffold were measured as 860 ± 170 nm and 1.58 ± 0.2 μm . Incorporating DS particles to PHBV/PCL fibers resulted in thicker fiber formation (2.47 ± 0.5). In co-electrospun scaffold, fiber diameter of PHBV/PCL/CA phase decreased to nano size. This result has obtained by change in the electric field created in co-electrospun system. The effect of electric field change on fiber morphology have been reported in the study of Li et al. Study have showed that electric field distribution can change jet directory which can effect frequency and strength of whipping (Xiang Li et al., 2016). Two syringe system with two power supply created two concurrent electric fields and this

change in electric field distribution could have decreased the fiber diameter of PHBV/PCL/CA fiber phase by creating stronger whipping. Study of Tuzlakoglu et al., have reported that the combination of nano and micro fibers together, have improved ALP activity and proliferation of Saos-2 cells which creates similarities with bone extracellular environment (Tuzlakoglu et al., 2005). In this study, nano fibers of co-electrospun scaffold have created higher surface area for cell interaction while micro fibers have improved mechanical properties of scaffold.

SEM images were taken to examine the fiber morphologies of PHBV/PCL (Figure 3.26a) and PHBV/PCL/CA:PUL/DS (Figure 3.26c) scaffolds produced with commercially obtained PHBV, B-PHBV/PCL (Figure 3.26b) and B-PHBV/PCL/CA:PUL/DS (Figure 3.26d) produced by produced PHBV. PHBV/PCL fibers produced with produced PHBV were thicker than fibers produced with commercially obtained PHBV. This is due to the fact that produced PHBV showed higher solubility in HFIP and form a solution with high viscosity. In electrospinning of commercially obtained PHBV, polymer solution concentration was optimized as 14% wt/v, while the B-PHBV solution was optimized as 10% wt/v since electrospinning could not be performed due to the density at higher concentrations of B-PHBV. Average fiber diameter of produced PHBV was measured as $4.51 \pm 1.5 \mu\text{m}$. The diameter of the PUL fibers in the PHBV/PCL/CA:PUL/DS and B-PHBV/PCL/CA:PUL/DS scaffold groups were $2.10 \pm 0.6 \mu\text{m}$ and $2.5 \pm 0.7 \mu\text{m}$ which were similar. However, the diameter of PHBV/PCL fibers was $0.46 \pm 0.15 \mu\text{m}$ in PHBV/PCL/CA:PUL/DS, whereas in B-PHBV/PCL/CA:PUL/DS scaffold, these fibers diameter were increased to $4.98 \pm 1.3 \mu\text{m}$ due to increased viscosity of polymer solution during electrospinning. Water contact angle analysis showed that presence of PUL/DS fibers entangled with PHBV/PCL fibers decreased the water contact angle of scaffold surface. Water contact angle of B-PHBV/PCL was 115.4° , while water contact angle of B-PHBV/PCL:PUL/DS was decreased to 89.3° , indicating increased hydrophilicity.

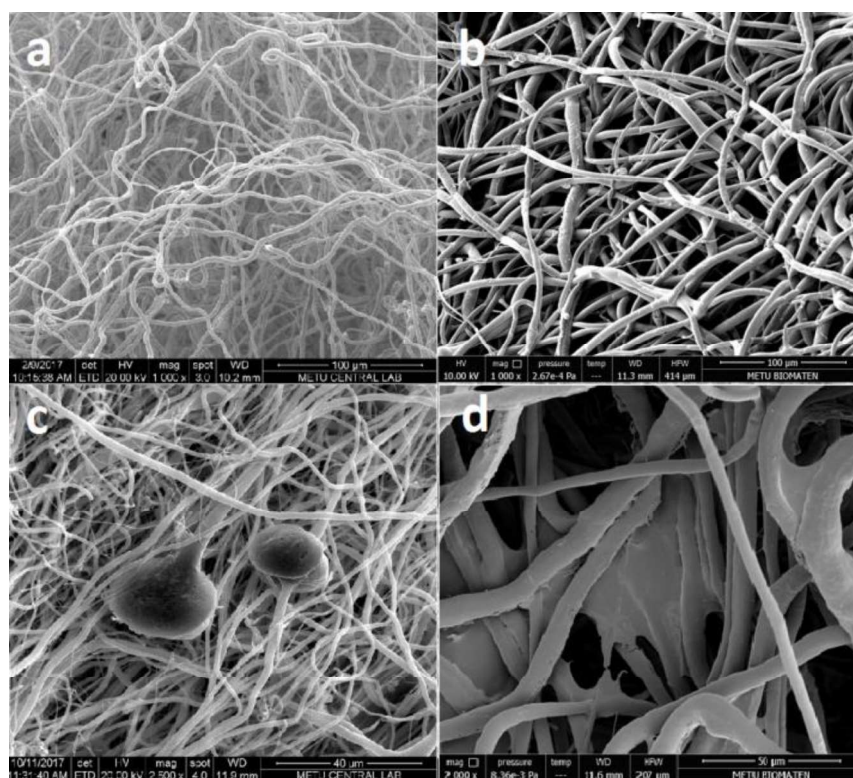


Figure 3.26. SEM images of PHBV/PCL (a) B-PHBV/PCL (b) PHBV/PCL/CA:PUL/DS (c) and B-PHBV/PCL/CA:PUL/DS (d) scaffold groups. Images were taken at 1000X (a and b) and 2000X (c and d) magnifications while scale bars show 100 μm (a and b), 40 μm (c) and 50 μm (d) lengths.

3.10 Efficiency of Cefuroxime Axetil Loading and Release Profiles of the Scaffolds

High loading of CA into PHBV/PCL fiber phase was achieved since CA has a hydrophobic nature that enabled more retention in hydrophobic polymer structure during collection of fibers in ethanol bath. Hydrophobic drug molecules are expected to homogeneously distribute in hydrophobic fibers within a good solvent that increase miscibility of both drug and polymer (Yuan et al., 2018). As the drug molecules distributed in the 3D volume of polymer fiber, less amount of drug molecules is expected to stay on the surface. As a result of this, the loss of entrapped CA molecules from the fiber surface to the ethanol bath was expected to be low.

Entrapment efficiency of CA into PHBV/PCL and PHBV/PCL/CA:PUL/DS and B-PHBV/PCL/CA:PUL/DS scaffolds were calculated as $92\pm 9.6\%$, $93\pm 11.7\%$ and $89\pm 10.7\%$. Entrapment efficiency of CA into DS was calculated as $66\pm 7.4\%$. The release of CA from DS was compared with CA release from PHBV/PCL fibrous scaffolds (Figure 3.27). Besides that, CA loaded DS were also incorporated into PHBV/PCL fibers to prepare PHBV/PCL/DS group. Cumulative amount of released CA was below 22% for all groups probably owing to low solubility of CA in aqueous environment (Water solubility: 0.412 ± 0.03 mg/ml) (Sruti et al., 2013). Amount of CA released from DS was highest. However, release of CA from DS particles which are kept inside PHBV/PCL fibers showed a more sustained behavior up to 12 days ($\cong 10\%$). After 12 days of release PHBV/PCL/DS group showed higher CA release compared to CA release directly from PHBV/PCL fibers. Co-electrospun PHBV/PCL/CA:PUL/DS scaffold showed no initial burst release which was the support of dense fibrous matrix in co-electrospun scaffold. CA loading and release have reported for several delivery systems like microspheres, polymer-ceramic scaffolds, calcium phosphates and bioactive glasses (Nandi, Kundu, Ghosh, et al., 2009; Nandi, Kundu, Mukherjee, et al., 2009; Soundrapandian et al., 2011; Yaprakci et al., 2013). The use of local delivery systems can overcome the limitations of CA use like low oral adsorption and short serum half-life. With this study, CA was loaded into a scaffold with this composition first time in literature. The hydrophobic polymer based fibers of dual fiber scaffolds enabled high loading and well distribution of CA in the scaffold structure. Second fiber phase provided more compact 3-D network of stable fibers that can control water penetration/diffusion related events, swelling, degradation and drug release. Thus, PHBV/PCL/CA:PUL/DS and B-PHBV/PCL/CA:PUL/DS scaffolds sustained a stable CA release suggesting that it can be a promising local controlled delivery system.

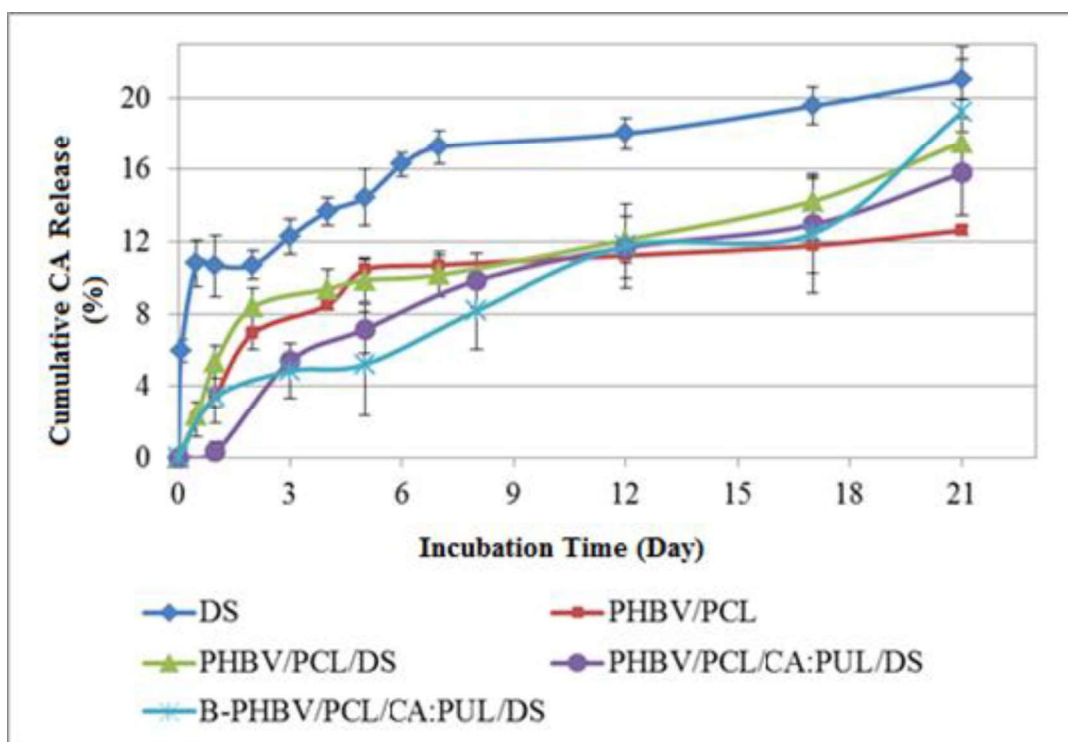


Figure 3.27. Percent cumulative CA release from scaffold groups through 21 days of incubation period. Release was studied in PBS at 37 °C (n = 4).

3.11 Mechanical Test Results of the Scaffolds

Electrospun scaffold systems are expected to endure high tensile forces due to entangled fibrous structure but possess low compressive strength. Bone tissue scaffold should bear to some extent of compression that will prevent collapse of the scaffold. These specific mechanical properties of fibrous mats lead their area of application to bone tissues that do not have to bear high compressive strength like maxillofacial bones, superficial defects, cranial defects or crack/void defects that can be filled with fibrous mats. Produced scaffolds were tested for tensile and compressive strength and results of mechanical tests are presented in Table 3.3 and 3.4. Representative stress strain curves for PHBV/PCL (Tension) and PHBV/PCL/DS (Compression) is presented in Figures 3.28 and 3.29.

3.11.1 Results of Tension Test

Incorporating DS into PHBV/PCL fibers increased the Young's modulus but decreased ultimate tensile strength (UTS) of PHBV/PCL/DS scaffold according to tension tests (Table 3.3). The incorporation of DS into fibers increased the fiber diameter which could have increased the modulus. On the other hand, DS and polymers lack interfacial interactions which could be the reason of decreased UTS. Co-electrospun scaffolds had denser fiber matrix with thick PUL fibers that could support high stiffness and modulus. In the study of Paşcu et al., young modulus of PHBV based electrospun scaffold under tensile force was presented as 0.7 ± 0.33 MPa. In the study, a higher tensile modulus was achieved with pure PHBV mat compared to PHBV/PCL fibrous mat that was produced in this study. The reasons of this was in the study of Paşcu et al, fibers were collected on an aluminum plate which resulted in densely packed fibers and fiber diameters have reported to range between 10 and 15 μm (Paşcu et al., 2013). In this study, PHBV/PCL fiber diameter was at least ten times lower 1.38 ± 0.2 which resulted in lower young modulus. On the other hand, tensile young modulus of PHBV/PCL/CA:PUL/DS scaffold group was improved to comparable values (0.51 ± 0.91 MPa) even though diameters of fiber phases were 860 ± 170 nm and 1.58 ± 0.2 μm for PHBV/PCL/CA and PUL/DS phases. While young modulus of B-PHBV/PCL/CA:PUL/DS scaffold was similar to PHBV/PCL/CA:PUL/DS scaffold even though PHBV/PCL fibers were thicker. A study has presented mechanical strength of PCL/Alginate fibrous scaffold produced with wet electrospinning. The results are comparable with this study since production method is similar. The maximum tensile strength and young modulus of PCL/Alginate scaffold have reported to be 54 ± 7 and 230 ± 20 kPa (M. S. Kim & Kim, 2014). In this study maximum tensile strength of PHBV/PCL/CA:PUL/DS was slightly lower (19.1 ± 1.4 kPa). However, co-electrospun scaffold showed higher young modulus under tensile force (515.2 ± 91.9 kPa).

Table 3.3 Tensile strength test results of scaffold groups. α : Statistical significant difference of PHBV/PCL/CA:PUL/DS and B-PHBV/PCL/CA:PUL/DS groups Young modulus results from other groups. β : Statistical significant difference of PHBV/PCL group ultimate tensile strength from PHBV/PCL/DS and B-PHBV/PCL/CA:PUL/DS groups.

Scaffold Groups	Young Modulus (kPa)	Ultimate Tensile Strength (kPa)
PHBV/PCL	95.2 \pm 3.1	22.3 \pm 2.8 ^{β}
PHBV/PCL/DS	125.3 \pm 10.9	13.5 \pm 5.5 ^{β}
PHBV/PCL/CA:PUL/DS	515.2 \pm 91.9 ^{α}	19.1 \pm 1.4
B-PHBV/PCL/CA:PUL/DS	460 \pm 79.1 ^{α}	16 \pm 2.7 ^{β}

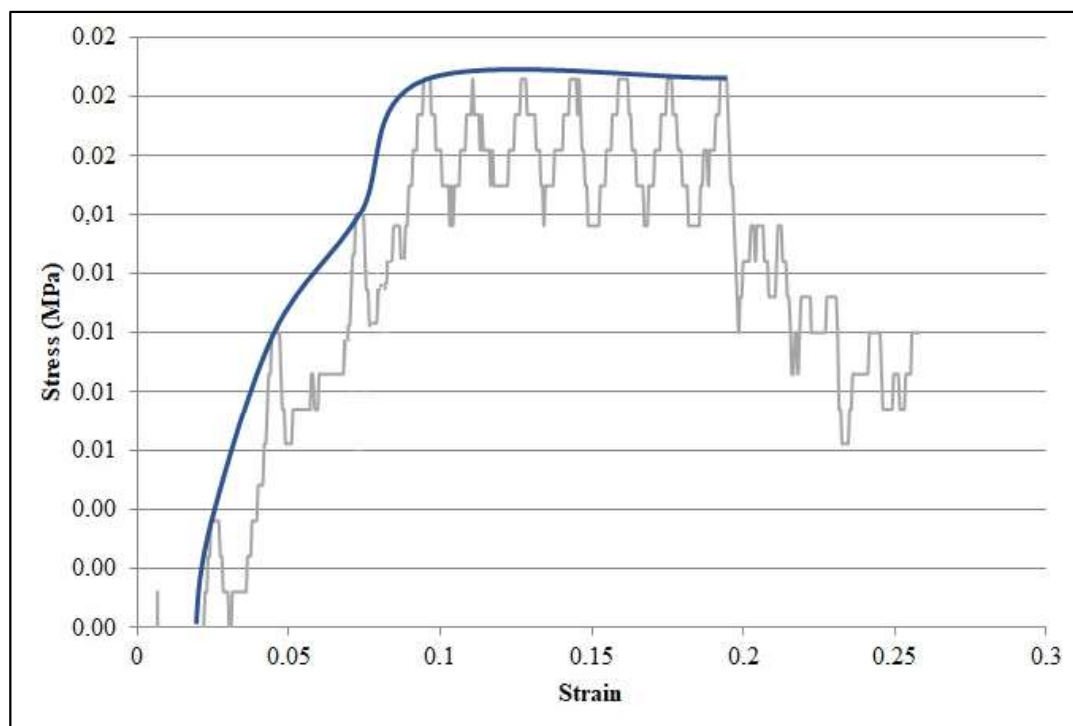


Figure 3.28. Representative stress strain curve for PHBV/PCL scaffold under tensile load.

In order to investigate if embedded DS particles create weakness in polymer fibers, PUL/DS mesh was subjected to tensile force until break and the break point of fiber mesh was observed under SEM (Figure 3.29a and b). Images showed that fibers' break points were random and was not specifically at DS incorporated points. The fiber break line can be observed from the SEM images and arrow shows a DS particle close to break point which was still in the fiber mesh.

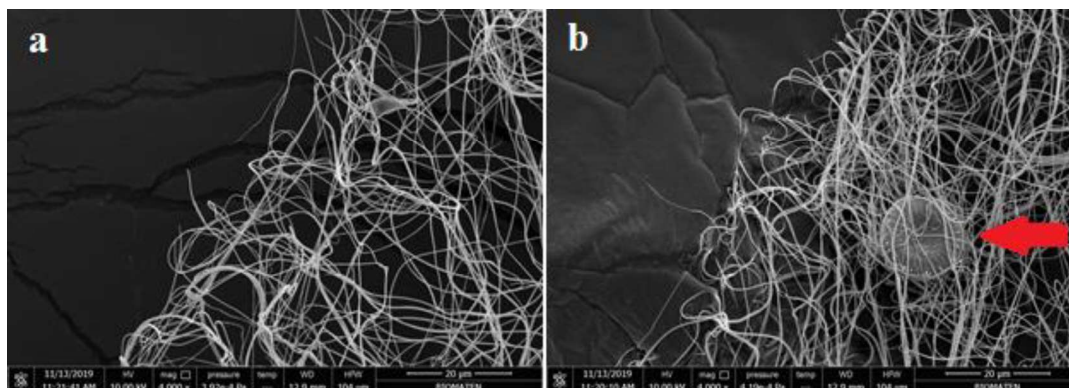


Figure 3.29. SEM images of fibers breaking point when tensile force is applied. Arrow shows DS in between fibers. Scale bars show 20 μm length.

3.11.2 Results of Compression Test

According to Compression Tests, PHBV/PCL/DS scaffold had higher Modulus and compressive strength compared to PHBV/PCL fibers (Table 3.4). Representative stress strain curve for PHBV/PCL is presented in Figure 3.30. Loading of DS has increased the fiber size and circular shape of the shells filled some of the pores increasing physical support within fiber mesh. PHBV/PCL/CA:PUL/DS scaffold has higher modulus and compressive strength (10.63 ± 3.05 and 5.33 ± 2.65 kPa) compared to single phase scaffolds, since co-electrospun scaffold have both PHBV/PCL fibers and DS loaded PUL fibers which are densely packed. B-PHBV/PCL/CA:PUL/DS scaffold has the highest young modulus and compressive strength (13.75 ± 2.30 and 7.29 ± 3.12 kPa) since B-PHBV/PCL fiber phase in this group is thicker compared to other groups. The method of wet electrospinning aims to improve porosity of scaffolds by creating 3D fibrous mats. As the pores between fibers become larger,

the resistance to any compressive force will decrease. Many wet electrospun scaffold studies have not considered and presented mechanical testing results on their scaffolds. The study of Kim et al., that have presented compressive strength and young modulus (30.5 ± 5.3 kPa) of PCL/Alginate fibrous scaffold produced with wet electrospinning, also found low compressive strength. Compressive modulus as low as 3.6 ± 0.3 kPa have reported for wet electrospun PCL scaffold which is similar to the compressive modulus found for PHBV/PCL in this study (M. S. Kim & Kim, 2014). The study of You et al., have presented 3D nanofibrous scaffolds produced by thermally induced nanofiber self-agglomeration method which is 3D agglomeration of electrospun nanofibrous mats/pieces in a bath and freeze drying to form 3D porous fibrous mats. Compressive strength of produced mats has reported to be low and as an in vivo application, study have applied fibrous scaffolds to critical-sized cranial bone defect of mouse. Study have showed the successful use of 3D fibrous mats for treatment of the defect on non-load bearing bones like cranial bones (Yao et al., 2017).

Table 3.4 Compressive strength test results of scaffold groups. α : Statistical significant difference of B-PHBV/PCL/CA:PUL/DS groups' Young modulus result from PHBV/PCL and PHBV/PCL/DS groups. β : Statistical significant difference of B-PHBV/PCL/CA:PUL/DS groups' compressive strength result from PHBV/PCL and PHBV/PCL/DS groups results.

Scaffold Groups	Young Modulus (kPa)	Compressive Strength (%40 Strain) (kPa)
PHBV/PCL	$2.42 \pm 0.52^{\alpha}$	$1.25 \pm 0.73^{\beta}$
PHBV/PCL/DS	$8.15 \pm 2.47^{\alpha}$	$2.08 \pm 0.71^{\beta}$
PHBV/PCL/CA:PUL/DS	10.63 ± 3.05	5.33 ± 2.65
B-PHBV/PCL/CA:PUL/DS	$13.75 \pm 2.30^{\alpha}$	$7.29 \pm 3.12^{\beta}$

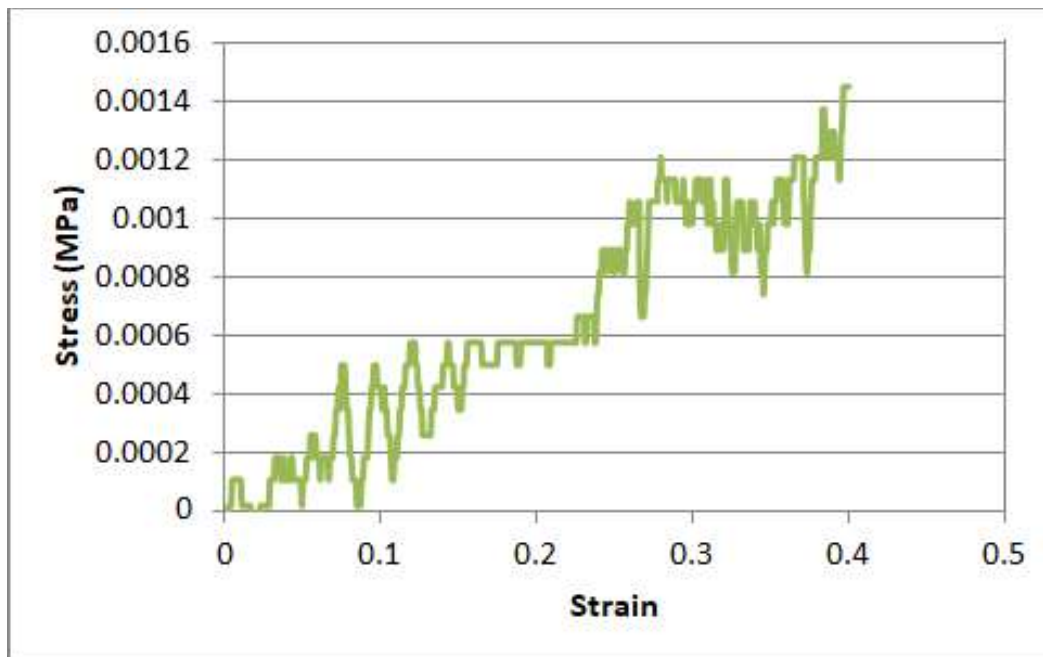


Figure 3.30. Representative stress strain curve for PHBV/PCL scaffold under compressive load.

3.12 Results of In Vitro Cell Culture Experiments

3.12.1 Saos-2 and L929 Cell Viability on Scaffold Groups

Cell viability on the PHBV/PCL, PHBV/PCL/CA, PHBV/PCL/DS, and PHBV/PCL/CA:PUL/DS groups was measured by the Alamar Blue viability test and compared with cell viability on B-PHBV/PCL and B-PHBV/PCL/CA:PUL/DS groups produced by synthesized PHBV. Saos-2 and L929 cells were selected for viability testing. The loading of CA into PHBV/PCL fibers in the scaffold was found to have no negative effect on cell viability. It was observed that DS-containing groups increased cell viability after the 4th and 7th days compared to the other groups. Cytotoxicity caused by the size, dose and shape of the DS shells has been reported in a recent study in the literature that small, uneven and high doses of DS lead to cell death (Xiang Zhang et al., 2018). The inclusion rates of small sized DS particles into the cell membrane can be higher and this interaction can create reactive

oxygen species, reducing cell viability. In this study, it was shown that when DS used in their original size, did not decrease the cell viability and the SEM images showed that the cells were attached to the DS surface. It is known that silicon released from DS in scaffolds will enhance osteogenic properties. Silicone has been reported to increase osteoblast activity, silicic acid increases IGF-I growth factor production and inhibits cell death (E.-J. Kim et al., 2013). In previous studies, it was reported that the bioactivity of chitosan membranes and scaffolds produced from silk fibroin and their suitability to bone tissue engineering could be increased by adding diatomite (Le et al., 2018a; Tamburaci & Tihminlioglu, 2017). Tamburaci and Tihminlioglu (2018) also reported that bioactivity of Saos-2 cells increased when they used diatomite in chitosan sponges in diatomite concentration range of 1-10% by weight (Tamburaci & Tihminlioglu, 2018). In B-PHBV/PCL and B-PHBV/PCL/CA:PUL/DS groups, synthesized PHBV showed no negative effect on cell viability (Figure 3.31). The co-electrospun B-PHBV/PCL/CA:PUL/DS group appears to support higher cell viability at day 1 compared to other groups. Cell viability increased at the same rate as other groups in the following days. Taking these results into consideration, fibers of B-PHBV/PCL supported better cell adhesion and attachment on the first day.

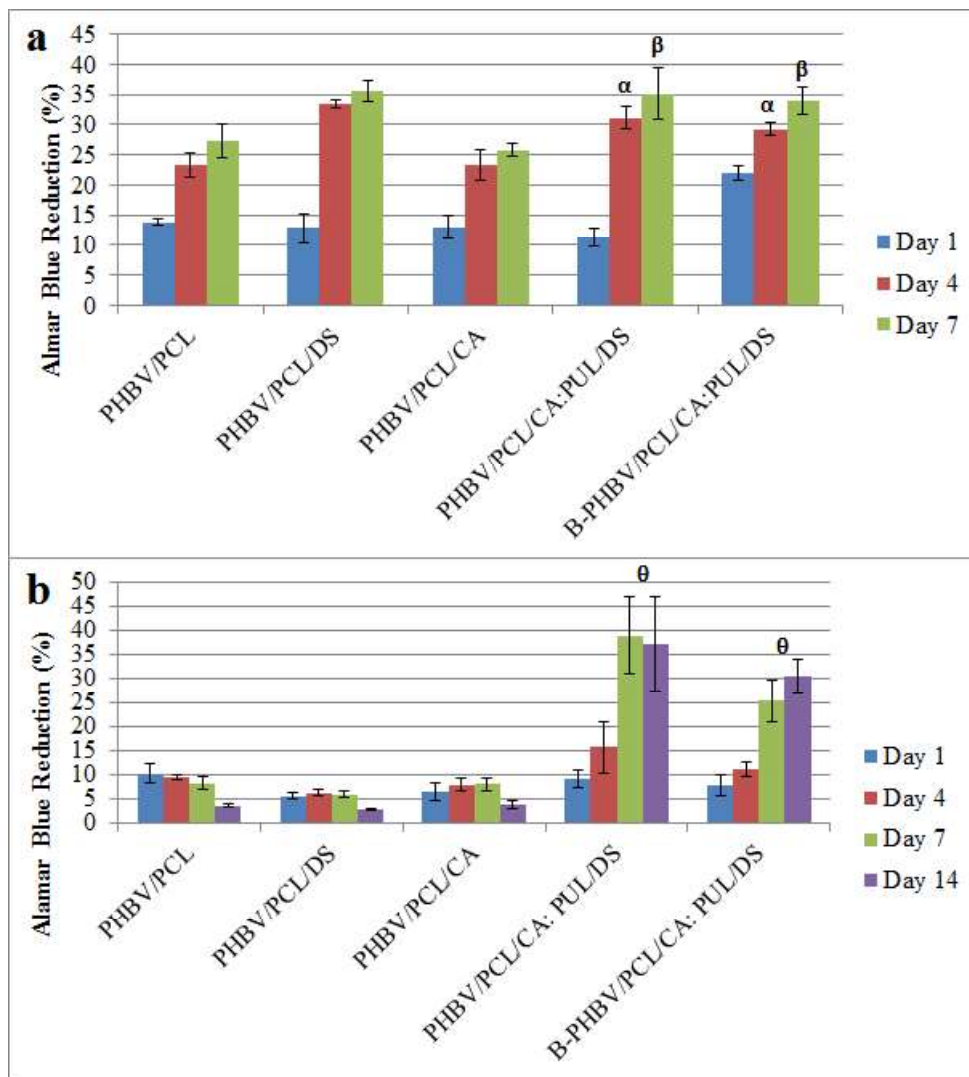


Figure 3.31. The Alamar Blue reduction of Saos-2 (a) and L929 (b) cells grown on scaffold groups through 1, 4 and 7 days of incubation periods. α : Statistically significant difference of PHBV/PCL/CA:PUL/DS and B-PHBV/PCL/CA:PUL/DS from PHBV/PCL and PHBV/PCL/CA groups after 4 day of incubation ($p < 0.05$). β : Statistically significant difference of PHBV/PCL/CA:PUL/DS and B-PHBV/PCL/CA:PUL/DS from PHBV/PCL/CA group after 7 day of incubation ($p < 0.05$). θ : Statistically significant difference of PHBV/PCL/CA:PUL/DS and B-PHBV/PCL/CA:PUL/DS groups from other groups after 7 and 14 days of incubation ($p < 0.05$).

3.12.2 Cell Morphology and Attachment Analysis by Scanning Electron Microscopy

The morphology of proliferated Saos-2 cells on scaffold groups were investigated by SEM analysis (Figure 3.32). After 7 days of incubation, cell populations on PHBV/PCL and PHBV/PCL/CA scaffolds were observed to be seldom with some smaller clusters (Figure 3.32a and c, respectively). On the other hand, denser cell populations were observed on PHBV/PCL/DS and PHBV/PCL/CA:PUL/DS scaffolds. The positive effect of DS doping on scaffolds in terms of Saos-2 cell proliferation and spreading was observed.

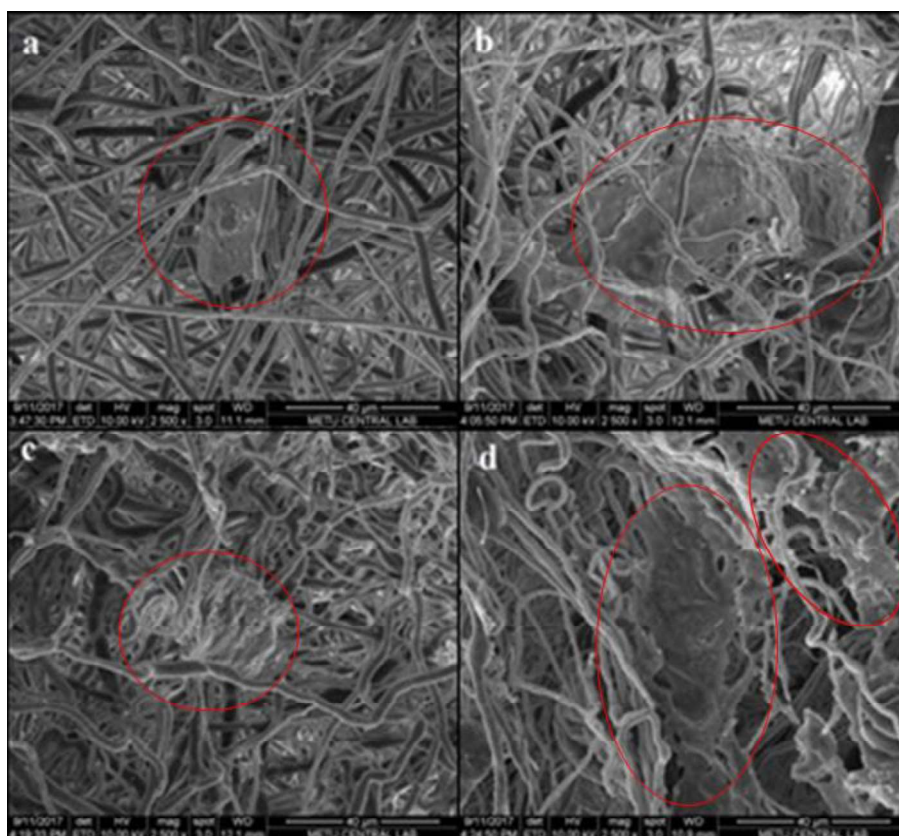


Figure 3.32. SEM images of Saos-2 cells after 7 days of incubation on scaffold groups (a) PHBV/PCL, (b) PHBV/PCL/DS, (c) PHBV/PCL/CA and (d) PHBV/PCL/CA:PUL/DS. Images were taken at 2500X magnifications while scale bars show 40 μ m length. Red circles show cells on fibers.

The SEM images of proliferated Saos-2 cells on B-PHBV/PCL and B-PHBV/PCL/CA:PUL/DS scaffold groups are shown in Figure 3.33. The fibers of the B-PHBV/PCL scaffold were found to be thicker. Cells are seen on thick fibers, lying on a single fiber or attached to the fibers at the junctions (Figure 3.33a and b). The cells lying on thick fibers have been found to have a thin and long morphology. In the B-PHBV/PCL/CA:PUL/DS scaffold group, the denser fiber matrix formed by co-electrospun fiber phases has created areas where the cells can easily spread on. Cells appear to be spread on fibers close to each other (Figure 3.33c and d). It has been observed in the SEM analyzes that the cells have a healthy morphology around the DS on the B-PHBV/PCL/CA:PUL/DS scaffold and grow around by attaching to the DS (Figure 3.33c).



Figure 3.33. SEM images of Saos-2 cells proliferating for 7 days on B-PHBV/PCL (a and b) and B-PHBV/PCL/CA:PUL/DS (c and d) scaffold groups. (Arrows: Cells on fibers). The scale bars on the images show 20 µm length.

3.12.3 Alkaline Phosphatase Activity and Calcium Deposition on Scaffold Groups

The optimum DS dose required to increase ALP activity was investigated by producing PHBV/PCL scaffolds containing different amounts of DS and examining the ALP activity of Saos-2 cells grown on the scaffolds (Figure 3.34a). On day 7 of incubation, scaffolds containing DS at a ratio of 64:1, 32:1, 16:1 and 8:1 PHBV/PCL:DS showed higher ALP activity than the control group. In view of this result, it was decided to continue the ALP activity experiments with 20:1 PHBV/PCL:DS ratio originally selected in the scaffolds. Figure 3.34 shows the ALP activity of Saos-2 cells seeded on scaffolds after 7 and 14 days of incubation. On day 7 of incubation, the CA loaded PHBV/PCL/CA group showed higher ALP activity than other scaffolds. After 14 days of incubation, all scaffolds groups showed a similar rate of ALP activity. In the study of Tamburaci and Tihminlioglu (2017; 2018), similar results were found in the ALP assay with Saos-2 cells planted on chitosan membranes, groups containing diatomite did not increase ALP activity compared to other groups, but delayed development of ALP activity after 21 days was proposed (Tamburaci & Tihminlioglu, 2017, 2018). The increase in ALP activity in diatomite-containing groups has been explained by the increase in osteoblastic activity due to silicon and other minor elements in diatomite structure and it is emphasized that it mimics natural tissue because it is also a minority elements in natural bone structure (López-Álvarez et al., 2009). When the intracellular calcium contents of Saos-2 cells incubated on scaffolds were compared after ALP test, parallel results were obtained with ALP test results, and no difference was observed between intracellular calcium levels in scaffold groups.

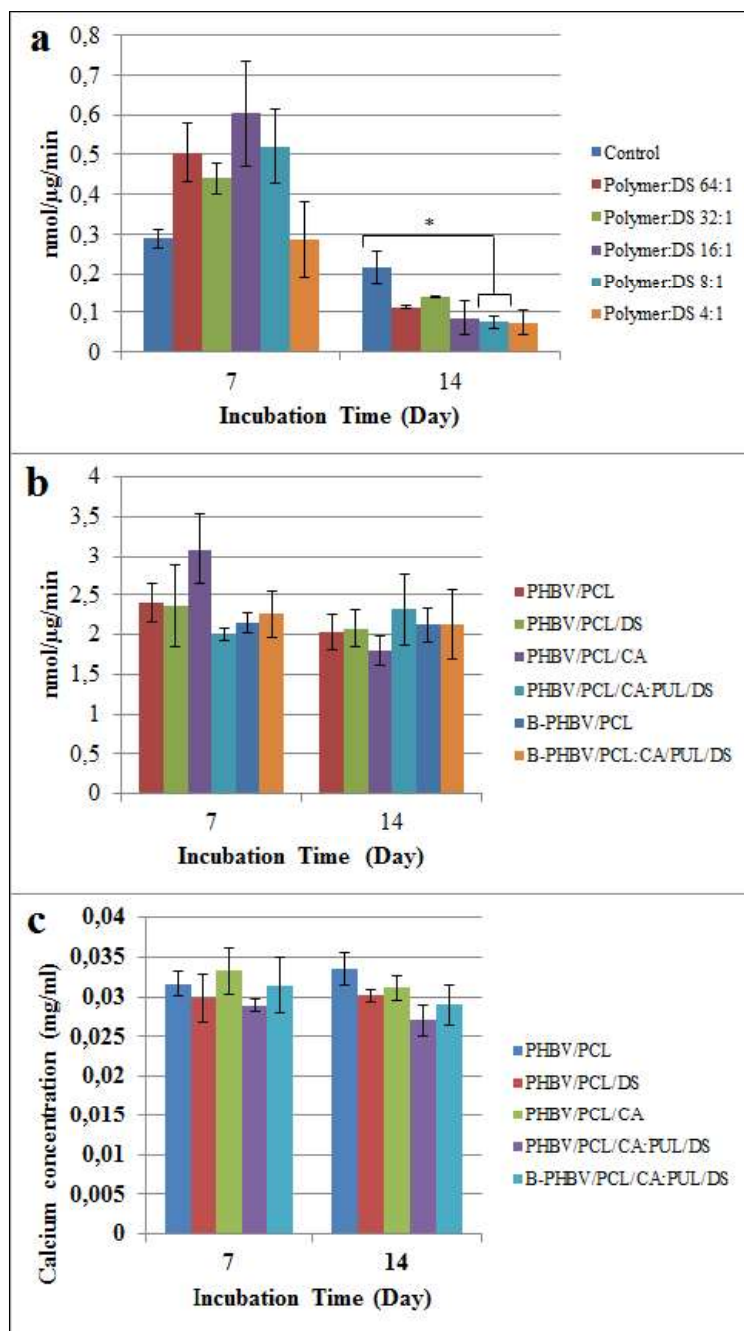


Figure 3.34. Saos-2 cell ALP activity after 7 and 14 days of incubation on PHBV/PCL scaffolds containing different concentrations of DS. Saos-2 cells grown as PHBV/PCL scaffold without DS was the control group (a). ALP activities of Saos-2 cells grown on scaffold groups after 7 and 14 days of incubation (b). As a result of the ALP activity assay, intracellular calcium levels of Saos-2 cells proliferated on scaffold groups (c).

3.12.4 Cell Morphology and Distribution Analysis by Laser Scanning Confocal Microscopy

The distribution and morphology of Saos-2 cells on scaffold groups were visualized by laser scanning confocal microscopy (PHBV/PCL, PHBV/PCL/DS, PHBV/PCL/CA, PHBV/PCL/CA:PUL/DS and B-PHBV/PCL/CA:PUL/DS) (Figure 3.35). Actin filaments in the cytoplasm and nucleus of the cells were labeled respectively with FITC and PI dyes. The merged images of FITC and PI labeling displayed exact location and morphology of cells. All scaffold groups have supported cell infiltration and images were formed after merging of z-stack images. The cell density on PHBV/PCL and PHBV/PCL/CA scaffold groups was low (Figure 3.35a and c). In contrary, DS bearing PHBV/PCL/DS and co-electrospun scaffolds showed higher cell density (Figure 3.35b, d and f). Some of the cells on the B-PHBV/PCL scaffold were covered a larger area, while some of the cells were in round morphology (Figure 3.35e). The fact that the cells were close to the round morphology indicates that they do not interact adequately with their environment and cannot propagate in a healthy way. This is due to the hydrophobic character of the fibers in the B-PHBV/PCL scaffold. Healthy morphology of cells on B-PHBV/PCL/CA:PUL/DS scaffold was observed with spread cell morphology on the fibers with filopodia extensions (Figure 3.35f). Spread cells were appeared to be directed towards the fiber directions in some parts of the scaffold. The co-electrospun B-PHBV/PCL/CA:PUL/DS scaffold has increased the cell adhesion and spread by adding hydrophilic properties to the structure with PUL fibers (Figure 3.35g). The cell spreading areas were calculated from confocal images and results showed that cells grown on co-electrospun scaffolds covered larger areas by larger spreading. Cell adhesion was reported to be improved by increasing of hydrophilicity of hydrophobic surfaces (Bauer et al., 2008). Kim et al., have reported that when hydrophilicity was achieved by co-electrospun PCL and PVA fibers, cell attachment and spreading were improved (C. H. Kim et al., 2006). This result proves that presence of PUL fibers in the co-electrospun fibers improved cell spreading and

created a healthier environment for growth. Results of confocal microscopy analysis shows that PHBV/PCL/CA:PUL/DS and PHBV/PCL/CA:PUL/DS co-electrospun scaffolds can support better cell infiltration and spreading compared to other scaffold groups and thus, it is convenient for bone tissue engineering.

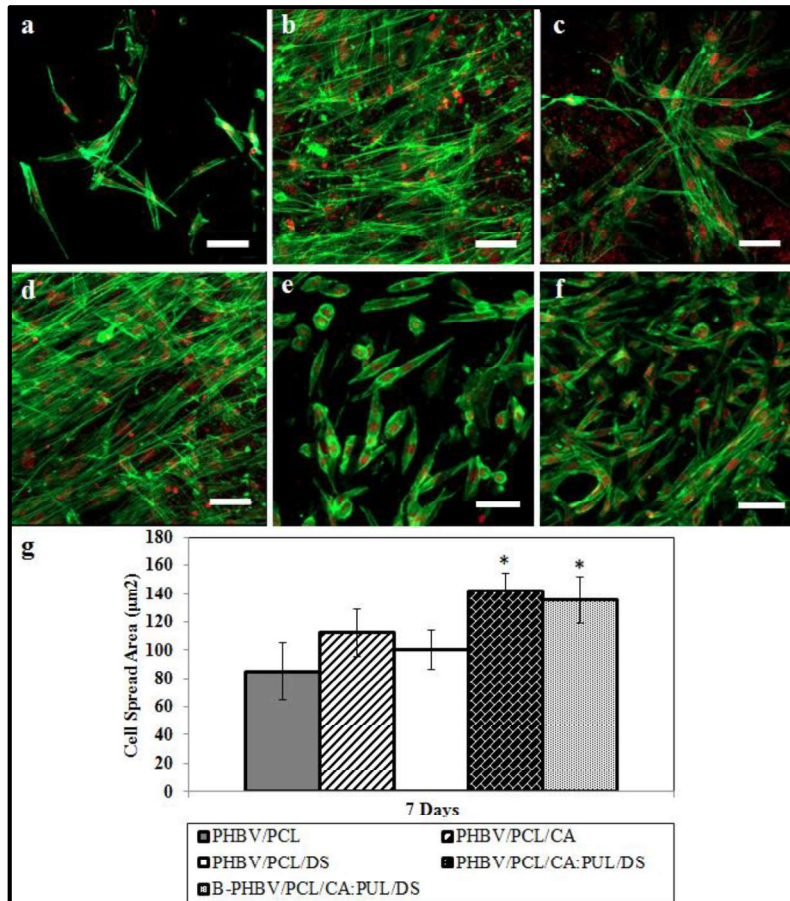


Figure 3.35. Laser-scanning confocal microscopy images of Saos-2 cells grown for 7 days on PHBV/PCL (a), PHBV/PCL/DS (b), PHBV/PCL/CA (c), PHBV/PCL/CA:PUL/DS (d), B-PHBV/PCL (e) and B-PHBV/PCL/CA:PUL/DS (f) scaffold groups. The cell cytoplasm was labeled with FTIC (Green) and nuclei was labeled with Draq5 (Red) fluorescent dyes (CSLM, Leica DM2500, Germany). Average cell spreading areas of Saos-2 cells that were proliferated on scaffold groups after 7 days of incubation (g). Scale bars (a-f) show 50 μm length. *: Statistically significant difference of PHBV/PCL/CA:PUL/DS and B-PHBV/PCL/CA:PUL/DS groups from PHBV/PCL group.

CHAPTER 4

CONCLUSION

In this thesis, co-electrospinning method was used to produce a dual fiber phase scaffold bearing both hydrophobic PHBV/PCL fiber and DS entrapped hydrophilic PUL fiber phases. In the study, the effect of DS entrapment in fibers was investigated for bone tissue engineering. The foreseen use of this co-electrospun scaffold in bone tissue engineering planned to be on non-load bearing bone tissues, filler in bone cracks and as an interphase between bone implants. In the optimization phase, cell culture studies have proved that DS, in their original size and shape had no cytotoxicity over Saos-2 cells. Improved cell viability was recorded at certain DS dose which was selected to be used in fibrous scaffolds to promote cell viability. In order to achieve stable PUL fiber phase, a GTA cross-linking method that was reported to be used to cross-link PUL films was modified and optimized as an in situ crosslinking method. Single phase, cross-linked PUL fibers that are stable for long periods in aqueous media was produced for the first time in this study. The PHBV polymer was also produced by a bacterial strain and characterized successfully in this study. A second co-electrospun group was prepared by using produced PHBV for comparison through the study. Produced scaffold groups were characterized in terms of morphology, mechanical properties, porosity, weight loss, water retention, calcium deposition and CA release. The effect of DS loading on mechanical properties was evaluated and it was observed that DS doping increases young modulus while decreases tensile properties. Denser fibrous structure and presence of DS in fibrous mass improved compressive strength of co-electrospun scaffolds compared to single phase scaffolds. Porosity and pore size distribution of scaffold groups were in the range that supports tissue ingrowth. Due to hydrophobic fiber phase and successful crosslinking of PUL, scaffolds were able to preserve unity

through enzymatic degradation. Presence of DS in scaffolds have shown to improve cell viability and spreading while confocal microscopy study have shown that co-electrospun scaffolds have supported higher cell viability with healthier cell morphology compared to single phase scaffolds. Future studies can investigate the in vivo application of co-electrospun scaffold for non-load bearing bone tissues like cranial bone defects, maxillofacial bones. Co-electrospun mats can also be used to support tissue-implant interface in bone implant applications. The co-electrospun scaffold have mainly formed with materials with natural origin and only small amount of synthetic polymer, PCL, was included to support smoother fiber morphology. Use of natural materials in scaffolds support biocompatibility. Study showed that PHBV polymer can be synthesized and optimized to be used in scaffold structure. Likewise natural polysaccharide PUL and silica shells of diatoms can be produced and used in fabrication of this scaffold. All these results are supporting the conclusion that co-electrospun PHBV/PCL/CA:PUL/DS and B-PHBV/PCL/CA:PUL/DS scaffold groups are promising candidates for applications in bone tissue engineering.

REFERENCES

- Alford, J. R., Kendrick, B. S., Carpenter, J. F., & Randolph, T. W. (2008). Measurement of the second osmotic virial coefficient for protein solutions exhibiting monomer-dimer equilibrium. *Analytical Biochemistry*, *377*(2), 128–133. <https://doi.org/10.1016/j.ab.2008.03.032>
- Amini, A. R., Laurencin, C. T., & Nukavarapu, S. P. (2012). Bone tissue engineering: Recent advances and challenges. *Critical Reviews in Biomedical Engineering*, *40*(5), 363–408. <https://doi.org/10.1615/CritRevBiomedEng.v40.i5.10>
- Anusuya, G. S., Kandasamy, M., Raja, S. A. J., Sabarinathan, S., Ravishankar, P., & Kandhasamy, B. (2016). Bone morphogenetic proteins: Signaling periodontal bone regeneration and repair. *Journal of Pharmacy and Bioallied Sciences*, *8*(Suppl 1), S39–S41. <https://doi.org/10.4103/0975-7406.191964>
- Aramvash, A., Hajizadeh-Turchi, S., Moazzeni-zavareh, F., Gholami-Banadkuki, N., Malek-sabet, N., & Akbari-Shahabi, Z. (2016). Effective enhancement of hydroxyvalerate content of PHBV in *Cupriavidus necator* and its characterization. *International Journal of Biological Macromolecules*, *87*, 397–404. <https://doi.org/10.1016/j.ijbiomac.2016.03.002>
- Atila, D., Keskin, D., & Tezcaner, A. (2016). Crosslinked pullulan/cellulose acetate fibrous scaffolds for bone tissue engineering. *Materials Science and Engineering: C*, *69*, 1103–1115. <https://doi.org/10.1016/J.MSEC.2016.08.015>
- Aw, M. S., Simovic, S., & Addai-mensah, J. (2011). Silica microcapsules from diatoms as new carrier for delivery of therapeutics P reliminary C ommunication. *Nanomedicine*, *6*(7), 1159–1173.
- Azhar, A., Abdelhady, H. M., Abdel Hafez, A., & Khodair, T. (2009). Batch Production of Polyhydroxybutyrate (PHB) by *Ralstonia Eutropha* and

- Alcaligenes Latus Using Bioreactor Different Culture Strategies. *Journal of Applied Sciences Research*, 5(5), 556–564.
- Babo, P. S., Santo, V. E., Gomes, M. E., & Reis, R. L. (2016). Development of an Injectable Calcium Phosphate/Hyaluronic Acid Microparticles System for Platelet Lysate Sustained Delivery Aiming Bone Regeneration. *Macromolecular Bioscience*, 16(11), 1662–1677. <https://doi.org/10.1002/mabi.201600141>
- Bacakova, L., Filova, E., Parizek, M., Ruml, T., & Svorcik, V. (2011). Modulation of cell adhesion, proliferation and differentiation on materials designed for body implants. *Biotechnology Advances*, 29(6), 739–767. <https://doi.org/10.1016/J.BIOTECHADV.2011.06.004>
- Bai, J., Dai, J., & Li, G. (2015). Electrospun composites of PHBV/pearl powder for bone repairing. *Progress in Natural Science: Materials International*, 25(4), 327–333. <https://doi.org/10.1016/J.PNSC.2015.07.004>
- Barbosa, O., Ortiz, C., Berenguer-Murcia, Á., Torres, R., Rodrigues, R. C., & Fernandez-Lafuente, R. (2014). Glutaraldehyde in bio-catalysts design: A useful crosslinker and a versatile tool in enzyme immobilization. In *RSC Advances* (Vol. 4, Issue 4, pp. 1583–1600). The Royal Society of Chemistry. <https://doi.org/10.1039/c3ra45991h>
- Bariana, M., Aw, M. S., Kurkuri, M., & Losic, D. (2013). Tuning drug loading and release properties of diatom silica microparticles by surface modifications. *International Journal of Pharmaceutics*, 443(1–2), 230–241. <https://doi.org/10.1016/j.ijpharm.2012.12.012>
- Basnett, P., & Roy, I. (2010). Microbial production of biodegradable polymers and their role in cardiac stent development. In A. Mendez-Vilas (Ed.), *Current research, technology and education topics in applied microbiology and microbial biotechnology* (pp. 1405–1415). Formatex Research Center. https://www.researchgate.net/publication/236888969_Microbial_production_o

f_biodegradable_polymers_and_their_role_in_cardiac_stent_development

- Bauer, S., Park, J., Mark, K. von der, & Schmuki, P. (2008). Improved attachment of mesenchymal stem cells on super-hydrophobic TiO₂ nanotubes. *Acta Biomaterialia*. <https://doi.org/10.1016/j.actbio.2008.04.004>
- Berezina, N. (2012). Enhancing the 3-hydroxyvalerate component in bioplastic PHBV production by *Cupriavidus necator*. *Biotechnology Journal*, 7(2), 304–309. <https://doi.org/10.1002/biot.201100191>
- Bharti, C., Gulati, N., Nagaich, U., & Pal, A. (2015). Mesoporous silica nanoparticles in target drug delivery system: A review. *International Journal of Pharmaceutical Investigation*, 5(3), 124–133. <https://doi.org/10.4103/2230-973X.160844>
- Bhattacharya, D., & Gupta, R. K. (2005). Nanotechnology and Potential of Microorganisms. *Critical Reviews in Biotechnology*, 25(4), 199–204. <https://doi.org/10.1080/07388550500361994>
- Bhattacharyya, A., Pramanik, A., Maji, S., Haldar, S., Mukhopadhyay, U., & Mukherjee, J. (2012). Utilization of vinasse for production of poly-3-(hydroxybutyrate-co-hydroxyvalerate) by *Haloferax mediterranei*. *AMB Express*, 2(1), 34. <https://doi.org/10.1186/2191-0855-2-34>
- Bianco, A., Calderone, M., & Cacciotti, I. (2013). Electrospun PHBV/PEO co-solution blends: Microstructure, thermal and mechanical properties. *Materials Science and Engineering C*, 33(3), 1067–1077. <https://doi.org/10.1016/j.msec.2012.11.030>
- Bismuto, A., Setaro, A., Maddalena, P., De Stefano, L., & De Stefano, M. (2008). Marine diatoms as optical chemical sensors: A time-resolved study. *Sensors and Actuators B*, 130(1), 396–399. <https://doi.org/10.1016/j.snb.2007.09.012>
- Blackwood, K. A., McKean, R., Canton, I., Freeman, C. O., Franklin, K. L., Cole, D., Brook, I., Farthing, P., Rimmer, S., Haycock, J. W., Ryan, A. J., & MacNeil,

- S. (2008). Development of biodegradable electrospun scaffolds for dermal replacement. *Biomaterials*, 29(21), 3091–3104. <https://doi.org/10.1016/j.biomaterials.2008.03.037>
- Bochicchio, B., Barbaro, K., De Bonis, A., Rau, J. V., & Pepe, A. (2020). Electrospun poly(d,l-lactide)/gelatin/glass-ceramics tricomponent nanofibrous scaffold for bone tissue engineering. *Journal of Biomedical Materials Research Part A*. <https://doi.org/10.1002/jbm.a.36882>
- Bonino, C. A., Krebs, M. D., Saquing, C. D., Jeong, S. I., Shearer, K. L., Alsberg, E., & Khan, S. A. (2011). Electrospinning alginate-based nanofibers: From blends to crosslinked low molecular weight alginate-only systems. *Carbohydrate Polymers*, 85(1), 111–119. <https://doi.org/10.1016/j.carbpol.2011.02.002>
- Bose, S., Roy, M., & Bandyopadhyay, A. (2012). Recent advances in bone tissue engineering scaffolds. *Trends in Biotechnology*, 30(10), 546–554. <https://doi.org/10.1016/j.tibtech.2012.07.005>
- Brunella, V., Jadhav, S. A., Miletto, I., Berlier, G., Ugazio, E., Sapino, S., & Scalpone, D. (2016). Hybrid drug carriers with temperature-controlled on-off release: A simple and reliable synthesis of PNIPAM-functionalized mesoporous silica nanoparticles. *Reactive and Functional Polymers*, 98, 31–37. <https://doi.org/10.1016/j.reactfunctpolym.2015.11.006>
- Burr, D. B. (2002). Targeted and nontargeted remodeling. In *Bone* (Vol. 30, Issue 1, pp. 2–4). Elsevier Inc. [https://doi.org/10.1016/S8756-3282\(01\)00619-6](https://doi.org/10.1016/S8756-3282(01)00619-6)
- Burr, David B. (2019). Bone Morphology and Organization. In *Basic and Applied Bone Biology* (Second Edi). Elsevier Inc. <https://doi.org/10.1016/B978-0-12-813259-3.00001-4>
- Butler, K. S., Durfee, P. N., Theron, C., Ashley, C. E., Carnes, E. C., & Brinker, C. J. (2016). Protocells: Modular Mesoporous Silica Nanoparticle-Supported Lipid Bilayers for Drug Delivery. *Small*, 12(16), 2173–2185.

<https://doi.org/10.1002/sml.201502119>

- Canton, I., Mckean, R., Charnley, M., Blackwood, K. A., Fiorica, C., Ryan, A. J., & MacNeil, S. (2010). Development of an Ibuprofen-releasing biodegradable PLA/PGA electrospun scaffold for tissue regeneration. *Biotechnology and Bioengineering*, *105*(2), 396–408. <https://doi.org/10.1002/bit.22530>
- Carlisle, E. M. (1972). Silicon: An Essential Element for the Chick. *Science*, *178*(4061), 619–621. <https://doi.org/10.1126/science.167.3916.279>
- Chen, C.-T., Chen, K.-I., Chiang, H.-H., Chen, Y.-K., & Cheng, K.-C. (2017). Improvement on Physical Properties of Pullulan Films by Novel Cross-Linking Strategy. *Journal of Food Science*, *82*(1), 108–117. <https://doi.org/10.1111/1750-3841.13577>
- Cheng, K.-C., Demirci, A., & Catchmark, J. M. (2011). Pullulan: biosynthesis, production, and applications. *Applied Microbiology and Biotechnology*, *92*(1), 29–44. <https://doi.org/10.1007/s00253-011-3477-y>
- Chiu, F.-Y., Chen, C.-M., Lin, C.-F. J., & Lo, W.-H. (2002). Cefuroxime-impregnated cement in primary total knee arthroplasty: a prospective, randomized study of three hundred and forty knees. *The Journal of Bone and Joint Surgery. American Volume*, *84*(5), 759–762. <http://www.ncbi.nlm.nih.gov/pubmed/12004017>
- Clarke, B. (2008). Normal bone anatomy and physiology. In *Clinical journal of the American Society of Nephrology: CJASN: Vol. 3 Suppl 3*. <https://doi.org/10.2215/CJN.04151206>
- Dalgic, A. D., Atila, D., Karatas, A., Tezcaner, A., & Keskin, D. (2019). Diatom shell incorporated PHBV/PCL-pullulan co-electrospun scaffold for bone tissue engineering. *Materials Science and Engineering: C*, *100*, 735–746. <https://doi.org/10.1016/J.MSEC.2019.03.046>
- De Stefano, L., Rotiroti, L., De Stefano, M., Lamberti, A., Lettieri, S., Setaro, A., &

- Maddalena, P. (2009). Marine diatoms as optical biosensors. *Biosensors and Bioelectronics*, 24(6), 1580–1584. <https://doi.org/10.1016/j.bios.2008.08.016>
- De Witte, T., Wagner, A. M., Fratila-Apachitei, L. E., Zadpoor, A. A., & Peppas, N. A. (2020). Immobilization of nanocarriers within a porous chitosan scaffold for the sustained delivery of growth factors in bone tissue engineering applications. *Journal of Biomedical Materials Research Part A*, jbm.a.36887. <https://doi.org/10.1002/jbm.a.36887>
- Del Gaudio, C., Ercolani, E., Nanni, F., & Bianco, A. (2011). Assessment of poly(ϵ -caprolactone)/poly(3-hydroxybutyrate-co-3-hydroxyvalerate) blends processed by solvent casting and electrospinning. *Materials Science and Engineering A*, 528(3), 1764–1772. <https://doi.org/10.1016/j.msea.2010.11.012>
- Delaissé, J. M., Andersen, T. L., Engsig, M. T., Henriksen, K., Troen, T., & Blavier, L. (2003). Matrix metalloproteinases (MMP) and cathepsin K contribute differently to osteoclastic activities. *Microscopy Research and Technique*, 61(6), 504–513. <https://doi.org/10.1002/jemt.10374>
- Dolatabadi, J. E. N., & de la Guardia, M. (2011). Applications of diatoms and silica nanotechnology in biosensing, drug and gene delivery, and formation of complex metal nanostructures. *Trends in Analytical Chemistry*, 30(9), 1538–1548. <https://doi.org/10.1016/j.trac.2011.04.015>
- ERIKSEN, E. F. (1986). Normal and Pathological Remodeling of Human Trabecular Bone: Three Dimensional Reconstruction of the Remodeling Sequence in Normals and in Metabolic Bone Disease*. *Endocrine Reviews*, 7(4), 379–408. <https://doi.org/10.1210/edrv-7-4-379>
- Farago, P. V., Raffin, R. P., Pohlmann, A. R., Guterres, S. S., & Zawadzki, S. F. (2008). Physicochemical characterization of a hydrophilic model drug-loaded PHBV microparticles obtained by the double emulsion/solvent evaporation technique. *Journal of the Brazilian Chemical Society*, 19(7), 1298–1305. <https://doi.org/10.1590/S0103-50532008000700011>

- Ferreira, L. M., Velasquez, A. de A., Schaffazick, S. R., & Cruz, L. (2015). Pullulan: an advantageous natural polysaccharide excipient to formulate tablets of alendronate-loaded microparticles. *Brazilian Journal of Pharmaceutical Sciences*, *51*(1), 27–33. <https://doi.org/10.1590/S1984-82502015000100003>
- Finn, A., Straughn, A., Meyer, M., & Chubb, J. (1987). Effect of dose and food on the bioavailability of ceforoxime axetil. *Biopharmaceutics & Drug Disposition*, *8*(6), 519–526. <http://www.ncbi.nlm.nih.gov/pubmed/3427209>
- Florencio-Silva, R., Rodrigues Da, G., Sasso, S., Sasso-Cerri, E., Simões, M. J., & Cerri, P. S. (2015). *Biology of Bone Tissue: Structure, Function, and Factors That Influence Bone Cells*. <https://doi.org/10.1155/2015/421746>
- Fong, H., Chun, I., & Reneker, D. H. (1999). Beaded nanofibers formed during electrospinning. *Polymer*, *40*(16), 4585–4592. [https://doi.org/10.1016/S0032-3861\(99\)00068-3](https://doi.org/10.1016/S0032-3861(99)00068-3)
- Frazer, J. (2016). *Beams Built of Diatom Boast Record-Setting Strength - Scientific American Blog Network*. <https://blogs.scientificamerican.com/artful-amoeba/beams-built-of-diatom-boast-record-setting-strength/>
- Fricain, J. C., Schlaubitz, S., Le Visage, C., Arnault, I., Derkaoui, S. M., Siadous, R., Catros, S., Lalande, C., Bareille, R., Renard, M., Fabre, T., Cornet, S., Durand, M., Léonard, A., Sahraoui, N., Letourneur, D., & Amédée, J. (2013). A nano-hydroxyapatite – Pullulan/dextran polysaccharide composite macroporous material for bone tissue engineering. *Biomaterials*, *34*(12), 2947–2959. <https://doi.org/10.1016/j.biomaterials.2013.01.049>
- Gao, C., Deng, Y., Feng, P., Mao, Z., Li, P., Yang, B., Deng, J., Cao, Y., Shuai, C., & Peng, S. (2014). Current progress in bioactive ceramic scaffolds for bone repair and regeneration. In *International Journal of Molecular Sciences* (Vol. 15, Issue 3, pp. 4714–4732). MDPI AG. <https://doi.org/10.3390/ijms15034714>
- Gong, T., Xie, J., Liao, J., Zhang, T., Lin, S., & Lin, Y. (2015). Nanomaterials and bone regeneration. In *Bone Research* (Vol. 3). Sichuan University.

<https://doi.org/10.1038/boneres.2015.29>

Guarino, V., Gentile, G., Sorrentino, L., & Ambrosio, L. (2002). Polycaprolactone: Synthesis, Properties, and Applications. In *Encyclopedia of Polymer Science and Technology* (4th ed., Vol. 15, pp. 1–36). John Wiley & Sons, Inc. <https://doi.org/10.1002/0471440264.pst658>

Gupta, P., Elkins, C., Long, T. E., & Wilkes, G. L. (2005). Electrospinning of linear homopolymers of poly(methyl methacrylate): Exploring relationships between fiber formation, viscosity, molecular weight and concentration in a good solvent. *Polymer*, *46*(13), 4799–4810. <https://doi.org/10.1016/j.polymer.2005.04.021>

Hench, L. L., Xynos, I. D., & Polak, J. M. (2004). Bioactive glasses for in situ tissue regeneration. In *Journal of Biomaterials Science, Polymer Edition* (Vol. 15, Issue 4, pp. 543–562). Taylor & Francis Group. <https://doi.org/10.1163/156856204323005352>

Henkel, J., Woodruff, M. A., Epari, D. R., Steck, R., Glatt, V., Dickinson, I. C., Choong, P. F. M., Schuetz, M. A., & Hutmacher, Di. W. (2013). Bone Regeneration Based on Tissue Engineering Conceptions-A 21st Century Perspective. In *Bone Research* (Vol. 1, pp. 216–248). Sichuan University. <https://doi.org/10.4248/BR201303002>

Hermanson, G. T. (2013). Homobifunctional Crosslinkers. In *Bioconjugate Techniques* (pp. 275–298). Elsevier. <https://doi.org/10.1016/b978-0-12-382239-0.00005-4>

Husain, O., Lau, W., Edirisinghe, M., & Parhizkar, M. (2016). Investigating the particle to fibre transition threshold during electrohydrodynamic atomization of a polymer solution. *Materials Science and Engineering C*, *65*, 240–250. <https://doi.org/10.1016/j.msec.2016.03.076>

Ikpeme, I. A., Ngim, N. E., & Ikpeme, A. (2010). Diagnosis and treatment of pyogenic bone infections. *African Health Sciences*, *10*(1), 82–88.

https://www.researchgate.net/publication/46111248_Diagnosis_and_treatment_of_pyogenic_bone_infections

- Islam, M. S., Akter, N., & Karim, M. R. (2010). Preparation of superhydrophobic membranes by electrospinning of fluorinated silane functionalized pullulan. *Colloids and Surfaces A: Physicochemical and Engineering Aspects*, 362(1–3), 117–120. <https://doi.org/10.1016/J.COLSURFA.2010.04.004>
- Jamali, A. A., Akbari, F., Ghorakhlou, M. M., de la Guardia, M., & Khosroushahi, A. Y. (2012). Applications of diatoms as potential microalgae in nanobiotechnology. *BioImpacts*, 2(2), 83–89. <https://doi.org/10.5681/bi.2012.012>
- Jugdaohsingh, R. (2007). Silicon and bone health. *The Journal of Nutrition, Health & Aging*, 11(2), 99–110. <http://www.ncbi.nlm.nih.gov/pubmed/17435952>
- Jugdaohsingh, R., Tucker, K. L., Qiao, N., Cupples, L. A., Kiel, D. P., & Powell, J. J. (2004). Dietary Silicon Intake Is Positively Associated With Bone Mineral Density in Men and Premenopausal Women of the Framingham Offspring Cohort. *Journal of Bone and Mineral Research*, 19(2), 297–307. <https://doi.org/10.1359/JBMR.0301225>
- Kalayci, V. E., Patra, P. K., Kim, Y. K., Ugbohue, S. C., & Warner, S. B. (2005). Charge consequences in electrospun polyacrylonitrile (PAN) nanofibers. *Polymer*, 46(18), 7191–7200. <https://doi.org/10.1016/j.polymer.2005.06.041>
- Karageorgiou, V., & Kaplan, D. (2005). Porosity of 3D biomaterial scaffolds and osteogenesis. *Biomaterials*, 26(27), 5474–5491. <https://doi.org/10.1016/J.BIOMATERIALS.2005.02.002>
- Khojasteh, A., Fahimipour, F., Eslaminejad, M. B., Jafarian, M., Jahangir, S., Bastami, F., Tahriri, M., Karkhaneh, A., & Tayebi, L. (2016). Development of PLGA-coated β -TCP scaffolds containing VEGF for bone tissue engineering. *Materials Science and Engineering C*, 69, 780–788. <https://doi.org/10.1016/j.msec.2016.07.011>

- Kim, C. H., Khil, M. S., Kim, H. Y., Lee, H. U., & Jahng, K. Y. (2006). An improved hydrophilicity via electrospinning for enhanced cell attachment and proliferation. *Journal of Biomedical Materials Research - Part B Applied Biomaterials*, 78(2), 283–290. <https://doi.org/10.1002/jbm.b.30484>
- Kim, E.-J., Bu, S.-Y., Sung, M.-K., & Choi, M.-K. (2013). Effects of Silicon on Osteoblast Activity and Bone Mineralization of MC3T3-E1 Cells. *Biological Trace Element Research*, 152(1), 105–112. <https://doi.org/10.1007/s12011-012-9593-4>
- Kim, M. S., & Kim, G. (2014). Three-dimensional electrospun polycaprolactone (PCL)/alginate hybrid composite scaffolds. *Carbohydrate Polymers*, 114, 213–221. <https://doi.org/10.1016/j.carbpol.2014.08.008>
- Kobayashi, S., Takahashi, H. E., Ito, A., Saito, N., Nawata, M., Horiuchi, H., Ohta, H., Iorio, R., Yamamoto, N., & Takaoka, K. (2003). Trabecular minimodeling in human iliac bone. *Bone*, 32(2), 163–169. [https://doi.org/10.1016/S8756-3282\(02\)00947-X](https://doi.org/10.1016/S8756-3282(02)00947-X)
- Köse, G. T., Korkusuz, F., Korkusuz, P., Purali, N., Ozkul, A., & Hasirci, V. (2003). Bone generation on PHBV matrices: an in vitro study. *Biomaterials*, 24(27), 4999–5007. <http://www.ncbi.nlm.nih.gov/pubmed/14559013>
- Kouhi, M., Fathi, M., Prabhakaran, M. P., Shamanian, M., & Ramakrishna, S. (2018). Poly L lysine-modified PHBV based nanofibrous scaffolds for bone cell mineralization and osteogenic differentiation. *Applied Surface Science*, 457, 616–625. <https://doi.org/10.1016/J.APSUSC.2018.06.239>
- Lack, S., Dulong, V., Le Cerf, D., Picton, L., Argillier, J. F., & Muller, G. (2004). Hydrogels based on pullulan crosslinked with sodium trimetaphosphate (STMP): Rheological study. *Polymer Bulletin*, 52(6), 429–436. <https://doi.org/10.1007/s00289-004-0299-4>
- Lalande, C., Miraux, S., Derkaoui, S. M., Mornet, S., Bareille, R., Fricain, J. C., Franconi, J. M., Le Visage, C., Letourneur, D., Amédée, J., & Bouzier-Sore, A.

- K. (2011). Magnetic resonance imaging tracking of human adipose derived stromal cells within three-dimensional scaffolds for bone tissue engineering. *European Cells & Materials*, 21, 341–354. <http://www.ncbi.nlm.nih.gov/pubmed/21484704>
- Landi, E., Celotti, G., Logroscino, G., & Tampieri, A. (2003). Carbonated hydroxyapatite as bone substitute. *Journal of the European Ceramic Society*, 23(15), 2931–2937. [https://doi.org/10.1016/S0955-2219\(03\)00304-2](https://doi.org/10.1016/S0955-2219(03)00304-2)
- Le, T. D. H., Liaudanskaya, V., Bonani, W., Migliaresi, C., & Motta, A. (2018a). Enhancing bioactive properties of silk fibroin with diatom particles for bone tissue engineering applications. *Journal of Tissue Engineering and Regenerative Medicine*, 12(1), 89–97. <https://doi.org/10.1002/term.2373>
- Le, T. D. H., Liaudanskaya, V., Bonani, W., Migliaresi, C., & Motta, A. (2018b). Enhancing bioactive properties of silk fibroin with diatom particles for bone tissue engineering applications. *Journal of Tissue Engineering and Regenerative Medicine*, 12(1), 89–97. <https://doi.org/10.1002/term.2373>
- Lee, K. H., Kim, H. Y., Khil, M. S., Ra, Y. M., & Lee, D. R. (2003). Characterization of nano-structured poly(ϵ -caprolactone) nonwoven mats via electrospinning. *Polymer*, 44(4), 1287–1294. [https://doi.org/10.1016/S0032-3861\(02\)00820-0](https://doi.org/10.1016/S0032-3861(02)00820-0)
- Li, H., & Chang, J. (2005). In vitro degradation of porous degradable and bioactive PHBV/wollastonite composite scaffolds. *Polymer Degradation and Stability*, 87(2), 301–307. <https://doi.org/10.1016/j.polymdegradstab.2004.09.001>
- Li, L., Gao, J., & Wang, Y. (2004). Evaluation of cyto-toxicity and corrosion behavior of alkali-heat-treated magnesium in simulated body fluid. *Surface and Coatings Technology*, 185(1), 92–98. <https://doi.org/10.1016/J.SURFCOAT.2004.01.004>
- Li, Xiang, Bian, F., Lin, J., & Zeng, Y. (2016). Effect of electric field on the morphology and mechanical properties of electrospun fibers. *RSC Advances*, 6(56), 50666–50672. <https://doi.org/10.1039/c6ra09635b>

- Li, Xiangjia, Yuan, Y., Liu, L., Leung, Y. S., Chen, Y., Guo, Y., Chai, Y., & Chen, Y. (2019). 3D printing of hydroxyapatite/tricalcium phosphate scaffold with hierarchical porous structure for bone regeneration. *Bio-Design and Manufacturing*, 1–15. <https://doi.org/10.1007/s42242-019-00056-5>
- Li, Y., Ma, X., Ju, J., Sun, X., Deng, N., Li, Z., Kang, W., & Cheng, B. (2018). Preparation and characterization of crosslinked electrospun pullulan nanofiber membrane as a potential for biomaterials. *The Journal of The Textile Institute*, 109(6), 750–756. <https://doi.org/10.1080/00405000.2017.1368107>
- Lim, Y.-M., Gwon, H.-J., Jeun, J. P., & Nho, Y.-C. (2010). We are IntechOpen , the world ' s leading publisher of Open Access books Built by scientists , for scientists TOP 1 % . In A. Kumar (Ed.), *Nanofibers* (p. 438). INTECH.
- Lin, T., Wang, H., Wang, H., & Wang, X. (2004). The charge effect of cationic surfactants on the elimination of fibre beads in the electrospinning of polystyrene. *Nanotechnology*, 15(9), 1375. <https://iopscience.iop.org/article/10.1088/0957-4484/15/9/044/meta>
- Liu, Y., Luo, D., & Wang, T. (2016). Hierarchical Structures of Bone and Bioinspired Bone Tissue Engineering. *Small*, 12(34), 4611–4632. <https://doi.org/10.1002/sml.201600626>
- Liu, Y. S., Ou, M. E., Liu, H., Gu, M., Lv, L. W., Fan, C., Chen, T., Zhao, X. H., Jin, C. Y., Zhang, X., Ding, Y., & Zhou, Y. S. (2014). The effect of simvastatin on chemotactic capability of SDF-1 α and the promotion of bone regeneration. *Biomaterials*, 35(15), 4489–4498. <https://doi.org/10.1016/j.biomaterials.2014.02.025>
- Logoluso, N., Drago, L., Gallazzi, E., George, D., Morelli, I., & Romanò, C. (2016). Calcium-Based, Antibiotic-Loaded Bone Substitute as an Implant Coating: A Pilot Clinical Study. *Journal of Bone and Joint Infection*, 1, 59–64. <https://doi.org/10.7150/jbji.17586>
- López-Álvarez, M., Solla, E. L., González, P., Serra, J., León, B., Marques, A. P., &

- Reis, R. L. (2009). Silicon-hydroxyapatite bioactive coatings (Si-HA) from diatomaceous earth and silica. Study of adhesion and proliferation of osteoblast-like cells. *Journal of Materials Science: Materials in Medicine*, 20(5), 1131–1136. <https://doi.org/10.1007/s10856-008-3658-0>
- Lü, L.-X., Wang, Y.-Y., Mao, X., Xiao, Z.-D., & Huang, N.-P. (2012). The effects of PHBV electrospun fibers with different diameters and orientations on growth behavior of bone-marrow-derived mesenchymal stem cells. *Biomedical Materials*, 7(1), 015002. <https://doi.org/10.1088/1748-6041/7/1/015002>
- Lu, Q., Han, J., Zhou, L., Zhou, J., & Xiang, H. (2008). Genetic and biochemical characterization of the poly(3-hydroxybutyrate-co- 3-hydroxyvalerate) synthase in *Haloferax mediterranei*. *Journal of Bacteriology*, 190(12), 4173–4180. <https://doi.org/10.1128/JB.00134-08>
- Luo, C. J., Stride, E., & Edirisinghe, M. (2012). Mapping the influence of solubility and dielectric constant on electrospinning polycaprolactone solutions. *Macromolecules*, 45(11), 4669–4680. <https://doi.org/10.1021/ma300656u>
- Malaquias Barboza, F., Moreira Machado, W., Renato Olchanheski Junior, L., Padilha de Paula, J., Faria Zawadzki, S., Fernandes, D., & Vitor Farago, P. (2014). PCL/PHBV Microparticles as Innovative Carriers for Oral Controlled Release of Manidipine Dihydrochloride. *The Scientific World Journal*. <https://doi.org/10.1155/2014/268107>
- Martin, V., & Bettencourt, A. (2018). Bone regeneration: Biomaterials as local delivery systems with improved osteoinductive properties. *Materials Science and Engineering C*, 82, 363–371. <https://doi.org/10.1016/j.msec.2017.04.038>
- Matassi, F., Nistri, L., Paez, D. C., & Innocenti, M. (2011). New biomaterials for bone regeneration. In *Clinical Cases in Mineral and Bone Metabolism* (Vol. 8, Issue 1, pp. 21–24).
- Maximov, P. Y., Lee, T. M., & Jordan, V. C. (2013). The discovery and development of selective estrogen receptor modulators (SERMs) for clinical practice.

- Current Clinical Pharmacology*, 8(2), 135–155.
<http://www.ncbi.nlm.nih.gov/pubmed/23062036>
- Meijer, G. J., de Bruijn, J. D., Koole, R., & van Blitterswijk, C. A. (2007). Cell-Based Bone Tissue Engineering. *PLoS Medicine*, 4(2), 260–264.
<https://doi.org/10.1371/journal.pmed.0040009>
- Meng, W., Kim, S.-Y., Yuan, J., Kim, J. C., Kwon, O. H., Kawazoe, N., Chen, G., Ito, Y., & Kang, I.-K. (2007). Electrospun PHBV/collagen composite nanofibrous scaffolds for tissue engineering. *Journal of Biomaterials Science, Polymer Edition*, 18(1), 81–94. <https://doi.org/10.1163/156856207779146114>
- Mishra, B., Vuppu, S., & Rath, K. (2011). The role of microbial pullulan, a biopolymer in pharmaceutical approaches: A review. *Journal of Applied Pharmaceutical Science*, 1(6), 45–50.
https://www.japsonline.com/admin/php/uploads/122_pdf.pdf
- Montalbano, G., Molino, G., Fiorilli, S., & Vitale-Brovarone, C. (2020). Synthesis and incorporation of rod-like nano-hydroxyapatite into type I collagen matrix: A hybrid formulation for 3D printing of bone scaffolds. *Journal of the European Ceramic Society*.
<https://doi.org/10.1016/j.jeurceramsoc.2020.02.018>
- Motamedian, S. R. (2015). Smart scaffolds in bone tissue engineering: A systematic review of literature. *World Journal of Stem Cells*, 7(3), 657.
<https://doi.org/10.4252/wjsc.v7.i3.657>
- Muhammadi, Shabina, Afzal, M., & Hameed, S. (2015). Bacterial polyhydroxyalkanoates-eco-friendly next generation plastic: Production, biocompatibility, biodegradation, physical properties and applications. *Green Chemistry Letters and Reviews*, 8(3–4), 56–77.
<https://doi.org/10.1080/17518253.2015.1109715>
- Muzzarelli, R. A. A. (2011). Chitosan composites with inorganics, morphogenetic proteins and stem cells, for bone regeneration. *Carbohydrate Polymers*, 83(4),

1433–1445. <https://doi.org/10.1016/J.CARBPOL.2010.10.044>

- Nair, M. B., Baranwal, G., Vijayan, P., Keyan, K. S., & Jayakumar, R. (2015). Composite hydrogel of chitosan-poly(hydroxybutyrate-co-valerate) with chondroitin sulfate nanoparticles for nucleus pulposus tissue engineering. *Colloids and Surfaces B: Biointerfaces*, *136*, 84–92. <https://doi.org/10.1016/j.colsurfb.2015.08.026>
- Nandi, S. K., Kundu, B., Ghosh, S. K., Mandal, T. K., Datta, S., De, D. K., & Basu, D. (2009). Cefuroxime-impregnated calcium phosphates as an implantable delivery system in experimental osteomyelitis. *Ceramics International*, *35*(4), 1367–1376. <https://doi.org/10.1016/J.CERAMINT.2008.07.022>
- Nandi, S. K., Kundu, B., Mukherjee, P., Mandal, T. K., Datta, S., De, D. K., & Basu, D. (2009). In vitro and in vivo release of cefuroxime axetil from bioactive glass as an implantable delivery system in experimental osteomyelitis. *Ceramics International*, *35*(8), 3207–3216. <https://doi.org/10.1016/J.CERAMINT.2009.05.005>
- Nassif, N., & Livage, J. (2011). From diatoms to silica-based biohybrids. *Chemical Society Reviews*, *40*(2), 849–859. <https://doi.org/10.1039/c0cs00122h>
- Nazemi, K., Moztafzadeh, F., Jalali, N., Asgari, S., & Mozafari, M. (2014). Synthesis and Characterization of Poly(lactic-co-glycolic) Acid Nanoparticles-Loaded Chitosan/Bioactive Glass Scaffolds as a Localized Delivery System in the Bone Defects. *BioMed Research International*, *2014*, 1–9. <https://doi.org/10.1155/2014/898930>
- Nezarati, R. M., Eifert, M. B., & Cosgriff-Hernandez, E. (2013). Effects of humidity and solution viscosity on electrospun fiber morphology. *Tissue Engineering - Part C: Methods*, *19*(10), 810–819. <https://doi.org/10.1089/ten.tec.2012.0671>
- Nielsen, F. H., & Poellot, R. (2004). Dietary silicon affects bone turnover differently in ovariectomized and sham-operated growing rats. *The Journal of Trace Elements in Experimental Medicine*, *17*(3), 137–149.

<https://doi.org/10.1002/jtra.20004>

- Nitschke, M., Costa, S. G. V. A. O., & Contiero, J. (2011). Rhamnolipids and PHAs: Recent reports on *Pseudomonas*-derived molecules of increasing industrial interest. In *Process Biochemistry* (Vol. 46, Issue 3, pp. 621–630). Elsevier. <https://doi.org/10.1016/j.procbio.2010.12.012>
- O'Brien, F. J. (2011). Biomaterials & scaffolds for tissue engineering. In *Materials Today* (Vol. 14, Issue 3, pp. 88–95). Elsevier B.V. [https://doi.org/10.1016/S1369-7021\(11\)70058-X](https://doi.org/10.1016/S1369-7021(11)70058-X)
- Parfitt, A. M. (2002). Targeted and nontargeted bone remodeling: Relationship to basic multicellular unit origination and progression. *Bone*, 30(1), 5–7. [https://doi.org/10.1016/S8756-3282\(01\)00642-1](https://doi.org/10.1016/S8756-3282(01)00642-1)
- Paşcu, E. I., Stokes, J., & McGuinness, G. B. (2013). Electrospun composites of PHBV, silk fibroin and nano-hydroxyapatite for bone tissue engineering. *Materials Science and Engineering C*, 33(8), 4905–4916. <https://doi.org/10.1016/j.msec.2013.08.012>
- Patrício, T., Domingos, M., Gloria, A., & Bártolo, P. (2013). Characterisation of PCL and PCL/PLA scaffolds for tissue engineering. *Procedia CIRP*, 5, 110–114. <https://doi.org/10.1016/j.procir.2013.01.022>
- Porter, A. E., Patel, N., Skepper, J. N., Best, S. M., & Bonfield, W. (2004). Effect of sintered silicate-substituted hydroxyapatite on remodelling processes at the bone-implant interface. *Biomaterials*, 25(16), 3303–3314. <https://doi.org/10.1016/j.biomaterials.2003.10.006>
- Porter, J. R., Ruckh, T. T., & Popat, K. C. (2009). Bone tissue engineering: A review in bone biomimetics and drug delivery strategies. *Biotechnology Progress*, NA-NA. <https://doi.org/10.1002/btpr.246>
- Puppi, D., Dinucci, D., Bartoli, C., Mota, C., Migone, C., Dini, F., Barsotti, G., Carlucci, F., & Chiellini, F. (2011). Development of 3D wet-spun polymeric

- scaffolds loaded with antimicrobial agents for bone engineering. *Journal of Bioactive and Compatible Polymers*, 26(5), 478–492. <https://doi.org/10.1177/0883911511415918>
- Rambo, C. R., Costa, C. M., Carminatti, C. A., Recouvreux, D. O. S., D'Acampora, A. J., & Porto, L. M. (2012). Osteointegration of poly-(3-hydroxybutyrate-co-3-hydroxyvalerate) scaffolds incorporated with violacein. *Materials Science and Engineering C*, 32(2), 385–389. <https://doi.org/10.1016/j.msec.2011.10.016>
- Rașoga, O., Sima, L., Chirițoiu, M., Popescu-Pelin, G., Fufă, O., Grumezescu, V., Socol, M., Stănculescu, A., Zgură, I., & Socol, G. (2017). Biocomposite coatings based on Poly(3-hydroxybutyrate-co-3-hydroxyvalerate)/calcium phosphates obtained by MAPLE for bone tissue engineering. *Applied Surface Science*, 417, 204–212. <https://doi.org/10.1016/j.apsusc.2017.01.205>
- Raza, Z. A., Abid, S., & Banat, I. M. (2018). Polyhydroxyalkanoates: Characteristics, production, recent developments and applications. In *International Biodeterioration and Biodegradation* (Vol. 126, pp. 45–56). Elsevier Ltd. <https://doi.org/10.1016/j.ibiod.2017.10.001>
- Reddy, S. V. (2004). Regulatory mechanisms operative in osteoclasts. In *Critical Reviews in Eukaryotic Gene Expression* (Vol. 14, Issue 4, pp. 255–270). <https://doi.org/10.1615/CritRevEukaryotGeneExpr.v14.i4.20>
- Rehm, B. H. A. (2010). Bacterial polymers: biosynthesis, modifications and applications. *Nature Reviews Microbiology*, 8(8), 578–592. <https://doi.org/10.1038/nrmicro2354>
- Roodman, G. D. (1999). Cell biology of the osteoclast. In *Experimental Hematology* (Vol. 27, Issue 8, pp. 1229–1241). [https://doi.org/10.1016/S0301-472X\(99\)00061-2](https://doi.org/10.1016/S0301-472X(99)00061-2)
- Roseti, L., Parisi, V., Petretta, M., Cavallo, C., Desando, G., Bartolotti, I., & Grigolo, B. (2017). Scaffolds for Bone Tissue Engineering: State of the art and new

- perspectives. In *Materials Science and Engineering C* (Vol. 78, pp. 1246–1262). Elsevier Ltd. <https://doi.org/10.1016/j.msec.2017.05.017>
- Ross, G., Ross, S., & Tighe, B. J. (2017). Bioplastics: New Routes, New Products. In M. Gilbert (Ed.), *Brydson's Plastics Materials* (8th ed., pp. 631–652). Elsevier Ltd. <https://doi.org/10.1016/B978-0-323-35824-8.00023-2>
- Sabir, M. I., Xu, X., & Li, L. (2009). A review on biodegradable polymeric materials for bone tissue engineering applications. *Journal of Materials Science*, 44(21), 5713–5724. <https://doi.org/10.1007/s10853-009-3770-7>
- Sajesh, K. M., Kiran, K., Nair, S. V., & Jayakumar, R. (2016). Sequential layer-by-layer electrospinning of nano SrCO₃/PRP loaded PHBV fibrous scaffold for bone tissue engineering. *Composites Part B: Engineering*, 99, 445–452. <https://doi.org/10.1016/J.COMPOSITESB.2016.06.026>
- Saldaña, L., Barranco, V., García-Alonso, M. C., Vallés, G., Escudero, M. L., Munuera, L., & Vilaboa, N. (2006). Concentration-dependent effects of titanium and aluminium ions released from thermally oxidized Ti6Al4V alloy on human osteoblasts. *Journal of Biomedical Materials Research Part A*, 77(2), 220–229. <https://doi.org/10.1002/jbm.a.30599>
- Samorezov, J. E., & Alsberga, E. (2015). Spatial regulation of controlled bioactive factor delivery for bone tissue engineering. *Advanced Drug Delivery Reviews*, 84, 45–67. <https://doi.org/10.1007/s10741-014-9462-7>.Natural
- Schärftl, W. (2007). *Light Scattering from Polymer Solutions and Nanoparticle Dispersions*. Springer Science & Business Media. https://books.google.com.tr/books?hl=tr&lr=&id=JBHyVdlwuuUC&oi=fnd&pg=PA1&ots=Tw6Avju8Mc&sig=I8NX1riu1hVn0SOoz3HHslK1p-s&redir_esc=y#v=onepage&q&f=false
- Schemitsch, E. H. (2017). Size Matters. *Journal of Orthopaedic Trauma*, 31, S20–S22. <https://doi.org/10.1097/BOT.0000000000000978>

- Schwarz, K., & Milne, D. B. (1972). Growth-promoting effects of silicon in rats. *Nature*, 239(5371), 333–334. <https://doi.org/10.1038/239333a0>
- Scott, L. J., Ormrod, D., & Goa, K. L. (2001). Cefuroxime Axetil. *Drugs*, 61(10), 1455–1500. <https://doi.org/10.2165/00003495-200161100-00008>
- Seaborn, C. D., & Nielsen, F. H. (2002). Silicon deprivation and arginine and cystine supplementation affect bone collagen and bone and plasma trace mineral concentrations in rats. *The Journal of Trace Elements in Experimental Medicine*, 15(3), 113–122. <https://doi.org/10.1002/jtra.10011>
- Shaheen, M. E., Ghazy, A. R., Kenawy, E. R., & El-Mekawy, F. (2018). Application of laser light scattering to the determination of molecular weight, second virial coefficient, and radius of gyration of chitosan. *Polymer*, 158, 18–24. <https://doi.org/10.1016/j.polymer.2018.10.044>
- Shi, L., Le Visage, C., & Chew, S. Y. (2011). Long-Term Stabilization of Polysaccharide Electrospun Fibres by In Situ Cross-Linking. *Journal of Biomaterials Science, Polymer Edition*, 22(11), 1459–1472. <https://doi.org/10.1163/092050610X512108>
- Shishatskaya, E. I., & Volova, T. G. (2004). A comparative investigation of biodegradable polyhydroxyalkanoate films as matrices for in vitro cell cultures. *Journal of Materials Science: Materials in Medicine*, 15(8), 915–923. <https://doi.org/10.1023/B:JMSM.0000036280.98763.c1>
- Shuai, C., Zan, J., Yang, Y., Peng, S., Yang, W., Qi, F., Shen, L., & Tian, Z. (2020). Surface modification enhances interfacial bonding in PLLA/MgO bone scaffold. *Materials Science and Engineering C*, 108. <https://doi.org/10.1016/j.msec.2019.110486>
- Silver, I. A., Murrills, R. J., & Etherington, D. J. (1988). Microelectrode studies on the acid microenvironment beneath adherent macrophages and osteoclasts. *Experimental Cell Research*, 175(2), 266–276. [https://doi.org/10.1016/0014-4827\(88\)90191-7](https://doi.org/10.1016/0014-4827(88)90191-7)

- Simovic, S., Ghouchi-Eskandar, N., Moom Sinn, A., Losic, D., & Prestidge, C. A. (2011). Silica Materials in Drug Delivery Applications. *Current Drug Discovery Technologies*, 8(3), 250–268.
- Sionkowska, A. (2011). Current research on the blends of natural and synthetic polymers as new biomaterials: Review. *Progress in Polymer Science*, 36(9), 1254–1276. <https://doi.org/10.1016/J.PROGPOLYMSCI.2011.05.003>
- Sombatmankhong, K., Sanchavanakit, N., Pavasant, P., & Supaphol, P. (2007). Bone scaffolds from electrospun fiber mats of poly(3-hydroxybutyrate), poly(3-hydroxybutyrate-co-3-hydroxyvalerate) and their blend. *Polymer*, 48(5), 1419–1427. <https://doi.org/10.1016/J.POLYMER.2007.01.014>
- Song, H. H., Yoo, M. K., Moon, H. S., Choi, Y. J., Lee, H. C., & Cho, C. S. (2007). A Novel Polycaprolactone/Hydroxyapatite Scaffold for Bone Tissue Engineering. *Key Engineering Materials*, 342–343, 265–268. <https://doi.org/10.4028/www.scientific.net/KEM.342-343.265>
- Song, M., Huo, H., Cao, Z., Han, Y., & Gao, L. (2017). Aluminum Trichloride Inhibits the Rat Osteoblasts Mineralization In Vitro. *Biological Trace Element Research*, 175(1), 186–193. <https://doi.org/10.1007/s12011-016-0761-9>
- Soundrapandian, C., Basu, D., Sa, B., & Datta, S. (2011). Local drug delivery system for the treatment of osteomyelitis: *In vitro* evaluation. *Drug Development and Industrial Pharmacy*, 37(5), 538–546. <https://doi.org/10.3109/03639045.2010.528427>
- Sruti, J., Patra, C., Swain, S., Beg, S., Palatasingh, H., Dinda, S., & Rao, M. E. (2013). Improvement in dissolution rate of cefuroxime axetil by using poloxamer 188 and Neusilin US2. *Indian Journal of Pharmaceutical Sciences*, 75(1), 67–75. <https://doi.org/10.4103/0250-474X.113551>
- Stewart, S., Bryant, S. J., Ahn, J., & Hankenson, K. D. (2015). Bone Regeneration. In *Translational Regenerative Medicine* (pp. 313–333). Elsevier Inc. <https://doi.org/10.1016/B978-0-12-410396-2.00024-4>

- Stijnman, A. C., Bodnar, I., & Hans Tromp, R. (2011). Electrospinning of food-grade polysaccharides. *Food Hydrocolloids*, 25(5), 1393–1398. <https://doi.org/10.1016/J.FOODHYD.2011.01.005>
- Sultana, Najma, & Arayne, A. M. S. (2002). IN VITRO ACTIVITY OF CEFAZOLINE AND CEFUROXIME IN PRESENCE OF ESSENTIAL AND TRACE ELEMENTS. *Pakistan Journal of Pharmaceutical Sciences*, 15(2), 41–50.
- Sultana, Nargis, Akter, T., & Begum, S. (2012). Population Studies of Tree Hole Breeding Aedes Species (Diptera: Culicidae) in Dhaka University Campus and its Adjacent Suhrawardi Park, Dhaka City, Bangladesh. *Bangladesh Journal of Zoology*, 40(1), 1–11. <https://doi.org/10.3329/bjz.v40i1.12887>
- Sultana, Naznin, & Khan, T. H. (2012). In Vitro Degradation of PHBV Scaffolds and nHA/PHBV Composite Scaffolds Containing Hydroxyapatite Nanoparticles for Bone Tissue Engineering. *Journal of Nanomaterials*, 2012, 12. <https://doi.org/10.1155/2012/190950>
- Suroy, M., Moriceau, B., Boutorh, J., & Goutx, M. (2014). Fatty acids associated with the frustules of diatoms and their fate during degradation-A case study in *Thalassiosira weissflogii*. *Deep-Sea Research Part I: Oceanographic Research Papers*. <https://doi.org/10.1016/j.dsr.2014.01.001>
- Suwantong, O., Waleetorncheepsawat, S., Sanchavanakit, N., Pavasant, P., Cheepsunthorn, P., Bunaprasert, T., & Supaphol, P. (2007). In vitro biocompatibility of electrospun poly(3-hydroxybutyrate) and poly(3-hydroxybutyrate-co-3-hydroxyvalerate) fiber mats. *International Journal of Biological Macromolecules*, 40(3), 217–223. <https://doi.org/10.1016/J.IJBIOMAC.2006.07.006>
- Taepucharoen, K., Tarawat, S., Puangcharoen, M., Incharoensakdi, A., & Monshupanee, T. (2017). Production of poly(3-hydroxybutyrate-co-3-hydroxyvalerate) under photoautotrophy and heterotrophy by non-

- heterocystous N₂-fixing cyanobacterium. *Bioresource Technology*, 239, 523–527. <https://doi.org/10.1016/j.biortech.2017.05.029>
- Tamburaci, S., & Tihminlioglu, F. (2017). Diatomite reinforced chitosan composite membrane as potential scaffold for guided bone regeneration. *Materials Science and Engineering: C*, 80, 222–231. <https://doi.org/10.1016/j.msec.2017.05.069>
- Tamburaci, S., & Tihminlioglu, F. (2018). Biosilica incorporated 3D porous scaffolds for bone tissue engineering applications. *Materials Science and Engineering: C*, 91, 274–291. <https://doi.org/10.1016/J.MSEC.2018.05.040>
- Tao, Jian, Song, C., Cao, M., Hu, D., Liu, L., Liu, N., & Wang, S. (2009). Thermal properties and degradability of poly(propylene carbonate)/poly(β -hydroxybutyrate-co- β -hydroxyvalerate) (PPC/PHBV) blends. *Polymer Degradation and Stability*, 94(4), 575–583. <https://doi.org/10.1016/j.polymdegradstab.2009.01.017>
- Tao, Jing, & Shivkumar, S. (2007). Molecular weight dependent structural regimes during the electrospinning of PVA. *Materials Letters*, 61(11–12), 2325–2328. <https://doi.org/10.1016/j.matlet.2006.09.004>
- Tenenbaum, H. C., Shelemay, A., Girard, B., Zohar, R., & Fritz, P. C. (2002). Bisphosphonates and Periodontics: Potential Applications for Regulation of Bone Mass in the Periodontium and Other Therapeutic/ Diagnostic Uses. *Journal of Periodontology*, 73(7), 813–822. <https://doi.org/10.1902/jop.2002.73.7.813>
- Thavornnyutikarn, B., Chantarapanich, N., Sitthiseriratip, K., Thouas, G. A., & Chen, Q. (2014). Bone tissue engineering scaffolding: computer-aided scaffolding techniques. *Progress in Biomaterials*, 3(2–4), 61–102. <https://doi.org/10.1007/s40204-014-0026-7>
- Truesdell, S. L., & Saunders, M. M. (2019). Bone remodeling platforms: Understanding the need for multicellular lab-on-a-chip systems and predictive agent-based models Regulation of EGFR signaling in *Drosophila* development

View project Bone remodeling platforms: Understanding the need for multicellular lab-on-a-chip systems and predictive agent-based models. *Mathematical Biosciences and Engineering*, 17(2), 1233–1252. <https://doi.org/10.3934/mbe.2020063>

Tsukimura, N., Yamada, M., Aita, H., Hori, N., Yoshino, F., Lee, M. C., Kimoto, K., Jewett, A., & Ogawa, T. (2009). N-acetyl cysteine (NAC)-mediated detoxification and functionalization of poly(methyl methacrylate) bone cement. *Biomaterials*, 30, 3378–3389. <https://doi.org/10.1002/9781444314724>

Tuzlakoglu, K., Bolgen, N., Salgado, A. J., Gomes, M. E., Piskin, E., & Reis, R. L. (2005). Nano- and micro-fiber combined scaffolds: A new architecture for bone tissue engineering. *Journal of Materials Science: Materials in Medicine*, 16(12), 1099–1104. <https://doi.org/10.1007/s10856-005-4713-8>

Uçkay, I., Hoffmeyer, P., Lew, D., & Pittet, D. (2013). Prevention of surgical site infections in orthopaedic surgery and bone trauma: state-of-the-art update. *Journal of Hospital Infection*, 84(1), 5–12. <https://doi.org/10.1016/J.JHIN.2012.12.014>

Umemura, K., Xing, L., Mayama, S., & Gad, M. (2007). Controlled nanoporous structures of a marine diatom. *Journal of Nanoscience and Nanotechnology*. <https://doi.org/10.1166/jnn.2007.633>

Uppal, R., & Ramaswamy, G. N. (2011). Cellulose Submicron Fibers. *Journal of Engineered Fibers and Fabrics*, 6(4), 39–45. <https://doi.org/10.1177/155892501100600406>

van Vugt, T. A. G., Walraven, J. M. B., Geurts, J. A. P., & Arts, J. J. C. (2018). Antibiotic-Loaded Collagen Sponges in Clinical Treatment of Chronic Osteomyelitis. *The Journal of Bone and Joint Surgery*, 100(24), 2153–2161. <https://doi.org/10.2106/JBJS.17.01140>

Völker, A. C., Vaccaro, A., & Cardinaux, F. (2016). Advanced light scattering techniques. In *Lecture Notes in Physics* (Vol. 917, pp. 389–412). Springer

Verlag. https://doi.org/10.1007/978-3-319-24502-7_11

- Wang, B.-J., Zhang, Y.-J., Zhang, J.-Q., Gou, Q.-T., Wang, Z.-B., Chen, P., & Gu, Q. (2013). Crystallization behavior, thermal and mechanical properties of phbv/graphene nanosheet composites. *Chinese Journal of Polymer Science*, *31*(4), 670–678. <https://doi.org/10.1007/s10118-013-1248-1>
- Wang, Yi, Cui, W., Zhao, X., Wen, S., Sun, Y., Han, J., & Zhang, H. (2019). Bone remodeling-inspired dual delivery electrospun nanofibers for promoting bone regeneration. *Nanoscale*, *11*(1), 60–71. <https://doi.org/10.1039/c8nr07329e>
- Wang, Yuanpeng, Chen, R., Cai, J. Y., Liu, Z., Zheng, Y., Wang, H., Li, Q., & He, N. (2013). Biosynthesis and Thermal Properties of PHBV Produced from Levulinic Acid by *Ralstonia eutropha*. *PLoS ONE*, *8*(4), e60318. <https://doi.org/10.1371/journal.pone.0060318>
- Wilkinson, F. (2015). *The Isolation and Estimation of the Poly- β -hydroxy- butyrate Inclusions of. 1958*, 198–209.
- Xiao, Q., & Lim, L.-T. (2018). Pullulan-alginate fibers produced using free surface electrospinning. *International Journal of Biological Macromolecules*, *112*, 809–817. <https://doi.org/10.1016/J.IJBIOMAC.2018.02.005>
- Xue, J., Wu, T., Dai, Y., & Xia, Y. (2019). Electrospinning and electrospun nanofibers: Methods, materials, and applications. *Chemical Reviews*, *119*(8), 5298–5415. <https://doi.org/10.1021/acs.chemrev.8b00593>
- Yang, Y., Zan, J., Yang, W., Qi, F., He, C., Huang, S., Peng, S., & Shuai, C. (2020). Metal organic frameworks as a compatible reinforcement in a biopolymer bone scaffold. *Materials Chemistry Frontiers*. <https://doi.org/10.1039/C9QM00772E>
- Yao, Q., Cosme, J. G. L., Xu, T., Miszuk, J. M., Picciani, P. H. S., Fong, H., & Sun, H. (2017). Three dimensional electrospun PCL/PLA blend nanofibrous scaffolds with significantly improved stem cells osteogenic differentiation and

- cranial bone formation. *Biomaterials*, *115*, 115–127.
<https://doi.org/10.1016/j.biomaterials.2016.11.018>
- Yaprakci, V., Erdemli, O., Kayabolen, A., Tezcaner, A., Bozkurt, F., & Keskin, D. (2013). *In vitro / in vivo* comparison of cefuroxime release from poly(ϵ -caprolactone)-calcium sulfate implants for osteomyelitis treatment. *Biotechnology and Applied Biochemistry*, *60*(6), 603–616.
<https://doi.org/10.1002/bab.1118>
- Yokoyama, Y., Hattori, S., Yoshikawa, C., Yasuda, Y., Koyama, H., Takato, T., & Kobayashi, H. (2009). Novel wet electrospinning system for fabrication of spongiform nanofiber 3-dimensional fabric. *Materials Letters*, *63*(9–10), 754–756. <https://doi.org/10.1016/j.matlet.2008.12.042>
- Yoshimoto, H., Shin, Y. M., Terai, H., & Vacanti, J. P. (2003). A biodegradable nanofiber scaffold by electrospinning and its potential for bone tissue engineering. *Biomaterials*, *24*, 2077–2082. [https://doi.org/10.1016/S0142-9612\(02\)00635-X](https://doi.org/10.1016/S0142-9612(02)00635-X)
- Yuan, Y., Choi, K., Choi, S. O., & Kim, J. (2018). Early stage release control of an anticancer drug by drug-polymer miscibility in a hydrophobic fiber-based drug delivery system. *RSC Advances*, *8*(35), 19791–19803.
<https://doi.org/10.1039/c8ra01467a>
- Zamani, Y., Amoabediny, G., Mohammadi, J., Seddiqi, H., Helder, M. N., Zandieh-Doulabi, B., Klein-Nulend, J., & Koolstra, J. H. (2020). 3D-printed poly(ϵ -caprolactone) scaffold with gradient mechanical properties according to force distribution in the mandible for mandibular bone tissue engineering. *Journal of the Mechanical Behavior of Biomedical Materials*, *104*, 103638.
<https://doi.org/10.1016/j.jmbbm.2020.103638>
- Zhang, H., Shahbazi, M. A., Mäkilä, E. M., da Silva, T. H., Reis, R. L., Salonen, J. J., Hirvonen, J. T., & Santos, H. A. (2013). Diatom silica microparticles for sustained release and permeation enhancement following oral delivery of

- prednisone and mesalamine. *Biomaterials*, 34(36), 9210–9219. <https://doi.org/10.1016/j.biomaterials.2013.08.035>
- Zhang, L., Yan, J., Yin, Z., Tang, C., Guo, Y., Li, D., Wei, B., Xu, Y., Gu, Q., & Wang, L. (2014). Electrospun vancomycin-loaded coating on titanium implants for the prevention of implant-associated infections. *International Journal of Nanomedicine*, 3027–3036. <https://doi.org/10.2147/IJN.S63991>
- Zhang, Xiang, Yang, H., Li, S., Qin, G., & Yang, L. (2018). Natural diatomite particles: Size-, dose- and shape- dependent cytotoxicity and reinforcing effect on injectable bone cement. *Journal of Materials Science & Technology*, 34(6), 1044–1053. <https://doi.org/10.1016/J.JMST.2017.04.020>
- Zhang, Xihe, Zhou, J., Ying, H., Zhou, Y., Lai, J., & Chen, J. (2020). Glycogen as a Cross-Linking Agent of Collagen and Nanohydroxyapatite To Form Hydrogels for bMSC Differentiation. *ACS Sustainable Chemistry & Engineering*, 8(4), 2106–2114. <https://doi.org/10.1021/acssuschemeng.9b07051>
- Zou, P., Liu, H., Li, Y., Huang, J., & Dai, Y. (2016). Surface dextran modified electrospun poly (3-hydroxybutyrate-co-3-hydroxyvalerate) (PHBV) fibrous scaffold promotes the proliferation of bone marrow-derived mesenchymal stem cells. *Materials Letters*, 179, 109–113. <https://doi.org/10.1016/J.MATLET.2016.04.189>
- Zuo, W., Zhu, M., Yang, W., Yu, H., Chen, Y., & Zhang, Y. (2005). Experimental study on relationship between jet instability and formation of beaded fibers during electrospinning. *Polymer Engineering & Science*, 45(5), 704–709. <https://doi.org/10.1002/pen.20304>

APPENDICES

A. Appendix A

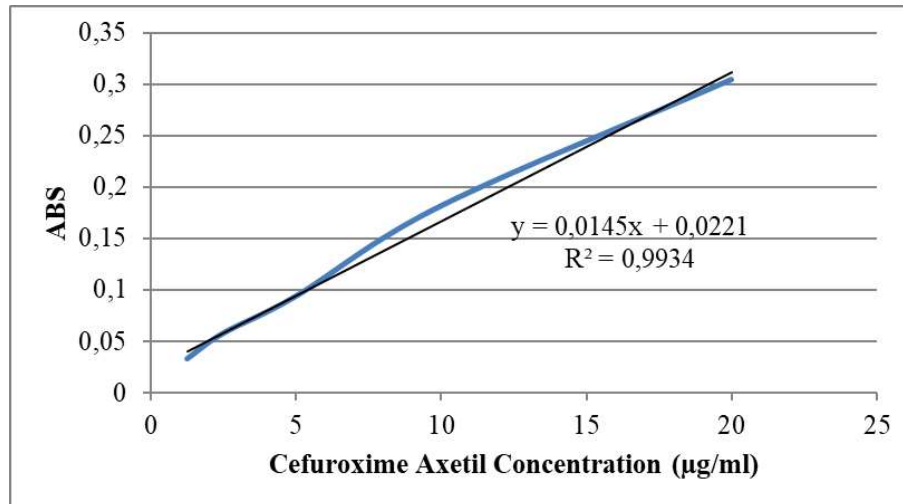


Figure A.2 Calibration curve of CA prepared by known concentrations in ethanol. Optical density was measured at 270 nm wavelength.

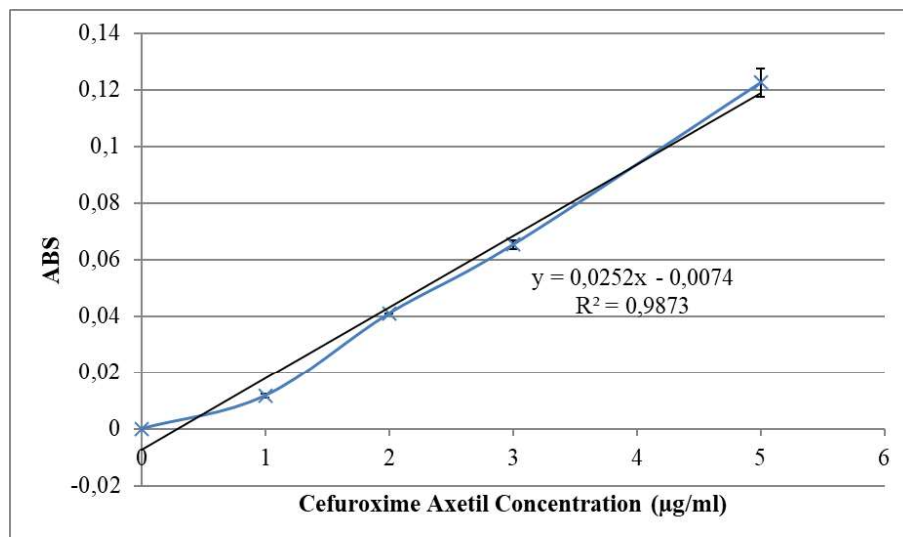


Figure A.2 Calibration curve of CA prepared by known concentrations in chloroform. Optical density was measured at 281.5 nm wavelength.

CURRICULUM VITAE

PERSONAL INFORMATION

Surname, Name: Dalgıç, Ali Deniz
Nationality: Turkish (TC)
Date and Place of Birth: 19 July 1990, Ankara
Marital Status: Single
Phone: +90 312 210 23 81
Fax: +90 312 210 44 62
email: deniz.dalgic@metu.edu.tr

EDUCATION

Degree	Institution	Year of Graduation
MS	METU Engineering Sciences	2014
BS	METU Biological Sciences	2011
High School	Izmir Private Turk Collage Science High School, İzmir	2007

WORK EXPERIENCE

Year	Place	Enrollment
2012-Present	METU Dept. of Engineering Sciences	Research Assistant

FOREIGN LANGUAGES

Advanced English

PUBLICATIONS

1. Guner, M. B., **Dalgic, A. D.**, Tezcaner, A., Yilanci, S., & Keskin, D. (2020). Dual phase scaffold produced by rotary jet spinning and electrospinning for tendon tissue engineering. *Biomedical Materials*, *IN PRESS*.
2. Motemeni, A., **Dalgic, A. D.**, Alshemary, A. Z., Keskin, D., & Evis, Z. (2020). Structural and Biological Analysis of Mesoporous Lanthanum Doped β TCP For Potential Use as Bone Graft Material. *Materials Today Communications*, *23*, 101151.
3. Alissa Alam, H., **Dalgic, A. D.**, Tezcaner, A., Ozen, C., & Keskin, D. (2020). A comparative study of monoaxial and coaxial PCL/gelatin/Ploxamer 188

- scaffolds for bone tissue engineering. *International Journal of Polymeric Materials and Polymeric Biomaterials*, 69(6), 339-350.
- Alshemary, A. Z., Pazarçeviren, E. A., **Dalgic, A. D.**, Tezcaner, A., Keskin, D., & Evis, Z. (2019). Nanocrystalline Zn²⁺ and SO₄²⁻ binary doped fluorohydroxyapatite: A novel biomaterial with enhanced osteoconductive and osteoinconductive properties. *Materials Science and Engineering: C*, 104, 109884.
 - Dalgic, A. D.**, Atila, D., Karatas, A., Tezcaner, A., & Keskin, D. (2019). Diatom shell incorporated PHBV/PCL-pullulan co-electrospun scaffolds for bone tissue engineering. *Materials Science and Engineering: C*, 100, 735-746.
 - Caliskan, Y., **Dalgic, A. D.**, Gerekci, S., Gulec, E. A., Tezcaner, A., Can, O., Keskin, D. (2019). A new therapeutic combination for osteosarcoma: Gemcitabine and Clofazimine co-loaded liposomal formulation. *International Journal of Pharmaceutics*, 557, 97-104.
 - Dalgic, A. D.**, Alshemary, A. Z., Tezcaner, A., Keskin, D., & Evis, Z. (2018). Silicate-doped nano-hydroxyapatite/graphene oxide composite reinforced fibrous scaffolds for bone tissue engineering. *Journal of Biomaterials Applications*, 32(10), 1392-1405.
 - Gurturk, Z., Tezcaner, A., **Dalgic, A. D.**, Korkmaz, S., & Keskin, D. (2017). Maltodextrin modified liposomes for drug delivery through the blood-brain barrier. *MedChemComm*, 8(6), 1337-1345.
 - Dalgic, A. D.**, Tezcaner, A., Elci, P., Sarper, M., Arpaci, F., Avcu, F., & Keskin, D. (2016). Improvement of a liposomal formulation with a native molecule: calcitriol. *RSC Advances*, 6(83), 80158-80167.